IKE Institut für Kernenergetik
und Energiesysteme

Influence of Multidimensionality and Interfacial Friction on the Coolability of Fragmented Corium

Werner Schmidt

Universität Stuttgart

Mai 2004 **IKE 2 - 149**

IKE Institut für Kernenergetik und Energiesysteme

Influence of Multidimensionality and Interfacial Friction on the Coolability of Fragmented Corium

Von der Fakultät Maschinenbau der Universität Stuttgart zur Erlangung der Würde eines Doktor-Ingenieurs (Dr.-Ing.) genehmigte Abhandlung

vorgelegt von

Werner Schmidt

geboren in Frankenberg/Eder

Hauptberichter: **Prof. G. Lohnert, Ph.D.**

Mitberichter: **Prof. Dr.Ing. T. Schulenberg**

Tag der Einreichung: **13. Oktober 2003**

Tag der mündlichen Prüfung: **7. Mai 2004**

ISSN - 0173 - 6892

Mai 2004 **IKE 2 - 149**

Universität Stuttgart

Abstract

After the shutdown of a nuclear power plant continued decay heat is released from the reactor core. To avoid environmental pollution, even during a very unlikely severe accident with failure of all cooling devices, the nuclear material has to be retained in the reactor containment. Due to the decay heat and a missing heat sink the core may dry out, and subsequently heat up and melt. This core melt, called “corium”, is a mixture of nuclear fuel, cladding and structure material. It will flow downwards, and, after some temporary configurations, pour down into the lower plenum of the reactor pressure vessel. Here the corium jet gets in contact with residual coolant water, and break up into fine fragments, that settle down as particulate debris bed. If the reactor pit is flooded, a similar configuration may also arise after vessel failure in the containment.

To achieve a stable cooled state enclosing the contaminated material, the decay heat of the corium has to be removed. Due to the magnitude of the internal power, and the non-availability of active cooling components, this heat can only be removed by evaporation of cooling liquid. The produced vapour escapes from the bed through the upper surface. To establish a steady cooled state, the evaporated water has to be replaced by a coolant inflow driven by gravity. Thus, a two phase flow of liquid water and steam establishes inside the particulate debris and determines the coolability.

The central aim of this work is to present a model for the calculation of the amount of heat that can be removed by this mechanism. As will be shown, this depends mainly on the friction laws and the geometric configuration of the particle bed. Especially the friction laws, with main emphasis on the interfacial drag between the steam and the water, are regarded in detail. For reactor typical configurations it will be shown, that the coolability is significantly increased in realistic multidimensional geometries, compared to commonly used 1D considerations. This increased coolability potential is due to preferred flow paths of the water.

Kurzfassung

Nach dem Abschalten eines Kernreaktors wird weiterhin Wärme freigesetzt. Diese Nachzerfallsleistung entsteht durch radioaktive Zerfälle in den Spaltprodukten und beträgt etwa 1% der thermischen Reaktorleistung. Bei einem Leicht Wasser Reaktor wird sie im regulären Zustand durch die Nachkühlsysteme aus dem Reaktorkern abgeführt. Im sehr unwahrscheinlichen Fall eines schweren Störfalls, mit Ausfall aller Nach- und Notkühlsysteme, ist diese Wärmeabfuhr nicht mehr möglich. Das Kühlwasser im Reaktorkern verdampft, und der nun trocken gelegte Kern heizt sich bis zum Aufschmelzen auf. Diese Schmelze, Corium genannt, ist eine Mischung aus Kernbrennstoff, Hüllrohr- und Strukturmaterialien und verlagert sich zum Unteren Plenum des Reaktordruckbehälters. Hier kommt der Schmelzestrahl in direkten Kontakt mit dem Restwasser im Druckbehälter, und fragmentiert zu Tropfen, die wiedererstarren und sich im unteren Plenum als Schüttung ansammeln. Wenn der Sicherheitsbehälter mit Wasser geflutet ist, führt ein analoger Prozess auch nach Versagen des Reaktordruckbehälters zu einer Schüttungskonfiguration in der Reaktorgrube.

Das zentrale Ziel aller Sicherheitsuntersuchungen ist es, kontaminiertes Material einzuschließen. Daher ist die Kühlbarkeit von solchen Partikelschüttungen aus fragmentiertem Corium eine zentrale Fragestellung. Um gekühlte stationäre Zustände zu erreichen, muß die Nachzerfallsleistung abgeführt werden. Aufgrund der großen Wärmeleistung und der Nichtverfühgbarkeit aktiver Komponenten, wie z.B. Pumpen, kann die Leistung nur durch verdampfen von Kühlwasser abgeführt werden. Der dabei entstehende Dampf entweicht über den oberen Rand der Schüttung. Zum Erreichen eines stationären Zustands ist es daher notwendig, daß das verdampfte Wasser durch einen von der Gewichtskraft getriebenen Zustrom ersetzt wird. Die sich dabei einstellende zwei-Phasen Strömung von Wasser und Dampf bestimmt die Kühlbarkeit der Partikelschüttung .

Im Rahmen dieser Arbeit wird das Kühlungspotential solcher Partikelschüttungen für reaktortypische Konfigurationen untersucht. Hierbei sind die Reibungsformulierungen für die zwei-Phasen Strömung von zentraler Bedeutung. Im Besonderen wird die Notwendigkeit einer expliziten Berücksichtigung der Interphasenreibung zwischen Wasser und Dampf aufgezeigt. Basierend auf den Reibungsformulierungen wird dann für realistische mehrdimensionale Konfigurationen die globale Kühlbarkeit untersucht. Hier zeigt sich ein erheblich verbessertes Kühlungspotential gegenüber üblicherweise betrachteten 1D Konfigurationen. Diese verbesserte Kühlbarkeit ergibt sich aufgrund von Querströmungen über bevorzugte Wasserpfade.

Contents

Nomenclature

Latin symbols

A	m^2	surface of the particles
c_p	$\mathrm{J/kg\,K}$	heat capacity
D_b	m	diameter off the gas bubbles
d_p	m	particle diameter
e	J/kg	specific internal energy
F_p	$\mathrm{N/m}^3$	volumetric particle-fluid drag force
F_i	$\mathrm{N/m}^3$	volumetric gas-liquid drag force
$F^\star$	-	normed force
f	-	fraction of coolant inflow from below
g	$\mathrm{m/s}^2$	gravitational constant
H	m	total bed height
h	J/kg	specific enthalpie
$J(s)$	-	Leverett function
j	m/s	superficial velocity of the fluids
j_r	m/s	relative velocity $\left(j_r = \frac{j_g}{\alpha} - \frac{j_l}{1-\alpha}\right)$
K	m^2	permeability
K_r	-	relative permeability of the fluids
L	m	length
M	kg	total corium mass
$P^\star$	-	normed pressure gradient
p	Pa	pressure
Q	W/kg	specific power
$\dot{q}$	$\mathrm{W/m}^3$	decay heat density
s	-	liquid volume fraction in the pores
T	°C	temperature
V	m^3	volume
$W(\xi)$	-	transition function
w_i	-	fractions of species
V	m^3	volume
v	m/s	real flow velocity of the fluids
z	m	height

Greek symbols

α	-	void, gas volume fraction in the pores
β	-	volume fraction
ε	-	porosity
η	m	passability
η_r	m	relative passability of the fluids
κ	$W/m^3\,K$	heat transfer coefficient
λ	$W/m\,K$	heat conductivity
$\Lambda(\alpha)$	$W/m^3\,K$	heat transfer coefficient evaporation
Γ	$kg/m^3\,s$	evaporation rate
μ	$kg/m\,s$	dynamic viscosity
σ	N/m	surface tension
ϱ	kg/m^3	density of the phase
ζ	-	volume fraction of the phase

Indices

eff	effective
v	vapour,gas
l	liquid
s	solid
sat	saturation
x	liquid or vapour

Abbreviations

AM	Accident Management
BWR	Boiling Water Reactor
DHF	Dryout Heat Flux
EPR	European Pressurised Water Reactor
LWR	Light Water Reactor
LMFBR	Liquid Metal Fast Breeder Reactor
PWR	Pressurised Water Reactor
RPV	Reactor Pressure Vessel

1 Introduction

The flow of fluids through porous structures is of central interest in various scientific and technical fields. Among these are environmental phenomena, as groundwater flow and the propagation of pollutants or oil in the ground, as well as technical applications, for example in the chemical industry, in catalytic reactors or in heat exchangers. In many of these applications more than one kind of fluid has to be considered. If these are immiscible, each fluid must be treated as a separate phase. Additionally chemical reactions, either exo- or endo-thermal, as well as evaporation or condensation may yield phase change processes between the fluids. In the most common configurations two fluids, one liquid and one vapour component, have to be considered.

In view of reactor safety of a nuclear power plant (NPP) such processes with two phase flow in porous media are at least in discussion since the severe accident in the nuclear power plant TMI-II in Harrisburg (USA) on March 28, 1979. Even after the chain reaction is stopped, either by a regular or by an emergency shutdown, heat is still produced due to ongoing nuclear α, β and γ-decay of the fission products. This residual power, the decay heat, decreases from about 6 % of the thermal reactor power directly after shutdown to about 1 % after one hour. Depending on the reactor type and size this power may be up to 40 MW even after some hours. For safety reasons this power has to be removed. In the worldwide commonly used various types of Light Water Reactors (LWR) this cooling is done by pumping cooling water via the primary circuit through the core, just as in normal operation. In a very unlikely severe accident, with failure of all normal and emergency cooling systems, the high decay heat yields evaporation of the cooling water in the core. Subsequently the core temperature will raise up to melting of core material. In contact with cooling liquid (water) at least some parts of the melt will be quenched, yielding a porous structure. This may occur either in the core region, in the lower head or, after failure of the reactor pressure vessel (RPV) in the reactor cavity as will be described in detail in chapter 2.

To avoid environmental pollution with radioactive material, remelting and further destruction, especially the failure of safety barriers, long term coolability of the corium must be reached. Therefore the cooling potential of such porous structures with internal power sources has to be observed. Due to the resulting high specific power of between

100 to 300 W/kg, depending on the composition of the core material (corium), and the non availability of forced coolant flow by pumping, this heat can only be removed by evaporation of cooling water. To yield long term coolability of the configuration, all evaporated water has to be replaced by water inflow due to natural forces. At the same time the produced steam must escape the porous structure driven by buoyancy forces.

Several experimental and theoretical programmes on debris coolability have been performed, especially in the beginning of the 1980's. The objective of most of these programmes had been to determine the maximum power, that can be removed from a heated particle filled column with a water reservoir on the top. The internal heating is produced either by resistance heaters (e.g. Hu and Theofanous [1]), by inductive heating (e.g. Hofmann [2]), or by direct neutron irradiation in a reactor (DCC-experiments [3]). A local dryout is detected by the temperature raise at thermocouples inside the particle bed. Based on these data, correlations for the friction laws of liquid and vapour were deduced. These correlations have then been used by e.g. Lipinski [4] in a model to calculate the critical heat flux, that corresponds to the maximum bed power before reaching a local dryout anywhere in the bed. Besides the boiling bed experiments, other authors (e.g. Chu et al. [5] or Tutu et al. [6]) used pressure loss measurements in isothermal air/water flow experiments to investigate the drag forces in the particle bed.

Mainly to investigate the risk of steam explosion, when a melt jet is poured into a water pool, experiments as FARO [7] or KROTOS [8] have been performed. In the view of the long term coolability, the resulting configurations of the particulate debris are prototypic for the ones to be expected during a severe accident. So, realistic conditions can be taken from these experiments. New experimental programmes to investigate the coolability of particulate corium have been started in recent years. Central aim of the SILFIDE experiments at EdF [9] is the measuring of effects resulting from the two dimensional geometry. Unfortunately, this experimental programme was stopped. A different attempt was made in the DEBRIS experiments performed at IKE [10]. These experiments are oriented towards specific investigations of the exchange terms. The friction and heat transfer laws are observed for boiling beds, as well as during the quenching of hot dry particles.

The knowledge about the coolability of strongly destroyed core structures and relocated core material in the late phase of severe accidents in nuclear power plants is the central point in the evaluation of safety margins. This results directly in the questions of accident management (AM). For example, if feeding of cooling water into the reactor pressure vessel (RPV) can be reestablished, the direct contact of this water with melt

may yield additional risks, especially the risk of strong steam explosions. On the other hand, it may be better to focus on other melt retention concepts. But, such concepts, as ex-vessel flooding or core catchers, are discussed and developed with regard to new reactors, and can not directly be applied to the existing ones. Additionally, they have to be safeguarded to cover all conditions. In the case of ex-vessel flooding, for example, all the corium is forming a melt pool in the lower head of the RPV, and must be cooled by heat transfer through the vessel wall to the water surrounding the vessel. This concept is questionable for large reactors. Additional problems arise from the focusing effect of a small metallic melt layer with high thermal conductivity on top of the melt pool, which may yield early RPV failure. So, especially in view of the existing reactors, but also for the new ones, the knowledge of the safety margins at any time during the accident, and at every safety barrier must be the central point in safety investigations. Based on this defence-in-depth concept the reactor safety and AM-measures have to be evaluated.

The central aim of this work is to point out the cooling potential of particulate corium debris in a water environment, either in- or ex-vessel. It will be shown, that this cooling potential is remarkable higher for realistic two- and three-dimensional configurations, compared to the usual used 1D results. Multidimensional effects increase the water inflow either laterally, e.g. through regions with higher porosity (gap), or by direct connected loops to lower bed parts. So, this yields enhanced coolability in such configurations, compared to homogeneous 1D debris beds, where all water is coming from a pool on the top, as considered classically. Additionally, the interfacial friction, always acting against water inflow and steam outflow (counter-current flow) in the top flooding case, enhances the coolability if water and steam have the same flow direction (co-current flow). This may occur at least in some parts of the bed, where water coming from the sides is dragged by the steam flowing upwards.

In the view of reactor safety, long term coolability must be reached. This is equivalent to a steady state, where all evaporated water is replaced by water inflow everywhere in the particulate bed. But first of all the melt has to be quenched. The fragmentation and quenching processes are discussed e.g. in [11]. So, the long term coolability of the corium is a necessary, but not a sufficient condition in accident management. This work only focuses on steady states, and thus on the long term coolability. Due to the small temperature differences, details of the heat transfer coefficients between the phases will not be discussed here. The main emphasis in this work is on the friction laws, especially the formulation of the interfacial friction, because the coolability is limited by the water access. In the above mentioned report [11] various calculations with the

models presented here are given, also including different geometric configurations with hindering effects, as e.g. a layer of small particles on top of larger ones, or larger unfragmented parts.

In the next chapter the development of a typical severe accident in a Light Water Reactor, yielding particulate debris or porous structures, is described in detail. The central parameters that influence the coolability are given in chapter 3. Here, the effects are discussed, as well as the range of values to be expected in the application case. In the following chapter the WABE-2D model, describing the processes in the debris bed, is presented. As will be explained there, the coolability is not restricted by the heat transfer from the heated particles to the cooling liquid, but by hydraulic limitations due to the friction of the moving fluids. Especially the partition of the pressure loss between the two phases, water and steam, and the influence of interfacial friction will be discussed for different mathematical models in detail. To check the validity of these models, results based on them are compared to experimental data for isothermal air/water experiments, as well as for boiling beds in chapter 6. The influence of the described multidimensional effects, as well as of the interfacial friction between water and steam, on the overall coolability of a particulate debris bed will be shown in the last chapter for exemplary configurations in the lower plenum of the reactor pressure vessel and ex-vessel, in the reactor cavity. The enhanced coolability compared to classical 1D investigations will be shown here.

2 Development of particulate debris beds in a Light Water Reactor

After regular or emergency shutdown of the chain reaction in a nuclear power plant (NPP) continued decay heat is produced in the core and must be removed to avoid heat-up and melting of the core. This decay heat is in the order of 6 % of the thermal reactor power directly after shutdown, and decreases with time to about 1 % after one hour. In normal operation this heat is removed by the reactor cooling systems.

During a very unlikely severe accident with failure of all normal and emergency cooling systems, several configurations with particulate debris or porous structures of the corium may develop. Due to the decay heat the cooling water in the core region will evaporate, and the water level in the reactor pressure vessel (RPV) will decrease. Depending on the accident development and reactor design the core will dry out after one to several hours, starting at upper regions. The decay heat yields a continued heat-up of the fuel rods and the other core materials. Starting at a temperature of about 1500 K, Zirconium of the fuel rod cladding will oxidise in the steam environment. This exo-thermic reaction produces additional heat which - in turn - accelerates the temperature rise and the core degradation. The continued temperature increase will lead to melting of core material. Several other processes, as candling, or the dissolution of the fuel by metallic melt, occur during this stage, but these will not be discussed here. For a more detailed description see e.g. [12] or [13].

If in this stage of the severe accident the cooling systems of the reactor could be reestablished, e.g. by restarting the pumps, the hot rods get in direct contact with cooling water. Due to this thermal shock some of the rods may crumble, and form a configuration with particulate debris surrounded by intact core regions, as shown in figure 2.1 (a). Still the decay heat must be removed, additionally to the quenching of the hot core material. The overall coolability is supported by the external pumping in such a configuration.

Without reestablished cooling the temperature in the dry parts of the core will further increase, yielding melting of the core materials. First metallic components, as Zr of the rod cladding and steel from the mounting structures will melt. Later, with increasing

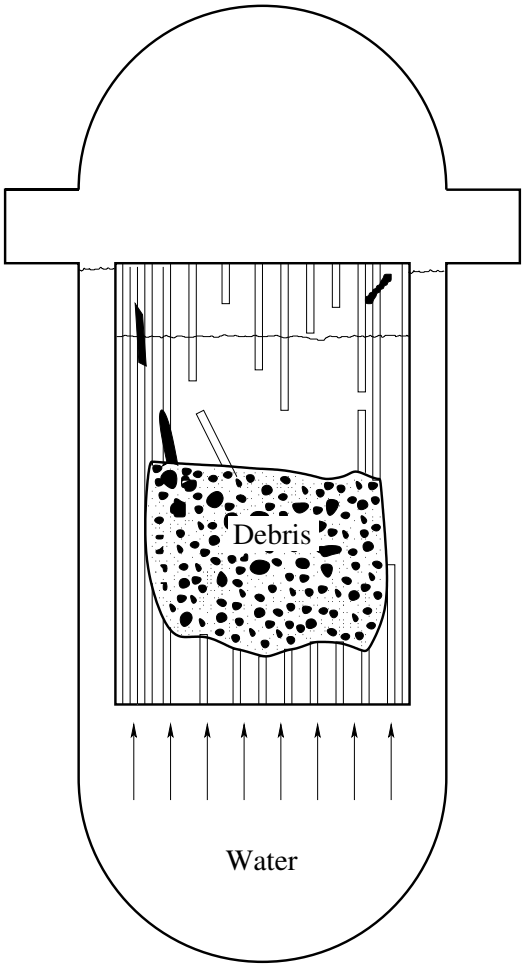

(a) in the core

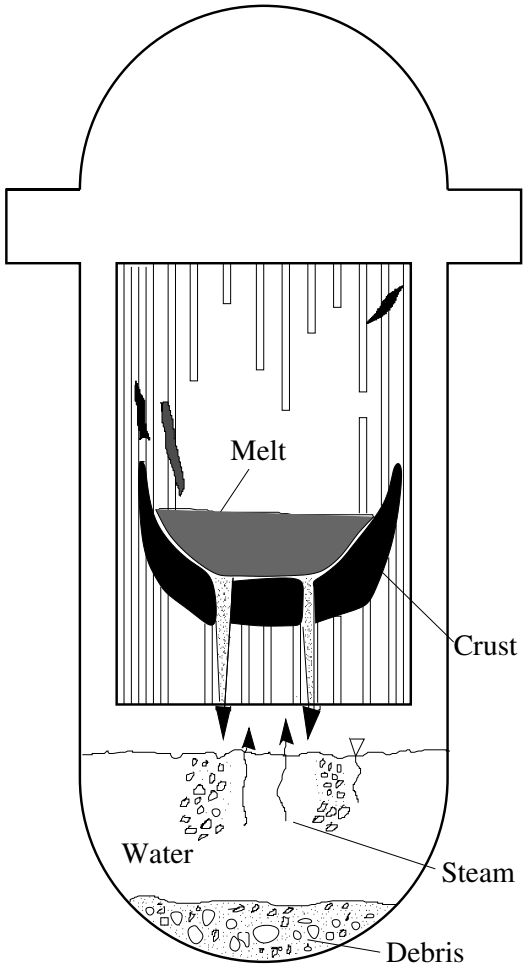

(b) in the lower head

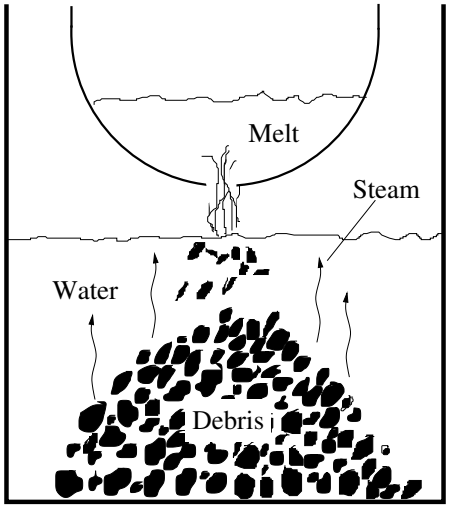

(c) in the reactor pit

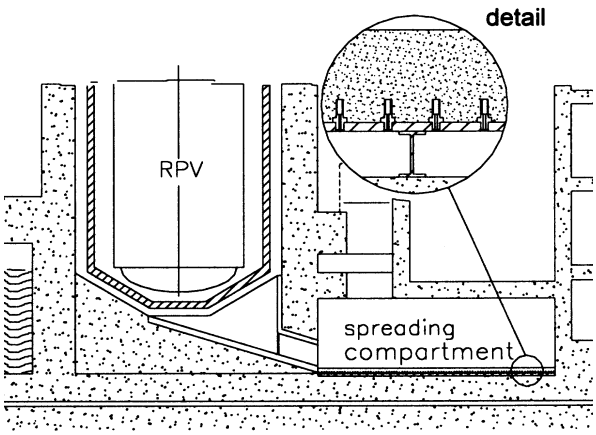

(d) COMET core catcher

Figure 2.1: Different configurations with particulate debris during a severe accident in a light water reactor

temperature, also the ceramic parts of oxidised ZrO_2 and the UO_2 fuel start melting. Due to gravity, this melt relocates to lower parts, where it freezes again, because the lower parts of the core have been dried out later during the decrease of the water level. This refrozen melt fills the space between the rods and forms a crust. Further down-pouring melt will be collected on this crust as a melt pool. The stability of this configuration depends on the cooling from below, e.g. by heat conduction, radiation and steam flow. Two extreme configurations may be considered. If there is only low cooling from below, no stable crust will be built up. So, no large melt accumulation in the pool occurs, and the melt will almost directly flow towards the lower head. In the other extreme, with good cooling of the crust, a large amount of melt will be collected in the melt pool. Due to natural convection in the melt pool the temperature will be highest at the top. So, crust failure has to be expected in the upper region, yielding a lateral melt release. In both cases only a small mass flux of melt to the lower head may be expected. This mass flux is of essential importance for the reaction of the melt with the residual water that has to be expected in the lower head. A detailed description of the melt accumulation and relocation process is given in [12]. In the view of reactor safety, small melt mass fluxes are favourable, because of the reduced risk of steam explosions, and the better fragmentation when pouring into water. For larger melt fluxes the risk of steam explosions is increased, or, if no explosion occurs, a total fragmentation of the melt becomes questionable.

As described above, only small melt fluxes from the core to the lower head may be expected. Additionally, if the reactor pressure vessel is intact, the lower head will be filled with residual water. When the melt pours into this water, the jet will break up and fragment into droplets, that refreeze and settle down as particulate debris. According to e.g. the FARO experiments [7], investigating this process, particle diameters from 1 to 10 mm can be expected. The so formed particle bed still includes the decay heat yielding a specific power of 100-300 W/kg, depending on reactor type and the corium composition. This heat must be removed to enable long term coolability and in-vessel retention of the nuclear material. The resulting large power density (0.5-1.5 MW/m^3 when assuming a porosity of $\varepsilon = 0.4$) can only be removed by evaporation of water. To establish a stable and coolable configuration, the evaporated water has to be replaced. This requires basically that the water pool surrounding the debris is refilled, either by water feeding into the vessel or by recondensation of the already evaporated liquid. The second requirement for long term coolability is inside the particle bed itself. The produced steam must be able to escape from the debris, while the evaporated water has to be replaced by penetrating water influx from the pool. The investigation of these processes is the central aim of this work, and treated in the following chapters.

As shown there, the chances for achieving a stable, long term coolable configuration are remarkable high, esp. when the geometric form of the configuration is taken into account. Such a configuration in the lower head is shown in figure 2.1 (b).

If the resulting debris configuration in the lower head of the reactor pressure vessel is not coolable, at least some part of it will dry out and heat up again. For really small dry zones in upper bed regions the temperature rise may be limited by conductive heat transfer to the surrounding of still cooled parts and by heat transfer to steam, coming from lower bed regions. If this is not possible, the corium will remelt and relocate as in the core, yielding a melt pool again. In the extreme case, when all water in the vessel is evaporated, a large melt pool develops in the lower head. Again, due to convection in the pool, the highest temperature is reached at the top. Additionally, as the corium consists of metallic and ceramic melt, a metallic layer with high heat conductivity will establish there. The vessel wall will be attacked and weakened by the hot melt, will begin creeping, and in the following the vessel will fail, which results in melt release into the cavity.

Two main ex-vessel configurations, the dry and the wet scenario, must be distinguished after vessel failure. Especially for boiling water reactors (BWR) the reactor cavity may be assumed to be flooded with water, either automatically, or due to accident management measures. The melt flowing out of the broken vessel pours into this water. Again, as described above for the lower head, the melt jet will break up and fragment. Depending on the conditions, esp. the melt flux, steam explosions may occur. But, according to the experiences from the FARO experiments, a good fragmentation and re-solidification of the corium without large steam explosions may be expected. These corium particles settle at the bottom of the reactor pit, again with good chances for coolability by the surrounding water pool. Figure 2.1 (c) gives a sketch of such a configuration.

In the new European Pressurised Reactor (EPR) concept a dedicated ex-vessel core catcher is installed. Here, the melt flowing out of the vessel is collected in the dry reactor pit, and is then exhausted to a spreading area. In one concept, the COMET core catcher (see [14, 15]), a sacrificial layer including nozzles with plugs is used. These nozzles are connected to a water pool at higher-placed level. The spreading melt now attacks the sacrificial layer, as well as the plugs, and opens the water path. Due to the hydrostatic head the water is injected through the nozzles into the melt, with the goal of forming a solid porous structure. Additionally, the spreaded corium can be cooled from above by a water pool or by sprinklers, as shown in figure 2.1 (d). To reach long term coolability, continuous water feeding, at least from the top, is necessary. The shallow height of the spreaded corium now supports the coolability from above.

In general, the central goal is to achieve a stable cooled configuration, to assure integrity of the safety barriers. Many parameters, as e.g. the particle size, debris location, geometry or chemical composition determine the coolability. These parameters depend on the reactor type and on the accident progression. Prototypical values, as well as variations of these values have to be assumed in calculations.

3 Main Parameters affecting the debris coolability

3.1 Definition of the dryout heat flux

Looking into the literature, the coolability of particulate beds with internal heat sources is limited by the dryout heat flux (DHF). This is the maximum heat flux that can be removed from the bed through the upper surface. For the particulate corium debris, as considered here, the internal power is converted by evaporation of cooling liquid (water). The produced steam flows up, driven by the buoyant force, and escapes through the top surface of the bed. So, the dryout heat flux is determined by the maximum steam flux (critical steam flux) that can escape through the upper surface of the bed. Its enthalpy is normalised by the cross section yielding the dimension W/m^2. So this term is just surface related, and no statement about the underlying structure or distribution is done.

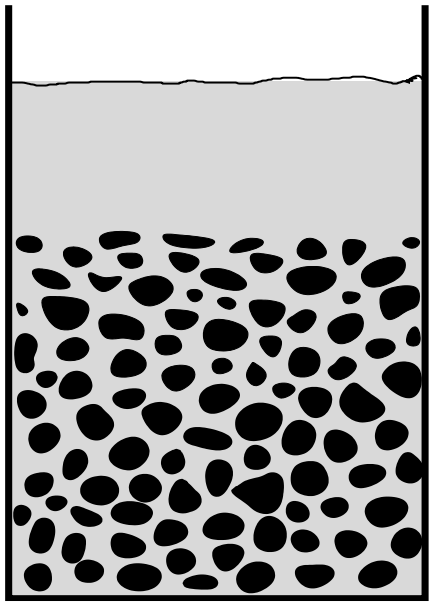

Figure 3.1: 1-D configuration with coolant pool

Classically, a pure one dimensional configuration with a water pool as coolant reservoir at the top is regarded. Figure 3.1 shows a principle sketch of such a configuration. The produced steam arises up, and escapes through the upper surface. In steady state the evaporated coolant has to be replaced by water from the overlying pool. So, liquid coolant and produced steam are in counter-current flow, and the coolability is limited by the counter-current flooding limit. This limit will be reached in the upper region of the bed, where the accumulated steam flux limits the water flux necessary to replace the evaporated coolant. A further increased steam flux, corresponding to higher internal heating, yields a transient development towards local dryout. The evaporated liquid can

no longer be replaced completely by the inflow. In the following subsections the main parameters influencing the dryout heat flux will be discussed. Relevant values of these parameters for the expected debris in Light Water Reactors will be given. Other effects, only having minor influence on the overall coolability of the particulate bed, are not discussed in detail here. For example the subcooling of the water pool may be mentioned, yielding a small subcooled non boiling zone at the top. Another example with only minor influence is the height of the water pool. This becomes only relevant for very shallow pools. In general, only one dimensional homogenous configurations, as described above, will be considered here, except in the last subsection.

3.2 Porosity

Due to the counteracting shore up of the particles, hollow space establishes in the debris bed. The fraction of this hollow space in a representative control volume is called porosity and is defined by:

$$\varepsilon = \frac{V_{hollow}}{V_{total}} . \tag{3.1}$$

In the idealised assumption of a bed of spheres with the same size, the porosity is dependent on the packing structure. The lower bound of the porosity is given for rhombohedrical arrangement, where each sphere has contact to 12 neighbours. The porosity in such a configuration is $\varepsilon = 0.2592$. On the other hand a cubic arrangement with 6 next neighbours and a porosity of $\varepsilon = 0.4764$ is the loosest configuration. In an unarranged configuration neither of these extreme cases will occur. The mean porosity will be in the order of $\varepsilon \approx 0.39$ (see also [16]). This value is just a mean one in the whole bed, that may vary locally.

In real debris beds with irregular particle shapes and sizes, as to be expected for the fragmented corium, the porosity will additionally be influenced by the particle form and size distribution. The irregular shapes yield larger holes and thus higher porosity. On the other hand, different particle sizes will reduce the porosity, because the smaller ones can fill the holes of the bigger particles. This reduction of the porosity is dependent on the size distribution and on the local mixing. For example, in the case with two kinds of spheres with different diameter, a minimum porosity of ε^2 may be reached for vanishing size and about 3/4 mass fraction of the smaller particles (see [16]). For the expected particulate debris during severe accidents in a nuclear power plant a porosity of about $\varepsilon \approx 0.4$ may be assumed.

The porosity influences the dryout heat flux in two ways. Firstly, in the case of higher porosity, more cooling liquid is inside the bed. So, more water can evaporate, and more heat can be removed. Secondly, and even more important for the long term coolability of the debris, is the fact, that with increasing porosity the friction losses of the fluid phases decreases. Geometrically this can already be seen by the larger available cross section for the fluid flows. The vapour can escape quicker from the bed, and the liquid coolant can easier penetrate into it. In any case, the higher the porosity, the better the overall coolability of the corium will be.

3.3 Particle diameter

Debris beds with small particles also have small pores. This directly shows the higher pressure loss, and thus the increasing friction for flows with decreasing particle diameter. More resistance is acting against the flows of coolant and vapour for smaller particles. Thus, the dryout heat flux increases with the particle size. Experimental results of different authors taken from the literature are given in figure 3.2. Two different regions can be identified. For very small particles an accelerated decrease of the dryout heat flux with decreasing diameter can be seen. The reduced friction losses for flow through larger particles yields increased flow velocities, and the influence of the diameter is reduced.

For spherical particles the diameter is already given by the geometric form. In the general case of irregular particle shapes a particle diameter may be defined by the ratio of volume to surface area:

$$d_p = 6\,\frac{V}{A}\ . \tag{3.2}$$

Multi grain configuration, as in the reactor case, consist of different particle sizes. These may be split in classes with volume fractions w_i. According [16] a mean diameter may be defined via:

$$d_{p_m} = \frac{1}{\frac{w_1}{d_{p_1}} + \frac{w_2}{d_{p_2}} + \cdots + \frac{w_n}{d_{p_n}}}\ . \tag{3.3}$$

The diameters used in the reactor calculations of chapter 7 are such mean diameters in a representative control volume, and, together with the porosity, determine the fluid-particle friction.

The particle diameters to be expected during severe accidents in Light Water Reactors can be taken from the FARO- [7] and KROTOS-experiments [8] performed at JRC Ispra. In these experiments molten Thermite (AlO_2) as simulation material, as well as Corium (UO_2, ZrO_2) is poured into a water pool. As already described in chapter 2 for the reactor scenario, the melt jet is fragmented. These fragments solidify in the water environment, settle down and form a debris bed at the bottom of the vessel. In the experimentally observed particle size distribution almost all particles have sizes in the range between 1 mm and 6 mm. Therefore in our application cases for Light Water Reactors such particle diameters have to be assumed to explore realistic debris conditions. Many observations in the beginning of the 1980's were oriented on the same problem in Liquid Metal Fast Breeder Reactors (LMFBR). Here smaller fragments with a diameter $d_p < 1$ mm are expected.

Another criterion concerning the particle diameter has to be mentioned here. The heating power, distributed over the whole particle volume, has to be transported to the particle surface via heat conduction. There, cooling liquid is evaporated consuming the heat. Due to the small heat conductivity of the corium, this process is limited. Assuming a spherical particle, the heat conduction equation may be solved with saturation temperature at the surface and melting temperature in the centre as boundary

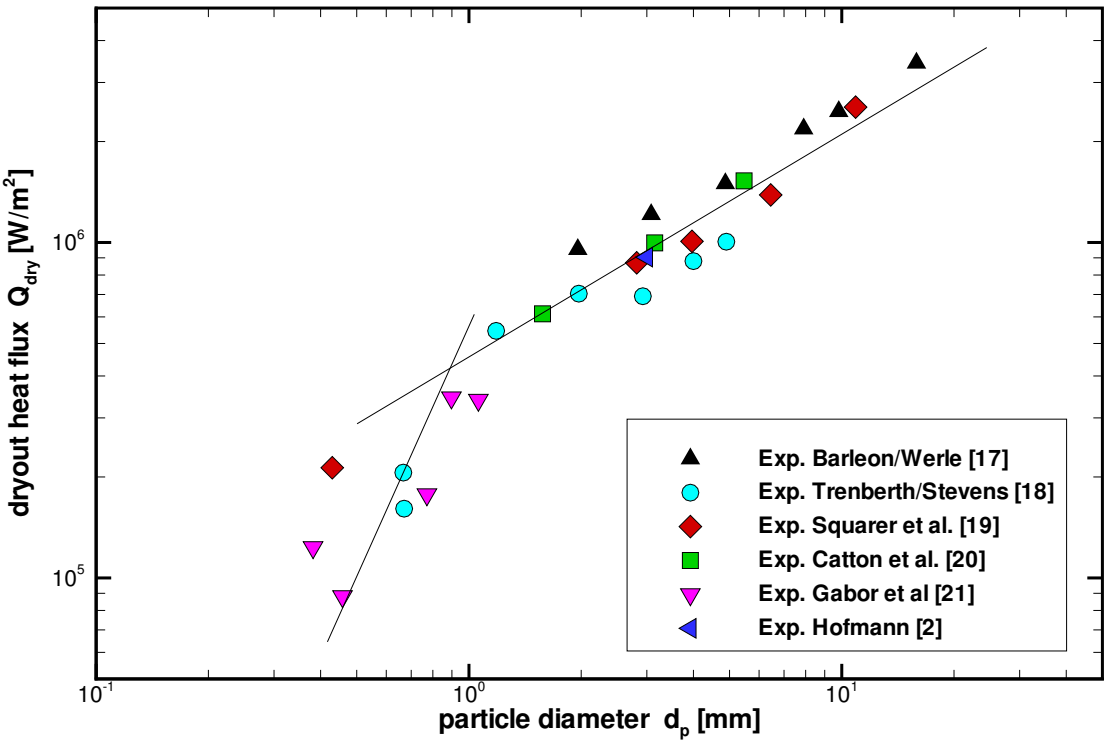

Figure 3.2: Dependence of the dryout heat flux on the particle diameter

conditions. The so deduced maximal particle diameter is larger than 10 cm. So, for realistic particle sizes it is assured, that the heat can be transfered to the particle surface without remelting in the centre.

3.4 Bed height

For a fixed power density in a homogeneous particulate bed the overall coolability is mainly determined by the bed height. The higher the bed, the more integrated vapour has to escape through the upper surface. So, the counter-current flooding limit will be reached for less power in deeper beds. On the other hand, as the dryout heat flux is defined by the maximum vapour flux it is equivalent to increase the bed height, or to raise the power inside the bed. Therefore, the dryout heat flux is just given by the total bed power, and is independent of the bed height. So, different beds may be compared by comparing their dryout heat flux.

This independence of the dryout heat flux on the bed height is only valid for deep beds, where the effects at the transition zone from the bed to the water-pool can be neglected. In shallow beds these effects gain importance and must be considered (see

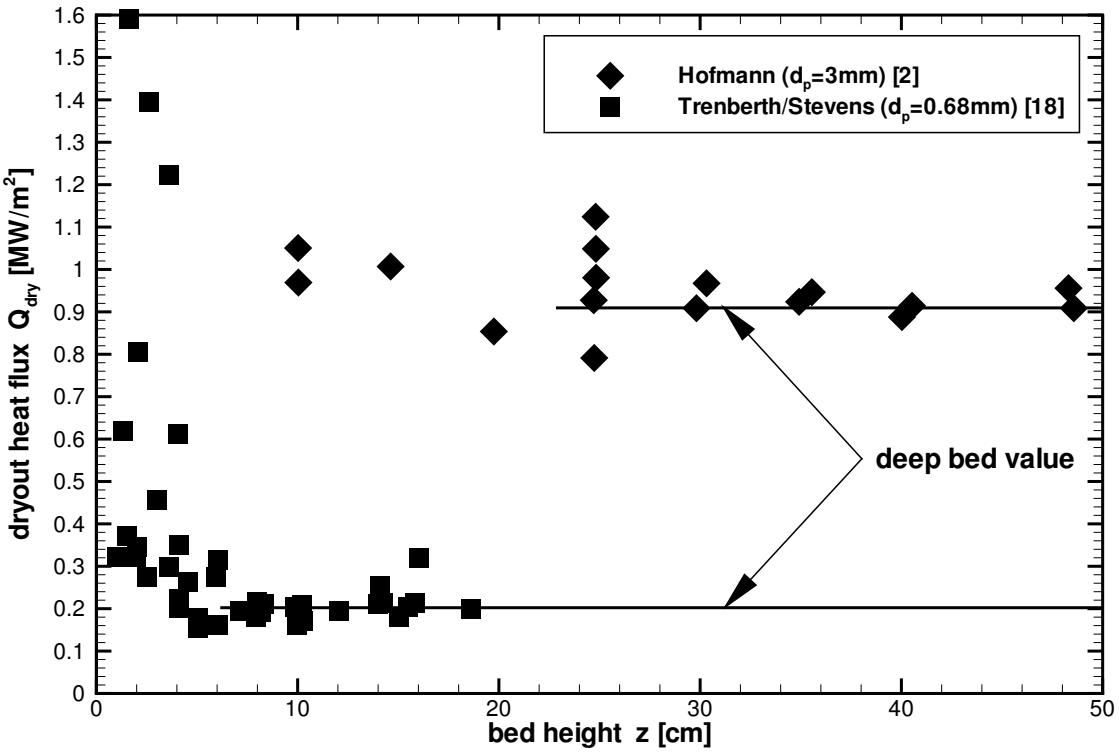

Figure 3.3: Dryout heat fluxes for different bed heights

[22]). The main effects are the establishment of vapour channels, and the capillarity in the upper bed region. Both effects raise the vapour velocity in the transition region, and higher steam mass fluxes are found, yielding an increased dryout heat flux. In figure 3.3 measured dryout heat fluxes for different bed heights are shown for two different particle diameters. The limit of the deep bed value is reached at about 100 times the particle diameter, as can be seen in the figure. Due to the large total mass of the corium particle beds in a reactor, only deep beds have to be considered. So, a detailed treatment of the transition region is not necessary here.

3.5 Pressure

Figure 3.4 shows experimental results of the dryout heat flux for different system pressure from the DCC2-Experiments [3], performed in 1985 at Sandia National Laboratory. Two counteracting effects can be seen. Starting from atmospheric pressure, there is a strong increase in the dryout heat flux for increasing system pressure. This can be explained by the increasing density of the steam. The produced steam fills up less volume fraction, and more total steam can escape the bed before the limitation of

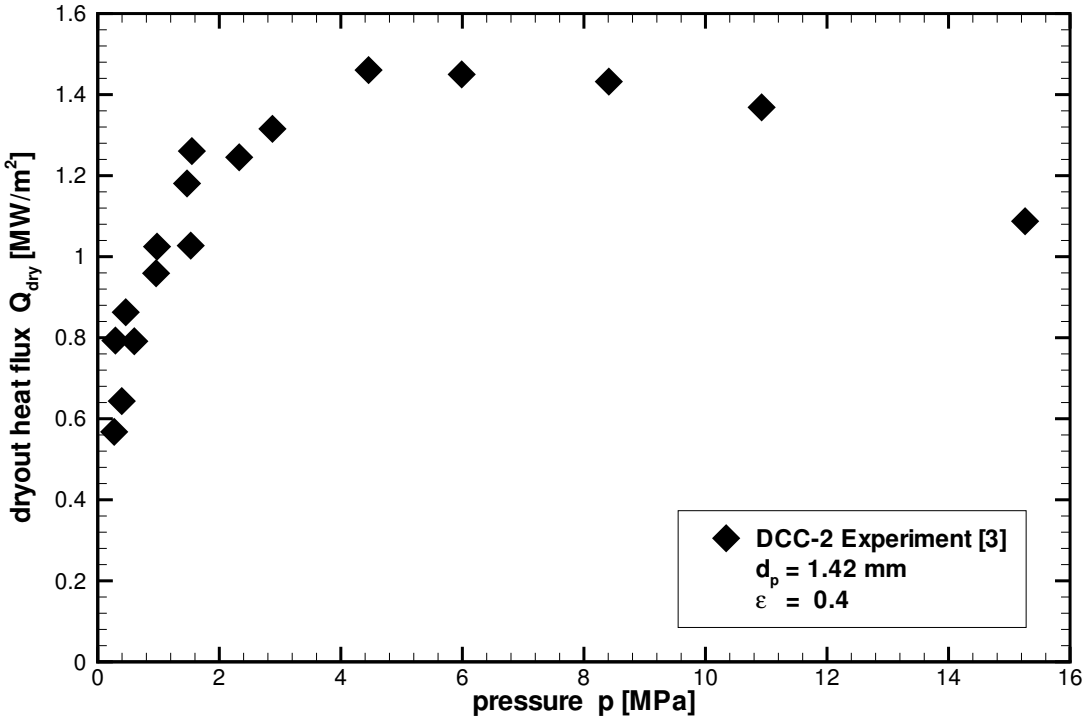

Figure 3.4: Influence of the system pressure on the dryout heat flux

the counter-current flooding limit is reached. The counteracting effect is due to the decreasing latent heat of the evaporation process. This effect becomes dominant for system pressures above about 70 bar (7 MPa) and explains the decrease of the dryout heat flux for high pressures.

In reactor typical cases the system pressure to be expected depends strongly on the reactor type, as well as the accident history. For ex-vessel debris an upper limit for the pressure is given by the maximum pressure load of the containment. Dependent on the reactor type, a maximum system pressure of about 10 bar (1 MPa) may be assumed. Especially for pressurised water reactors, significantly higher pressures are possible in the vessel. But, due to depressurisation, either automatically, or manually by accident management measures, system pressures below 10 bar have to be expected here too. For realistic conditions it can be concluded, the higher the system pressure, the better the overall coolability.

3.6 Coolant inflow

Up to now, just coolant inflow from a pool at the top of the bed was considered. The produced vapour accumulates, driven by buoyancy forces, from the bottom to the top and escapes the bed at the upper surface. Counteracting, the coolant must penetrate from the overlying water pool into the bed to replace the evaporated liquid. The limiting condition for a steady state is given by the counter-current flooding limit, where just all evaporated coolant can be replaced. Higher power inside the bed will increase the vapour flux, and no steady state can be established anymore. In such transients a dryout occurs in lower bed regions and subsequently relocates towards the bottom of the bed. These dryout regions will heat up due to the missing of cooling. Such beds are uncoolable and the dry zone will remelt. Results of model calculations on the transient behaviour are shown in chapter 7.1.

However, enhanced coolability can be expected if coolant inflow via the bottom of the particle bed is possible. A possible configuration with coolant at hydrostatic pressure at the lower bound of the bed is shown in figure 3.5. In such a configuration the coolant can easily reach lower bed regions from below, without being hindered by the counter-current vapour flux. In this case, not all the water necessary to maintain steady cooling has to penetrate the debris bed from above. Due to the higher liquid saturation in lower bed regions, corresponding to an enlarged cross section for the liquid flow, the friction of the liquid flow is reduced. This supports the coolant inflow from below. In this case the counter-current flooding limit is not limiting the coolability of the bed. An

upper limit for the coolability in such a configuration is reached, when the accumulated vapour fills the whole pore volume near the top of the bed. So, a local dryout has to be expected in upper bed regions for bed powers beyond this critical value. The critical heat flux here is substantially higher than the dryout heat flux in the purely top fed case.

This discussion already shows the inadequacy of the term "dryout heat" flux to characterise the coolability of internal heated particle beds. In this surface oriented term the inner structure of the bed, as well as geometrical and flow conditions, are not taken into account. This will be especially important for large particulate beds in multidimensional configurations, which are to be expected during severe accidents in nuclear power plants. Lower parts of the bed may be better fed with coolant via flow paths with less friction. This may inherently be due to regions with less bed height, for example in a hemispherical lower head of the reactor pressure vessel, or for mound shaped debris in water environment. Thus, it is generally not possible to determine the coolability of volumetric heated debris by just using bed properties like bed height, porosity, particle diameter and system pressure. A more detailed analysis with a multidimensional model to include realistic configurations is necessary.

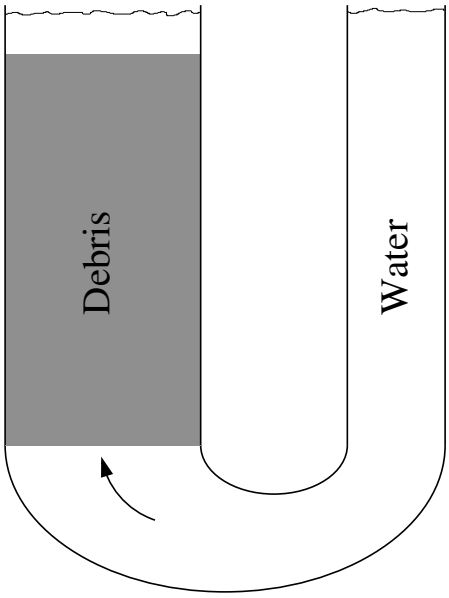

Figure 3.5: Example configuration for a debris bed with water inflow from the bottom

3.7 Effects from inhomogeneities

Inhomogeneities in the porous structure itself have a direct influence on the coolability, either supporting or hindering. Densified regions with a smaller local porosity, resulting from conglomerations of melt droplets during the quenching process, complicate the local coolability. Another major hindering effect occurs in stratified beds, where a layer of smaller particles covers the main bed part. Such configurations may also be expected for particulate debris in a Light Water Reactor, due to the settlement of the particles in a deep water pool. For a simple 1D top fed configuration, as described above, the coolability is dramatically reduced, yielding an extended dryout even for bed powers

much smaller then the dryout heat flux for smaller particle sizes. Experimentally this was shown by Hofmann [23]. This reduction is due to the capillary pressure at the interface between the main particle bed and the layer of the smaller particles. Due to this capillary pressure the layer of smaller particles acts like a sponge, holding the water. This dramatic effect will be reduced if other flow paths to the main debris exist, as for example paths from below (like in figure 3.5), or laterally in a realistic three dimensional configuration. Such water paths supporting the overall coolability, may be intrinsic for the bed configuration, or can be achieved by constructive measures.

Again, this discussion shows that the overall coolability of the debris in reactor typical configurations is not easily determined by some simple parameters. A multidimensional model including the capability to resolve heterogenous distributions and flows is necessary to include the hindering, as well as the supporting effects on the coolability. By using such a model, the coolability of typical configurations can then be investigated with the goal to enhance the reactor safety.

4 Description of the model WABE-2D

4.1 Conservation equations

The model WABE-2D (WAter BEd) is being developed at IKE in the frame of the KESS code system. The KESS system consists of several modules, simulating the behaviour of Light Water Reactors during severe accidents in the early, as well as in the late phase of the accident progression. Several of these modules are also included in the German system code ATHLET-CD.

The module WABE-2D describes the coolability of internally heated porous structures in two dimensions. Either x-y geometry, or r-z geometry with cylindrical symmetry may be chosen. Besides the solid particles two fluid phases, liquid coolant and vapour are considered. The basic assumption is that each phase is regarded as a continuum. So, each phase fills only a fraction of the whole volume. Therefore a representative control volume of sufficient size has to be used. In this control volume the microscopic description can be replaced by a macroscopic one. The macroscopic parameters are defined by averaging over the control volume. By this, the usual descriptions of fluid dynamics and heat transfer, weighted by the volume fractions, may be used. The particles are assumed to be a fixed matrix which is passed by the flow of the fluids coolant and vapour. The system is determined by the conservation equations for mass, momentum and energy. Additionally, some constitutive laws for closure of the equation system are necessary.

The volume fraction of the solid phase is given by the porosity via $\zeta_s = 1 - \varepsilon$. As all volume fractions must sum up to 1, one additional parameter is sufficient to define the volume fractions of the coolant and the vapour. The vapour fraction in the pores (void α) is chosen for this parameter. It can vary between 0 and 1. This leads to the following definitions of the volume fractions in the control volume.

$$\begin{aligned} &\text{Particle} && \zeta_s = \frac{V_s}{V} = (1-\varepsilon)\ ; \\ &\text{Liquid} && \zeta_l = \frac{V_l}{V} = (1-\alpha)\,\varepsilon\ ; \\ &\text{Vapour} && \zeta_v = \frac{V_v}{V} = \alpha\varepsilon\ ; \end{aligned} \tag{4.1}$$

The liquid saturation in the pores $s = 1-\alpha$ may be chosen as well, leading to similar equations.

Using this definition the mass conservation equations for the fluids can be written:

$$\text{Liquid} \qquad \partial_t(\,\varepsilon\,(1-\alpha)\,\varrho_l\,) + \nabla(\,\varrho_l\,\vec{j}_l\,) = -\Gamma \tag{4.2}$$

$$\text{Vapour} \qquad \partial_t(\,\varepsilon\,\alpha\,\varrho_v\,) + \nabla(\,\varrho_v\,\vec{j}_v\,) = \Gamma \tag{4.3}$$

with the phase change rate Γ, representing either evaporation or condensation. The velocities j_x are superficial velocities. These are defined by multiplying the real flow velocity v_x with the volume fraction ζ_x, respectively.

$$j_x = \zeta_x\, v_x \quad , \quad (x = l, v) \tag{4.4}$$

Multiplying this superficial velocity with the corresponding density ϱ_x gives the mass flux density of the fluids.

In porous structures the acting forces F_p are the friction between the fluid and the solid, as well as the interfacial drag between the fluids F_i. So, including the volume fractions, the momentum conservation equations for the fluids may be written as:

$$\zeta_x\,\varrho_x\,\frac{\partial}{\partial t}\,\frac{\vec{j}_x}{\zeta_x} + \varrho_x\,(\vec{j}_x\,\nabla)\frac{\vec{j}_x}{\zeta_x} = -\,\zeta_x\,\nabla p_x + \nabla(\zeta_x\tau_x) + \zeta_x\,\varrho_x\,\vec{g} - \vec{F}_{px} - \vec{F}_{ix} \tag{4.5}$$

where τ is the viscous stress tensor. The terms at the left side follow from the convective derivative, while on the right side the internal and external forces are balanced. The first three terms are the usual ones from the Navier-Stokes equations for the flow of an unlimited fluid. The last two terms symbolise the specific friction for the two phase flow in the porous structure. According to Newton's principle the interfacial friction F_i between the fluids has to be the same, but with opposite sign ($F_i = F_{iv} = -F_{il}$). The

most dominating forces on the fluids in the porous structure are the particle-fluid and the interfacial drag. So, assuming an instantaneous adjustment of the velocity fields on pressure variations, the left hand side as well as the viscous terms may be dropped. Additionally, especially for steady state conditions this is valid because the applied formulations for the friction terms are based on measurements, and thus include the inertial as well as the viscous forces implicitly. Dropping the small terms leads to:

$$-\varepsilon\,(1-\alpha)\,\nabla p_l = \varepsilon\,(1-\alpha)\,\varrho_l\,\vec{g} + \vec{F}_{pl} - \vec{F}_i \tag{4.6}$$

for the liquid, and

$$-\varepsilon\,\alpha\,\nabla p_v = \varepsilon\,\alpha\,\varrho_v\,\vec{g} + \vec{F}_{pv} + \vec{F}_i \tag{4.7}$$

for the vapour.

Detailed formulations for the frictions forces can be found in the next chapter.

Although not necessary for the long term coolability and the examination of steady states, thermal non-equilibrium is considered in WABE-2D. Each of the three phases may be at it's own temperature. This further enables calculations on the development of dry zones, as well as calculations on quenching of hot debris. This quenching of the corium is necessary to reach coolability in the reactor application. So, in WABE-2D an energy conservation equation is implemented for each phase separately. The decay heat $\dot{q}$ is a source term in the energy conservation equation of the solid phase. The corresponding heat sink is due to heat transfered directly to the evaporation. Additionally, in the general case, a heat transfer to the vapour as well as to the coolant have to be considered. This yields the following formulation:

$$\begin{aligned}\partial_t(\,(1-\epsilon)\,\varrho_s\,c_{p_s}\,T_s\,) \;-\; \nabla(\,(1-\epsilon)\,\lambda_{s_{eff}}\nabla T_s\,) = \\ -\,\kappa_{s,g_{eff}}(\,T_s - T_v\,) \;-\; \kappa_{s,l_{eff}}(\,T_s - T_l\,) \;-\; \Gamma\,(\,h_{v,sat} - h_{l,sat}\,) \;+\; \dot{q}\end{aligned} \tag{4.8}$$

The conductive heat transfer in the solid phase must be expressed by an effective heat transfer coefficient λ_{eff}. Since in the cases of long term coolability no large temperature gradients have to be expected, a detailed modelling of λ_{eff} is not necessary, even in the case of particulate configurations. Thus, it may be replaced roughly by $\lambda_{eff} = \lambda_s(1-\varepsilon)$.

The energy conservation equations of the fluids are defined quite usual, with conductive and convective heat transfer with additionally considering the volume fractions.

$$\begin{aligned}\partial_t(\varepsilon\,(1-s)\,\varrho_v\,e_v) + \nabla(\varrho_v\,\vec{u}_v\,h_v) - \nabla(\varepsilon\,(1-s)\,\lambda_{v_{eff}}\nabla T_v) = \\ \kappa_{s,v_{eff}}(\,T_s - T_v\,) \;+\; \kappa_{l,g_{eff}}(\,T_l - T_v\,) \;+\; \Gamma\,h_{v,sat}\end{aligned} \tag{4.9}$$

$$\begin{aligned}\partial_t(\,\varepsilon\,s\,\varrho_l\,e_l\,) + \nabla(\,\varrho_l\,\vec{u}_l\,h_l) - \nabla(\,\varepsilon\,s\,\lambda_{l_{eff}}\nabla T_l\,) = \\ -\,\kappa_{l,v_{eff}}(\,T_l - T_v\,) \;+\; \kappa_{s,l_{eff}}(\,T_s - T_l\,) \;-\; \Gamma\,h_{l,sat}\end{aligned} \tag{4.10}$$

The last terms symbolise the energy loss or gain in the phases due to the evaporation process. Again, as in the solid energy equation, the effective heat conductivity λ_{eff} may be approximated by the homogeneous value weighted by the volume fraction.

4.2 Constitutive laws

For closure of the equation system several additional relations are necessary. These constitutive laws are in macroscopic scale, and mainly depend on semi-empirical correlations deduced from experiments.

As already mentioned before, a detailed formulation of the effective heat conductivities is not important because in the desired steady states all phases are nearly in thermal equilibrium. The same argument is valid for the heat transfer coefficients between the phases. So, a detailed description for these terms is not necessary here.

Only the heat transfer from the liquid to saturated water, yielding the evaporation, has to be modelled. In WABE-2D the evaporation rate is given by:

$$\Gamma = \frac{\Lambda(\alpha)}{h_{v,sat} - h_{l,sat}}\,(\,T_s - T_{sat}\,) \tag{4.11}$$

The simplest form of a parametric heat exchange is sufficient for the problem of long term coolability. Depending on the value of the heat transfer coefficient $\Lambda(\alpha)$ a small overheating of the particles occurs, while the heat transfered to evaporation is equal to the decay heat. When there is locally no more water left in a calculation cell the evaporation becomes zero, and the decay heat yields an increase in solid temperature. By this, non coolable zones can easily be detected. In the case of quenching of hot particles a more sophisticated formulation is necessary. In this case, for highly overheated

particles, a film-boiling model has to be used, while for only small overheating pool-boiling occurs. In WABE-2D a piecewise defined boiling correlation is implemented to include this.

The second constitutive law to be described here is the capillary pressure in the coolant-steam system. When two immiscible fluids are in contact in the interstices of a porous medium a discontinuity in the pressure exists due to surface forces across the interface separating them. This pressure difference is called the capillary pressure. Leverett [24] correlated this capillary pressure with characteristics of the porous media and a function depending only on the liquid volume fraction $s=1-\alpha$. He obtained:

$$p_c = p_v - p_l = \sigma \sqrt{\frac{\varepsilon}{K}}\, J(s) \tag{4.12}$$

Various semi-empirical formulations for the Leverett function J(s) can be found in the literature, and all describe the capillary pressure sufficiently accurate. In WABE-2D a correlation according Turland and Morgan [25] is used. A more detailed analysis additionally has to include the history in the two phase configuration, because in detail the capillary pressure shows hysteresis effects during dryout and drainage, respectively.

4.3 Description of the numerical solver

The coupled equation system described above, together with the friction laws presented in detail in the next chapter, are solved numerically in WABE-2D. A two dimensional rectangular grid is chosen for the discretisation. In this form either a rectangular geometry, or, by using the symmetry, a cylinder geometry can be represented. The equations are discretised using a finite volume method, where the conservation equations are balanced in the cell volume. For solving the coupled system an approach similar to the SIMPLE algorithm [26] for one phase flow extended to the case of two phase is used.

At the beginning of each step the evaporation rate Γ is calculated in each cell, based on the actual values of void and solid temperature. This rate is the mass source term for the vapour conservation equation and the sink for the liquid. Additionally, the energy necessary for evaporation is calculated yielding a sink term for the energy conservation equation of the solid.

In the next step the momentum equations are linearised and resolved to the respective superficial velocity. These velocities are defined on a staggered grid, and the scalar values in the terms are taken in an upwind scheme to avoid numerical problems. The

so resolved formulations are then inserted into the discretised mass conservation equations. The resulting two equation systems are combined into one large system, and solved for corrections of the pressure in the gas phase and the liquid volume fraction simultaneously. After correction of these variables the new pressure of the liquid phase and the volume fraction of the gas are calculated for every cell. Inserting these values in the momentum conservation equations then yield the new velocity fields.

After this step, the energy conservation equations of the three phases are solved sequentially yielding corrections for the enthalpy of the fluids and the solid temperature. As the equations are nonlinear, the whole procedure has to be repeated iteratively until the corrections are small enough.

Having reached a sufficient accuracy, the calculation is continued with the next time step. For the case that no convergence is reached within a number of iterations given by the program input, the time step is restarted with a reduced time step width. The time step width in WABE-2D will be adjusted to the number of iterations in the previous steps according input parameters. The time dependent development of the debris conditions can be calculated by this procedure. Steady states are reached when the results are not changing for a certain time.

5 Friction laws

5.1 One phase flow – Erguns's law

A simplified formulation of the momentum conservation equations can be deduced from the pressure loss of flows in porous media. This was first observed by Darcy [27] who showed that $\nabla p \sim j$ for laminar flows. Ergun [28] extended Darcy's law to higher velocities by adding the quadratic Forchheimer term to include a "turbulent" friction also including inertia effects:

$$\frac{\Delta p}{L} = \frac{\mu}{K}\, j + \frac{\varrho}{\eta}\, |j|\, j - \varrho\, g \tag{5.1}$$

The parameters K and η are called permeability and passability, respectively. According Ergun they can be calculated by:

$$K = \frac{\epsilon^3\, {d_p}^2}{A\,(1-\epsilon)^2} \qquad and \qquad \eta = \frac{\epsilon^3\, d_p}{B\,(1-\epsilon)} \tag{5.2}$$

where the Ergun constants A and B can be taken from pressure loss measurements in granular debris. Usually $A = 150$ and $B = 1.75$ are used. From the above definition it can be seen, that K and η only depend on parameters of the debris.

5.2 Classical models without explicit consideration of interfacial friction

For two phase flow in porous media the permeability and the passability have to be extended by a function depending on the volume fraction to consider the impact of the smaller effective cross section. In these relative permeabilities and passabilities the influence of the other fluid phase on the pressure loss is included.

$$\text{Vapour:} \qquad K \to K K_{rv}(\alpha) \qquad \eta \to \eta\, \eta_{rv}(\alpha) \tag{5.3}$$

$$\text{Liquid:} \qquad K \to K K_{rl}(1-\alpha) \qquad \eta \to \eta\, \eta_{rl}(1-\alpha) \tag{5.4}$$

Inserting this definition into the momentum conservation equations of the fluids leads to:

$$-\nabla p_l = \varrho_l\, \vec{g} + \frac{\mu_l}{K\, K_{rl}}\, \vec{j}_l + \frac{\varrho_l}{\eta\, \eta_{rl}}\, |\vec{j}_l|\, \vec{j}_l \tag{5.5}$$

for the liquid, and

$$-\nabla p_v = \varrho_v\, \vec{g} + \frac{\mu_v}{K\, K_{rv}}\, \vec{j}_v + \frac{\varrho_v}{\eta\, \eta_{rv}}\, |\vec{j}_v|\, \vec{j}_v \tag{5.6}$$

for the vapour phase. The interfacial friction is neglected in the classical models.

Several approaches for the relative permeability and passability, based on dryout heat flux experiments, can be found in the literature (see [29] for a summary of formulations). The most commonly used approach has the form:

$$K_{rv}(\alpha) = \alpha^n \qquad \eta_{rv}(\alpha) = \alpha^m \tag{5.7}$$

$$K_{rl}(\alpha) = (1-\alpha)^n \qquad \eta_{rl}(\alpha) = (1-\alpha)^m \tag{5.8}$$

The relative permeability K_r was determined experimentally for laminar flow conditions by Brooks and Corey [30]. Simplifying their results, Lipinski [4] used $K_r = \beta^3$ (β = phase fraction in the pores) and assumed the same exponent for the relative passability $\eta_r = \beta^3$ too. Based on his own dryout experiments yielding a smaller dryout heat flux, Reed [31] proposed an exponent $m = 5$ for the relative passabilities. This exponent was also used by Lipinski in later publications [32]. The dryout heat flux calculated with this approach fits the experimental values for top fed particulate bed configurations. This heat flux was measured for beds heated either by resistance or inductive heating, as well as in-pile by neutron irradiation in a reactor.

Usually the measuring procedure was iterative. By increasing the bed power, and observing the largest value before the temperature in any part of the bed starts to rise, the critical heat flux was determined. Theofanous criticised this measurement

	K_{rv}	η_{rv}	K_{rl}	η_{rl}
Lipinski	α^3	α^3	$(1-\alpha)^3$	$(1-\alpha)^3$
Reed	α^3	α^5	$(1-\alpha)^3$	$(1-\alpha)^5$
Theofanous	α^3	α^6	$(1-\alpha)^3$	$(1-\alpha)^6$

Table 5.1: Relative permeability K_r and passability η_r in the classical formulations

method [1], and explained that the resulting dryout heat flux values would be too high, because the power was increased further before the dryout was detected. Additionally, he pointed out, that in most of the experiments the ratio of the test section diameter to the particle diameter was too small, yielding an increased water inflow along the walls. So, he proposed an exponent $m=6$ to increase the friction between the fluids and the particles, yielding a smaller dryout heat flux. A summary of the classical models is given in table 5.1.

5.3 Models including explicit interfacial friction

As already Tutu [6] pointed out in his isothermal air/water experiments, an explicit consideration of the interfacial friction is necessary. In his experiments he used a one dimensional test column filled with stainless steel spheres. Into the water filled test column a defined air mass-flow was injected from below. The pressure loss inside the bed was measured. Additionally, the level swell of the water may be used to determine the void fraction inside the bed. As there is no net water flow, equation 5.5 without interfacial friction F_i directly yields, that the pressure gradient will always be the hydrostatic head, independently from the gas flow. But the measurements of the pressure gradient showed a significantly smaller value than the hydrostatic pressure gradient. This directly indicates the influence of the interfacial friction. The experiment and the results will be discussed in detail in section 6.1. So, equations 5.5 and 5.6 have to be extended by the interfacial friction, yielding the liquid equation:

$$-\nabla p_l = \varrho_l \vec{g} + \frac{\mu_l}{K K_{rl}} \vec{j_l} + \frac{\varrho_l}{\eta \eta_{rl}} |\vec{j_l}| \vec{j_l} - \frac{\vec{F_i}}{1-\alpha} \tag{5.9}$$

and the vapour equation:

$$-\nabla p_v = \varrho_v \vec{g} + \frac{\mu_v}{K K_{rv}} \vec{j_v} + \frac{\varrho_v}{\eta \eta_{rv}} |\vec{j_v}| \vec{j_v} + \frac{\vec{F_i}}{\alpha} \quad . \tag{5.10}$$

Based on similar experiments Schulenberg and Müller [33] correlated their data, and deduced an equation for the interfacial friction from the measured pressure loss and the liquid momentum equation 5.9:

$$F_i = 350\,(1-\alpha)^7\,\alpha\,\frac{\varrho_l K}{\eta\,\sigma}\,(\varrho_l-\varrho_v)\,g\,\left(\frac{j_v}{\alpha}-\frac{j_l}{(1-\alpha)}\right)^2 \tag{5.11}$$

Inserting this formulation for the interfacial drag into the vapour equation and assuming a relative permeability of $K_{rv}=\alpha^3$, Schulenberg and Müller determined the relative passability η_{rv} for the vapour phase. For the liquid phase they assumed the same exponents as Reed. Their result is:

$$K_{rv}(\alpha)=\alpha^3 \qquad \eta_{rv}(\alpha)=\begin{cases} 0.1\,\alpha^4 & : \quad \alpha \le 0.3 \\ \alpha^6 & : \quad \alpha > 0.3 \end{cases} \tag{5.12}$$

$$K_{rl}(\alpha)=(1-\alpha)^3 \qquad \eta_{rl}(\alpha)=(1-\alpha)^5 \tag{5.13}$$

A completely different approach has been proposed by Tung and Dhir [34]. Based on visual observation in air/water flow experiments of Chu et al. [5] they defined flow pattern ranges for bubbly, slug and annular flow. Besides a subpattern in the bubbly flow regime, only relevant for particle sizes greater than 12 mm, the flow pattern limits are given in table 5.2. Tung and Dhir defined a weighting function for the transition region between these flow patterns, such that the result is continuous to the first derivative at the connecting points:

$$W(\xi)=\xi^2(3-2\xi) \qquad \text{, where} \qquad \xi=\frac{\alpha-\alpha_i}{\alpha_{i+1}-\alpha_i} \tag{5.14}$$

Based on the definition of the permeability K and passability η in equations 5.2, Tung and Dhir used geometrical arguments, and inserted an effective porosity and particle diameter that is seen by the gas flow. This guided them to the following formulation for the relative permeability and passability of the gas for the different flow patterns:

Particle gas drag F_{pv}

$0 \le \alpha \le \alpha_3$ (bubbly and slug flow)

$$K_{rv} = \left(\frac{1-\varepsilon}{1-\varepsilon\,\alpha}\right)^{4/3}\alpha^4 \qquad \textit{and} \qquad \eta_{rv} = \left(\frac{1-\varepsilon}{1-\varepsilon\,\alpha}\right)^{2/3}\alpha^4 \tag{5.15}$$

$\alpha_3 \le \alpha \le \alpha_4$ (transition)

α_1	$\min\left(0.3\,,\,0.6\,(1-\gamma)^2\right)$	bubbly flow
α_2	$\frac{\pi}{6} \approx 0.52$	transition
α_3	0.6	slug flow
α_4	$\frac{\pi\sqrt{2}}{6} \approx 0.74$	transition
		annular flow

Table 5.2: Flow regime bounds of the Tung / Dhir model

$\alpha_3 \leq \alpha \leq 1$ (pure annular flow)

$$K_{rv} = \left(\frac{1-\varepsilon}{1-\varepsilon\,\alpha}\right)^{4/3} \alpha^3 \qquad \textit{and} \qquad \eta_{rv} = \left(\frac{1-\varepsilon}{1-\varepsilon\,\alpha}\right)^{2/3} \alpha^3 \tag{5.16}$$

Similar ideas for the liquid part are based on the visual observation that the liquid is alway in contact with the particles like a film. So they remain the particle diameter unchanged and only included an effective volume fraction. By this they deduced:

Particle liquid drag F_{pl}

$$K_{rl} = \eta_{rl} = (1-\alpha)^4 \tag{5.17}$$

It has to be noted, that the above given exponent is increased from 3 to 4 compared to the original paper, because the momentum equations 5.9 and 5.10 are divided by the volume fraction in this work, in contrast to [34].

Interfacial drag F_i

Additionally to the drag at the solid matrix, Tung and Dhir also deduced a correlation for the liquid/vapour interfacial friction F_i. For bubbly and slug flow this drag force is based on an expression for the drag on a single bubble or slug, multiplied by the number of bubbles or slugs per unit volume. A detailed description can be found in the original paper [34]. Here only the results will be given. The interfacial drag is defined by:

$$F_i = C_1 \frac{\mu_l}{D_b^2} (1-\alpha)\, j_r + C_2 \frac{((1-\alpha)\,\varrho_l + \alpha\,\varrho_v)}{D_b\,\varepsilon} (1-\alpha)^2\, |j_r|\, j_r \tag{5.18}$$

Here the relative velocity j_r is given by:

$$j_r = \frac{j_v}{\alpha} - \frac{j_l}{(1-\alpha)} \tag{5.19}$$

Based on visual observation Tung and Dhir defined the diameter of the bubbles or slugs by:

$$D_b = 1.35 \sqrt{\frac{\sigma}{g\,(\varrho_l - \varrho_v)}} \tag{5.20}$$

The friction coefficients are given separately for bubbly and slug flow:

$0 \leq \alpha \leq \alpha_1$ (bubbly flow)

$$C_1 = 18\,\alpha \qquad \text{and} \qquad C_2 = 0.34\,(1-\alpha)^3\,\alpha \tag{5.21}$$

$\alpha_1 \leq \alpha \leq \alpha_2$ (transition)

$\alpha_2 \leq \alpha \leq \alpha_3$ (slug flow)

$$C_1 = 5.21\,\alpha \qquad \text{and} \qquad C_2 = 0.92\,(1-\alpha)^3\,\alpha \tag{5.22}$$

$\alpha_3 \leq \alpha \leq \alpha_4$ (transition)

$\alpha_4 \leq \alpha \leq 1$ (pure annular flow)

In the annular flow regime the interfacial drag can be modelled in a manner similar to the particle-gas drag, by using the relative velocity between the gas and the liquid. This yields:

$$F_i = \frac{\mu_g}{K\,K_{rv}} (1-\alpha)\, j_r + (1-\alpha)\,\alpha \frac{\varrho_v}{\eta\,\eta_{rv}} |j_r|\, j_r \quad . \tag{5.23}$$

The relative permeability and passability to be inserted here are the same as for the gas-particle drag and are given in equation 5.15. As before, the transitions between the flow regimes are to be interpolated using the interpolation function defined in equation 5.14.

5.3.1 Modifications of the Tung/Dhir model

Tung and Dhir compared their model to the measured pressure gradients, as well as the void fractions of the isothermal air/water experiments of Chu et al. [5]. They found a good agreement with the experimental data. But, Chu et al. used relatively large particles of $d_p = 5.8\,\text{mm}$, $d_p = 9.9\,\text{mm}$ and $d_p = 19\,\text{mm}$ in their experiments. As already could be seen in the paper [34] for $d_p = 5.8\,\text{mm}$ data, the Tung/Dhir model seems to be not so good for smaller particles. Looking at the diameter of the gas bubbles used by Tung and Dhir, this discrepancy can easily be understood. Inserting the density difference between air and liquid as well as the surface tension into equation 5.20 yields a bubble diameter of $D_b = 3.75\,\text{mm}$. So, the applied bubble diameter becomes larger then the pores for small particles, in contradiction to the geometric ideas of the model. Additionally, the assumption of gas bubbles in the pores becomes questionable for small particles. This must lead to some modifications of the original Tung/Dhir model to extend it to smaller particle diameters.

The first central point to be modified is the diameter of the gas bubbles or the slugs. This diameter strongly influences the interfacial drag in bubbly and slug flow, as could be seen in equation 5.18. Based on the assumption of a cubic arrangement of spherical particles a maximum diameter of $D_{b_{max}} = d_p(\sqrt{2}-1)$ may be deduced for a bubble. To get a connection to the original Tung/Dhir model, a modified bubble diameter is simply defined by:

$$D_b^m = \min\left(1.35\sqrt{\frac{\sigma}{g\,(\varrho_l - \varrho_v)}}\ ,\ 0.41\,d_p \right) \quad . \tag{5.24}$$

The second point to be modified are the flow patterns ranges used in the model. The original bounds are given as dashed lines in figure 5.1. As can be seen, for particle diameters less then 3 mm no pure bubbly flow is expected. This fits the usual understanding too. But, in this work an even steeper reduction of the bubbly flow regime with decreasing particle diameter is proposed. On the other hand, annular flow in the picture of Tung and Dhir is via gas tubes wiggling along the pores. With decreasing particle size, these pores will get smaller, leading to smaller tube diameter. So, for small particles this "tube picture" becomes questionable. Now, in the annular flow regime fixed gas channels in the order of the particle size may establish. Inside a representative control volume, including several pores - in the mean - annular flow may establish even for smaller void fractions. This is also conform to the flow pattern observations characterised by Haga et al. [35] using tracer particles. They reported a channel like configuration for 2 mm spheres down to a void fraction of $\alpha = 0.3$. So, an

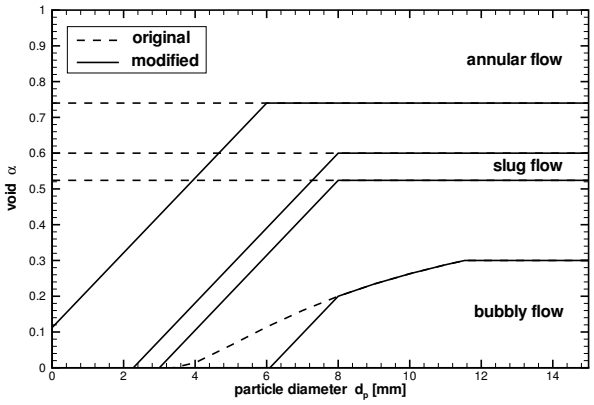

$$\alpha_1^m = \begin{cases} \frac{\pi/6}{5}(d_p - 8\,\mathrm{mm}) + \alpha_1 & : d_p < 8\,\mathrm{mm} \\ \alpha_1 & : d_p > 8\,\mathrm{mm} \end{cases}$$

$$\alpha_2^m = \begin{cases} \frac{\pi/6}{5}(d_p - 8\,\mathrm{mm}) + \alpha_2 & : d_p < 8\,\mathrm{mm} \\ \alpha_2 & : d_p > 8\,\mathrm{mm} \end{cases}$$

$$\alpha_3^m = \begin{cases} \frac{\pi/6}{5}(d_p - 8\,\mathrm{mm}) + \alpha_3 & : d_p < 8\,\mathrm{mm} \\ \alpha_3 & : d_p > 8\,\mathrm{mm} \end{cases}$$

$$\alpha_4^m = \begin{cases} \frac{\pi/6}{5}(d_p - 6\,\mathrm{mm}) + \alpha_4 & : d_p < 6\,\mathrm{mm} \\ \alpha_4 & : d_p > 6\,\mathrm{mm} \end{cases}$$

Figure 5.1: Flow pattern map for the modified Tung/Dhir model

enlargement of the annular flow range for particles less than 6 mm is proposed here. Consequently, the bounds for the slug flow regime have also to be modified, as this pattern becomes questionable for small particles too. Slugs will prefer flow paths in the wake of predecessors. The interfacial friction will then be less than for independent slugs. The modifications to the flow pattern bounds are also given in figure 5.1 by the solid lines.

Additionally, further modifications to the interfacial drag in the annular flow regime are necessary. As already discussed above, for smaller particles, a channel flow establishes. Compared to the classical picture of Tung and Dhir, the interfacial area between gas and liquid now is reduced. This motivates a decrease of the drag for decreasing particle diameter. By adaptation to the experimental results of Tutu et al. [6], discussed in detail in the next chapter, a multiplicative factor of $(d_p/6\text{x}10^{-3})^2$ is proposed for particles smaller than 6 mm in this work. Additionally, as can be seen in the formulation of the friction term for annular flow in equation 5.23, this drag decreases linearly to zero when the void fraction reaches the limit $\alpha \to 1$. This decent seems to be too weak compared to usual correlations. So, in this work an additional multiplier of $(1-\alpha)^2$ is proposed to get a more realistic decrease of the interfacial drag in the annular flow regime for increasing void fraction. This leads to the following modified formulation of the interfacial friction in the annular flow regime:

$$F_i^m = \left(\frac{\mu_g}{K\, K_{rv}} (1-\alpha)\, j_r + (1-\alpha)\, \alpha \frac{\varrho_v}{\eta\, \eta_{rv}} |j_r|\, j_r \right) * (1-\alpha)^2 \begin{cases} \left(\frac{d_p}{6\text{x}10^{-3}}\right)^2 & : d_p < 6\,\mathrm{mm} \\ 1 & : d_p > 6\,\mathrm{mm} \end{cases} \tag{5.25}$$

In general, all the modifications proposed above influence mainly the formulation of the interfacial drag. As will be seen in the next chapter, in general it is not easy to separate the different friction contributions in the experiments. Interfacial and particle drag are superimposed, but can be separated for specific conditions with no net water flow. On the other hand, for boiling beds - as in the reactor application - this splitting is not possible. So, one has to rely on the assumption, that the friction laws are valid here too. Comparisons to experiments with boiling beds will be given in the next chapter too. Especially the DEBRIS experiments described in chapter 6.2.2 support the above proposed modifications of the interfacial drag.

6 Comparison of the friction laws with experimental data

6.1 Comparison to isothermal Air/Water flow Experiments

Isothermal air/water experiments are a good method to investigate the friction laws of two phase flow in porous media with a simple experimental setup. By fixing the water and air flow rates through a vertical test column filled with particles, defined steady state conditions, either for co- or for counter-current flow, may be established. As the gas flow rate from the bottom to the top is fixed, a constant void fraction will establish over the whole bed height. Therefore the capillary pressure will be constant, and its gradient is zero. So, the same pressure gradient acts on both fluids. This pressure gradient in the test column can easily be measured. Additionally, the void fraction in the bed can be determined, either by visual observation through transparent vessel walls, or by the change of the water level on the top.

The experimental data can be compared to results of the theoretical models to verify the friction laws. For this, the momentum conservation equations 4.6 and 4.7 will be used in a dimensionless form. Dividing these equations by $g\varepsilon(\varrho_l - \varrho_v)$ yields:

$$(1-\alpha)\,P^\star = (1-\alpha)\,\frac{\varrho_l\, g}{g\,(\varrho_l - \varrho_v)} + F_{pl}^\star - F_i^\star \tag{6.1}$$

$$\alpha\,P^\star = \alpha\,\frac{\varrho_v\, g}{g\,(\varrho_l - \varrho_v)} + F_{pv}^\star + F_i^\star \tag{6.2}$$

with

$$P^\star = \frac{-\nabla p}{g(\varrho_l - \varrho_v)}\ , \qquad F^\star = \frac{F}{g\,\varepsilon\,(\varrho_l - \varrho_v)}\ . \tag{6.3}$$

By eliminating the normed pressure gradient one gets from equations 6.1 and 6.2:

$$\alpha\,(1-\alpha)\;+\;\alpha\,F_{pl}^{\star}\;-\;(1-\alpha)\,F_{pv}^{\star}\;-\;F_{i}^{\star}\;=\;0 \tag{6.4}$$

Inserting the friction laws presented in the previous chapter yields one equation with the three unknown j_v, j_l and α. For given superficial velocities, as adjusted in the experiment, the calculation of the void fraction requires an iterative process due to the functional dependence. It is much easier to fix one velocity, usually the liquid one, and vary the void fraction. Because the equation is just quadratic in the other velocity, the value can be calculated easily by selecting the physically relevant root. Additionally, adding the two equations 6.1 and 6.2 yields an equation for the pressure gradient:

$$P^{\star}\;=\;\frac{(1-\alpha)\varrho_l+\alpha\varrho_v}{\varrho_l-\varrho_v}\;+\;F_{pl}^{\star}\;+\;F_{pv}^{\star} \tag{6.5}$$

So, sets of j_v, j_l, $P^{\star}$ and α may be calculated and can directly be compared with the experimental values.

A direct comparison of model results with experimental air/water data measured by Tutu et al. [6] is shown in figure 6.1 and 6.2. A zero net water flow was adjusted for a particle bed consisting of stainless steel spheres with a diameter of $d_p = 6.35\,\mathrm{mm}$. Air was injected into the bottom of the column. The superficial velocity of the air, corresponding to the mass flux through the test column, was varied. For the established steady states the pressure gradient was measured by the difference of two pressure taps, one in the lower and one in the upper bed region. Additionally the void fraction in the bed was determined by the rise of the liquid level above the bed. In figure 6.1 the dimensionless pressure gradient is plotted over the superficial velocity of the gas. The figure shows that the pressure gradient becomes less than one, indicating a pressure loss due to the gas flow. The classical models, which do not explicitly consider the interfacial friction, can't reproduce this behaviour. This already can be seen clearly in the friction equation of the liquid phase (equation 6.1) by setting the superficial velocity of the liquid j_l to zero, leading to $F_{pl}^{\star}=0$. As in these models the interfacial friction $F_i^{\star}$ is zero too, this yields $P^{\star}=\varrho_l/(\varrho_l-\varrho_v)\approx 1$ for each gas mass flux. So, in these models the pressure field must always be equal to the hydrostatic pressure, and is not influenced by the gas flux. This behaviour is not verified by the experimental data, as can clearly be seen in figure 6.1. The measured pressure first decreases with increasing gas flow rate, although the water is still the continuous phase. This behaviour can only be explained by including the drag of the up-flowing gas on the liquid. The models of Schulenberg and Tung/Dhir, including this interfacial friction, show this characteristics qualitatively.

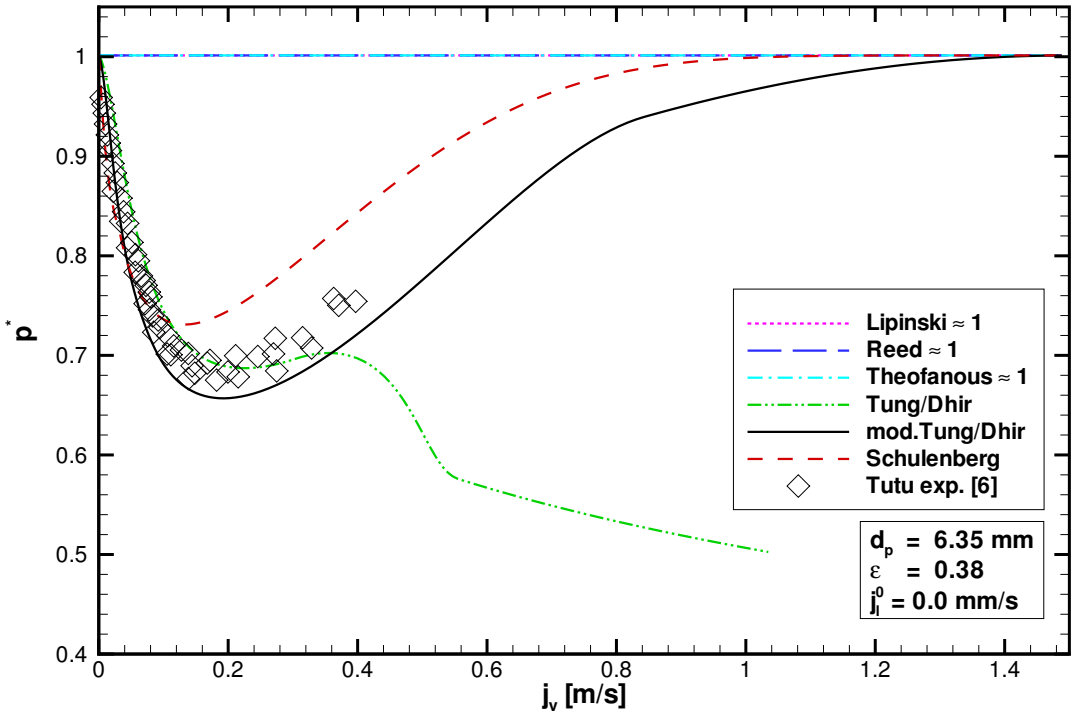

Figure 6.1: Comparison of the measured dimensionless pressure gradient for an isothermal air/water experiment with no net water flow and results from the theoretical models (exp. data taken from [6])

As already mentioned in the last chapter, the interfacial friction law in the annular flow regime of the Tung/Dhir model has to be modified to reach a reliable trend for large voids up to one. This can also be seen clearly in figure 6.1. With increasing gas flow rate the pressure gradient first strongly decreases below the hydrostatic one due to the drag of the upflowing gas bubbles and slugs on the liquid. Later, with further increased gas flow, the friction between the phases decreases again for void fractions greater than 0.5, due to the decreasing interfacial area between the gas and the water. This explains the increase in the normed pressure gradient for higher gas fluxes. As both fluid phases are regarded as continuous the limit is reached, when the gas replaces all the water. This is the case when the pressure loss due to the gas flow is equal to the hydrostatic head of the water, independent of the model. This limit is not reached for the original Tung/Dhir model. To compensate this, it was proposed in the previous chapter to multiply the interfacial friction by $(1-\alpha)^2$ in the annular flow regime, to get a cubic decrease for large void fractions. The comparison with the experimental data, as well as the development for high gas fluxes in figure 6.1, strongly supports this modification of the Tung/Dhir model.

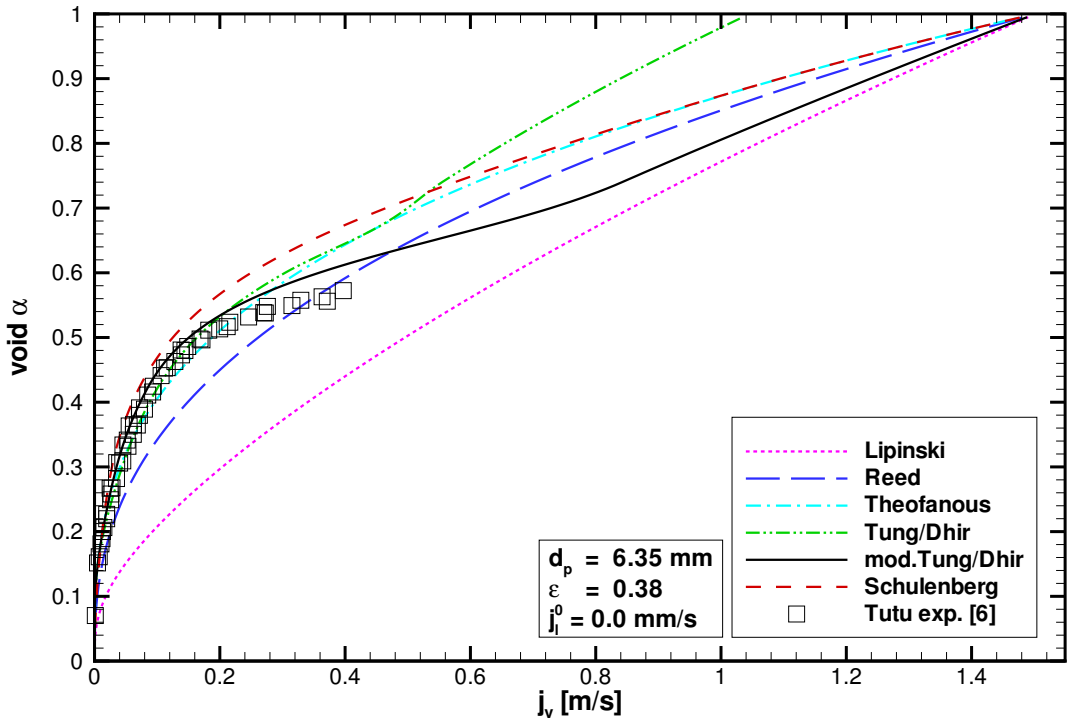

Figure 6.2: Comparison of the measured void fraction and results from the theoretical models in the case of figure 6.1

Similar conclusions can be drawn from the corresponding void data in figure 6.2. Although the experimental data points are not up to the annular flow regime, the modified Tung/Dhir model fits the experimental points better. This is due to the decreased bubble diameter in the slug and bubbly flow regime ($D_b = 2.6\,\text{mm}$ modified instead of 3.75 mm in the original form), yielding an increased interfacial friction. Additionally, as already described for the pressure gradient, the tendency in the annular flow regime for the original Tung/Dhir formulation is again not explainable. The one-phase flow limit with $\alpha = 1$ should be reached at the same gas velocity for all models, independent of the interfacial friction. The modified formulation, with decreased interfacial friction in the annular flow regime, fullfills this condition.

For the special case with no net water flow in the porous medium ($j_l = 0$) an enhanced analysis is possible. The interfacial friction can directly be deduced from the measured pressure gradient and void fraction via the liquid momentum equation given in 6.1. The results for the described data together with the results of the various models are given in figure 6.3 in respect to the gas velocity and the void fraction, respectively. While the interfacial friction is always zero for the classical models, a principle agreement of the enhanced models with the experimental data can be seen. But, especially the hunch

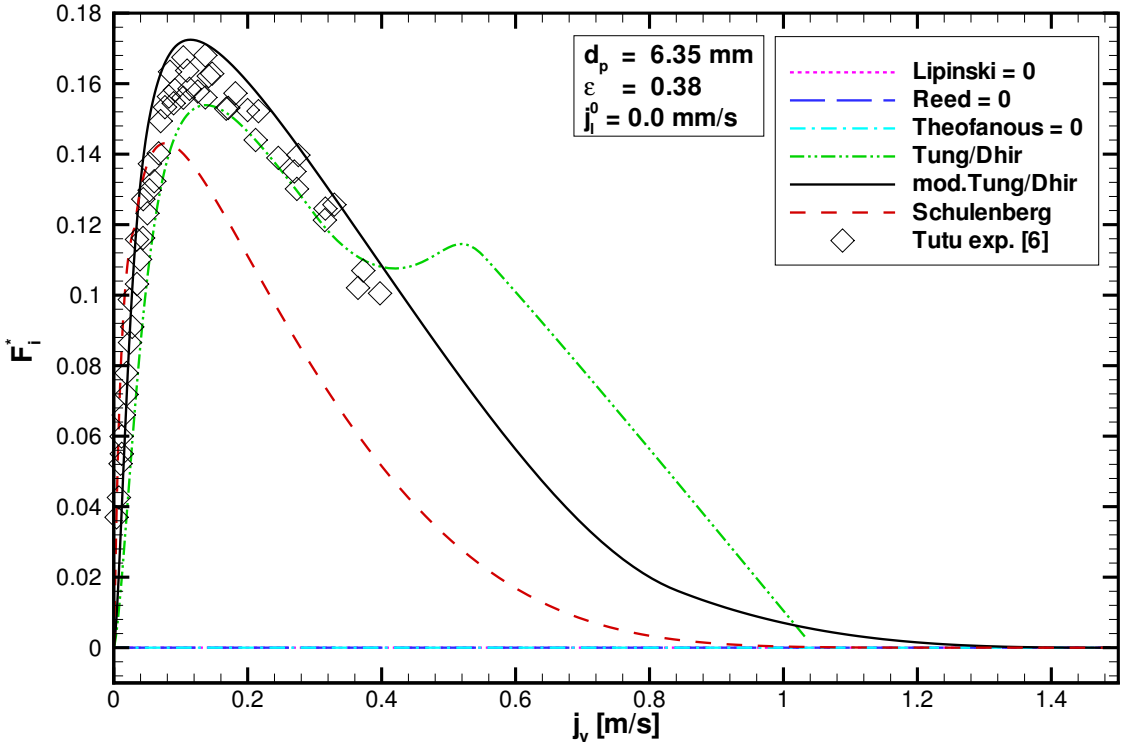

(a) F_i as function of the superficial gas velocity

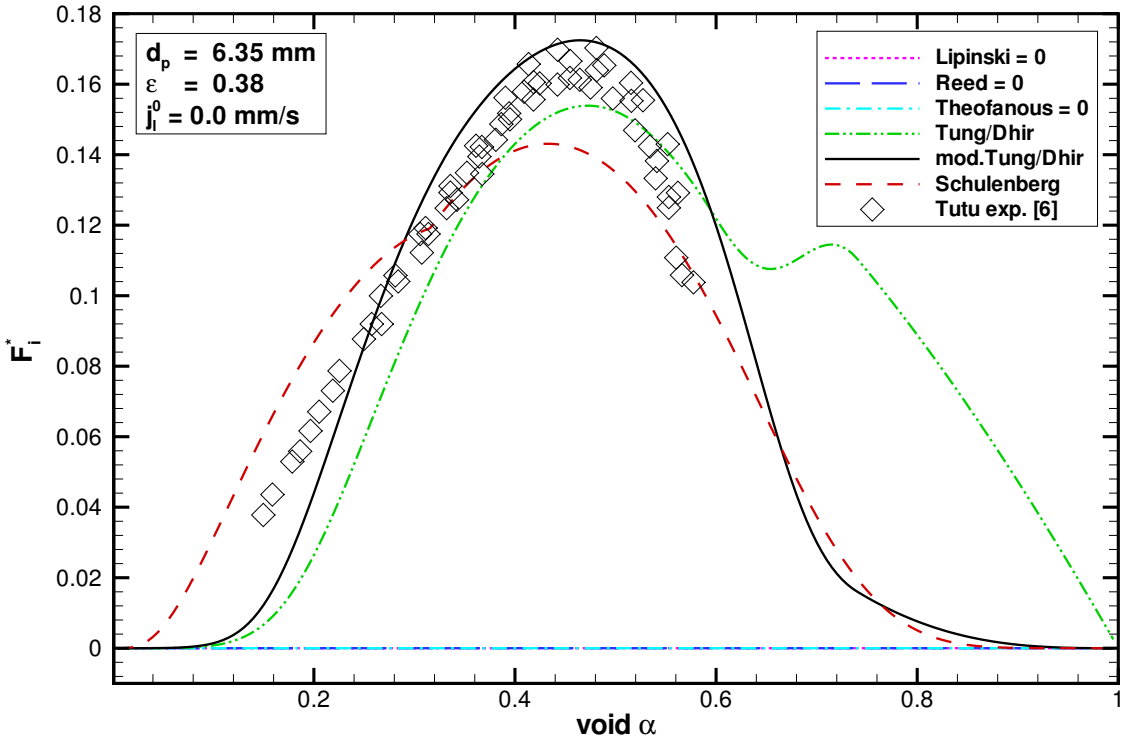

(b) F_i as function of the void

Figure 6.3: Comparison of experimentally and theoretically deduced dimensionless interfacial friction in the case of figure 6.1 and 6.2

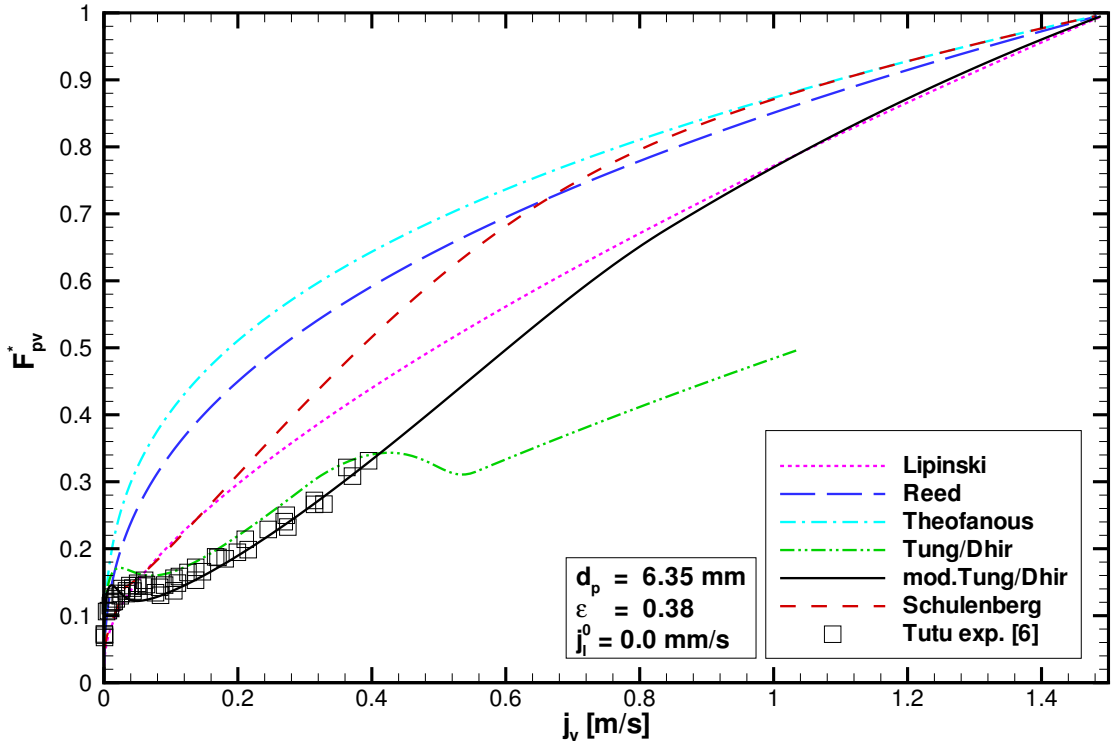

Figure 6.4: Dimensionless particle gas drag F^*_{pv} in the case of figure 6.1

in the original Tung/Dhir formulation seems not to be verified by the experiment. This hunch originates in the annular flow regime. Furthermore, as already mentioned, the linear decrease of $F_i^\star$ for $\alpha \to 1$ is unreliable. These faults are eliminated by the modifications of the Tung/Dhir model proposed in chapter 5.3.1, which then yields the best estimate for the experimental data.

By inserting the so determined interfacial friction, the measured pressure gradient and the void into the momentum equation of the gas phase (equation 6.2), the particle gas drag can be obtained. The resulting data for this case, together with results of the different models, are plotted in figure 6.4. Again, the original Tung/Dhir model yields the wrong limit value for the transition to one-phase gas flow. Modifying the interfacial friction as proposed in chapter 5.3.1 fits this limit condition and also the experimental data. So, in the whole system, the formulation of the interfacial friction has an influence on the local pressure and the void fraction, and by this also on the particle gas drag. A direct comparison of the measured drag forces - the particle and the interfacial drag - in the gas momentum equation is given in figure 6.5. As can be seen, the interfacial drag is of the same order as the drag of the gas flow at the particles. So, both drag terms must be considered separately by the models.

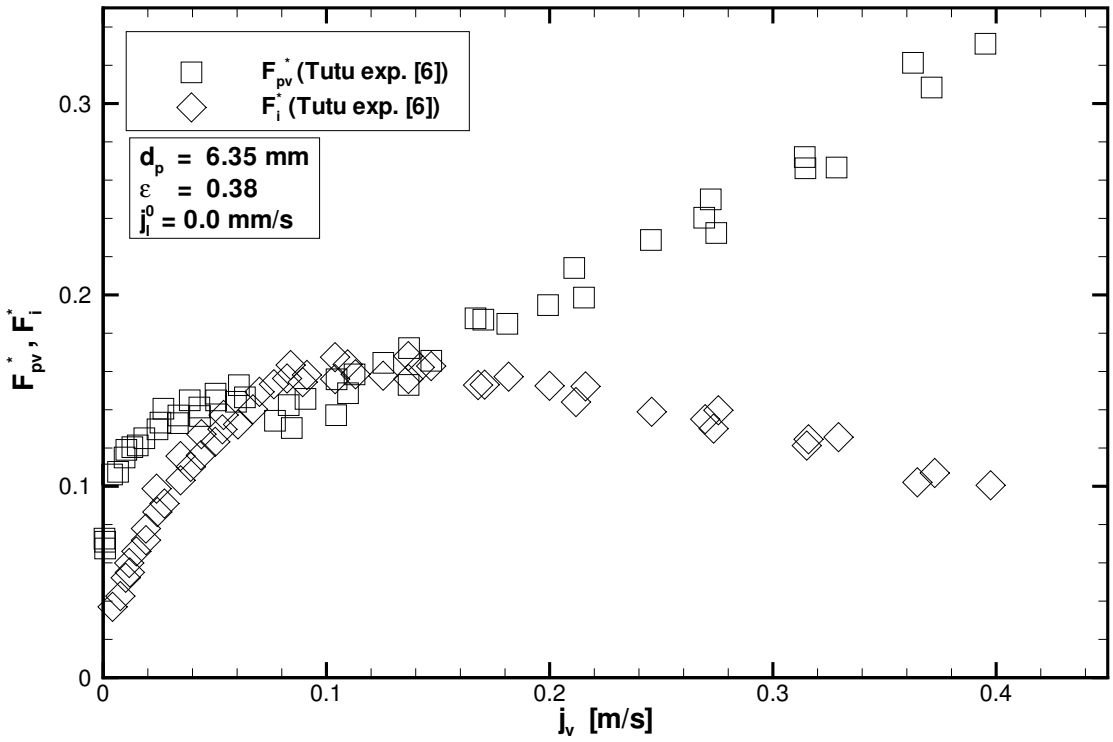

Figure 6.5: Comparison of the experimentally determined particle and interfacial drag of the gas flow (taken from [6])

Measurements for larger particles with a diameter of $d_p = 12.7\,\text{mm}$ yield similar results, as can be seen in figure 6.6. For particles of this size, the flow regime limits in the modified version of the Tung/Dhir model are the same as in the original formulation. This is to be expected, because the flow patterns originally used by Tung and Dhir are based on visible observations of similar isothermal air/water flow experiments in co- and counter-current flow configurations, but with larger particle diameters between 5.8 mm and 19 mm performed by Chu et al. [5]. Experimental results of Chu et al., again with no net water flow, for particles with $d_p = 9.9\,\text{mm}$ are given in figure 6.7. In principle these results show the same behaviour as described above, especially the decrease in the pressure gradient for increasing gas flux. Only the measurements for the largest gas flow rates seem to support the original formulation of Tung and Dhir. But, as already discussed, the limit for $\alpha \to 1$ is not plausible in this formulation.

The enhanced models, that include the interfacial friction term explicitly, yield satisfying results compared to the experimental data for larger particles. Especially the Tung/Dhir formulation - after the modifications proposed in the previous chapter - fits the data well. For smaller particle diameters, which are to be expected during a severe accident in a nuclear power plant, the models show more differences compared

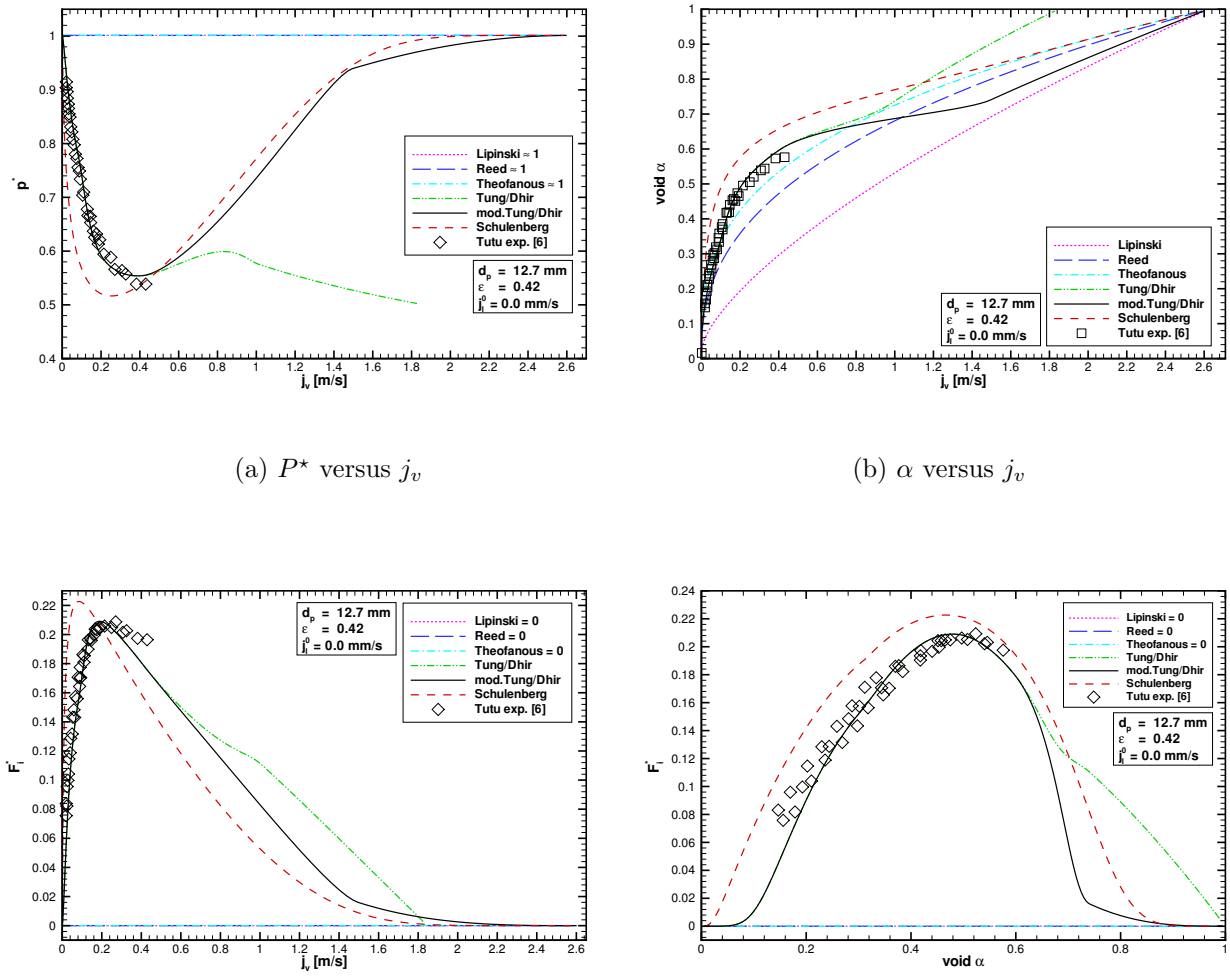

(a) $P^\star$ versus j_v

(b) α versus j_v

(c) F_i versus j_v

(d) F_i versus α

Figure 6.6: Experimental and theoretical results for air injected into a water filled column of 12.7 mm particles (exp. data taken from [6])

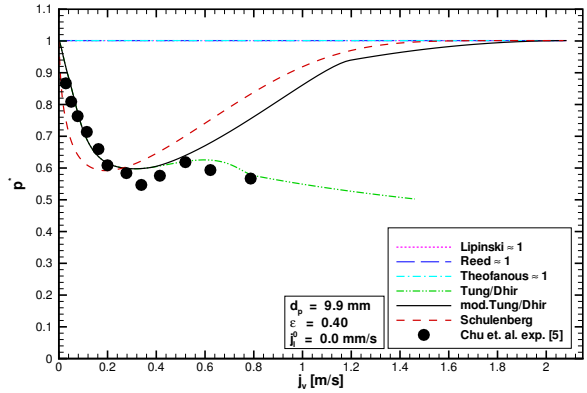

(a) $P^\star$ versus j_v

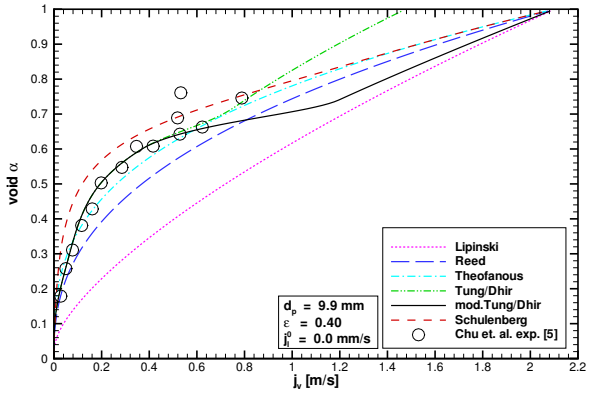

(b) α versus j_v

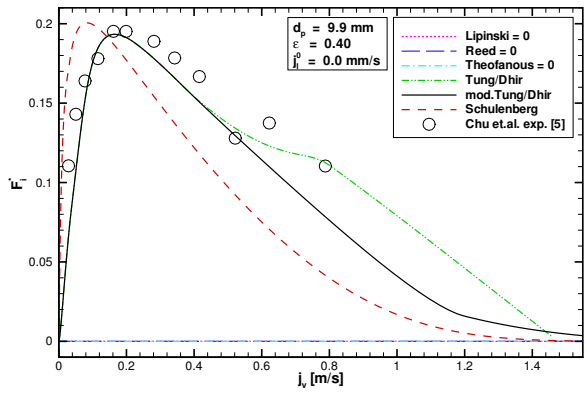

(c) F_i versus j_v

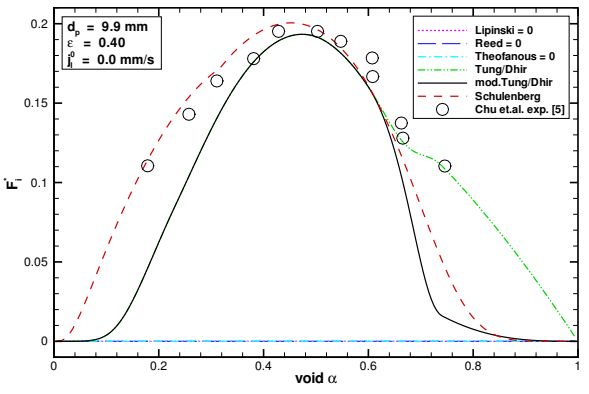

(d) F_i versus α

Figure 6.7: Experimental and theoretical results for air injected into a water filled column of 9.9 mm particles (exp. data taken from [5])

	original Tung/Dhir	modified Tung/Dhir
bubble diameter	3.75	1.30
upper limit for pure bubbly flow	0.	0.
lower limit for pure slug flow	0.52	0.02
upper limit for pure slug flow	0.6	0.1
lower limit for pure annular flow	0.74	0.45

Table 6.1: Model parameters for the original and the modified Tung/Dhir formulation for $d_p = 3.18\,\text{mm}$ particles

to the experimental data. This can already be seen in the original paper of Tung and Dhir [34] for a particle diameter of 5.8 mm. Unfortunately, for this diameter pressure gradients only with net water flow in a counter-current flow configuration are reported in the paper (see below).

Beside particle diameters of 6.35 mm and 12.7 mm Tutu et al. [6] also performed experiments for smaller particles with $d_p = 3.18\,\text{mm}$, again without water flow. The described modifications that have been introduced into the original Tung/Dhir model - especially the modifications of the flow pattern limits and the modified slug size - are seen to be of decisive influence for smaller particle sizes. Additionally, the interfacial friction in the annular flow regime was reduced for particle diameters less than 6 mm. A summary of the changed parameters is given in table 6.1. As can be seen in figure 5.1, the annular flow regime in the modified formulation is extended to lower voids, while the pure bubbly flow region disappeared. This is obviously plausible because the pores are too small for the bubbles. On the other hand, slugs will move in the wake of the predecessor, and, with increasing gas flow rate, will form channels in the bed. This is also compatible to the flow patterns described by Haga et al. [35]. For particles with a diameter of $d_p = 2\,\text{mm}$ they visually observed a channel flow for voids above $\alpha = 0.3$.

The calculated void and the dimensionless pressure gradient for a particle diameter of 3.18 mm are given and compared to the experimental data of Tutu et al. in figures 6.8 and 6.9. The influence of the interfacial friction again can be seen in the pressure gradient. The decrease in the pressure gradient with increasing gas flow rate is only reproduced by the enhanced models including the interfacial friction explicitly. But, the further measured increase for higher gas fluxes is steeper than expected from these models. Looking additionally at the void development, only the modified Tung/Dhir model yields satisfying results. This can even better be seen for the interfacial friction, given in figure 6.10 over the gas velocity and over the void fraction, respectively.

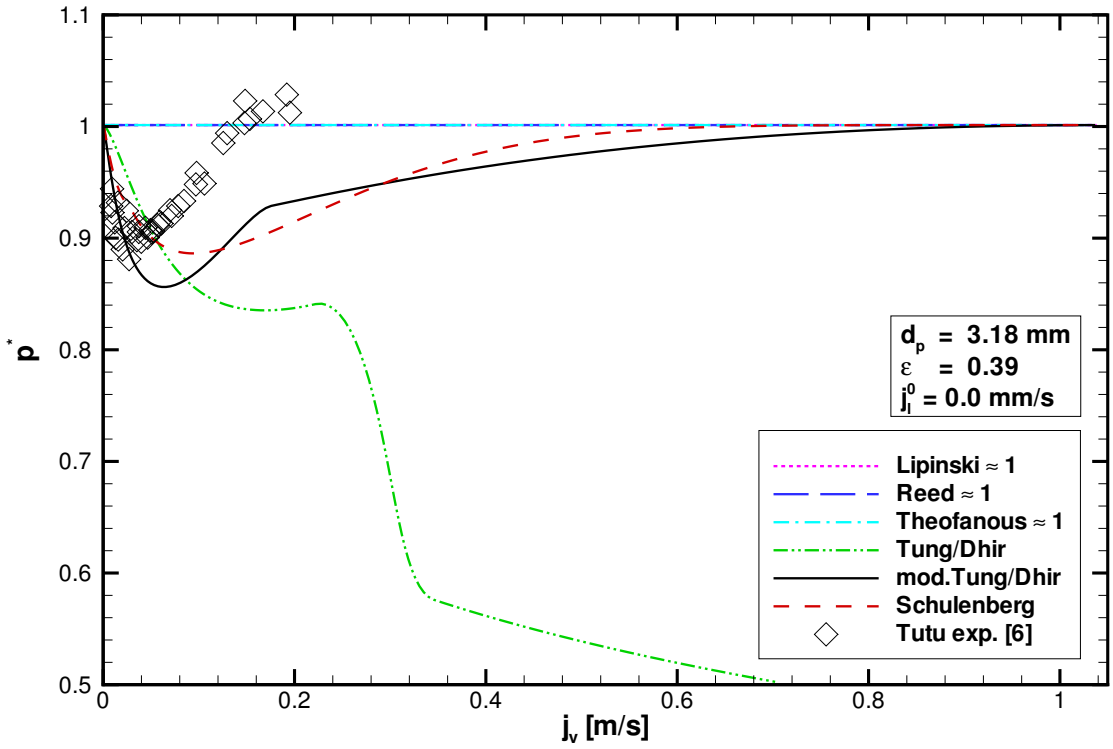

Figure 6.8: Dimensionless pressure gradient for air injected into a water filled column of 3.18 mm diameter particles (exp. data taken from [6])

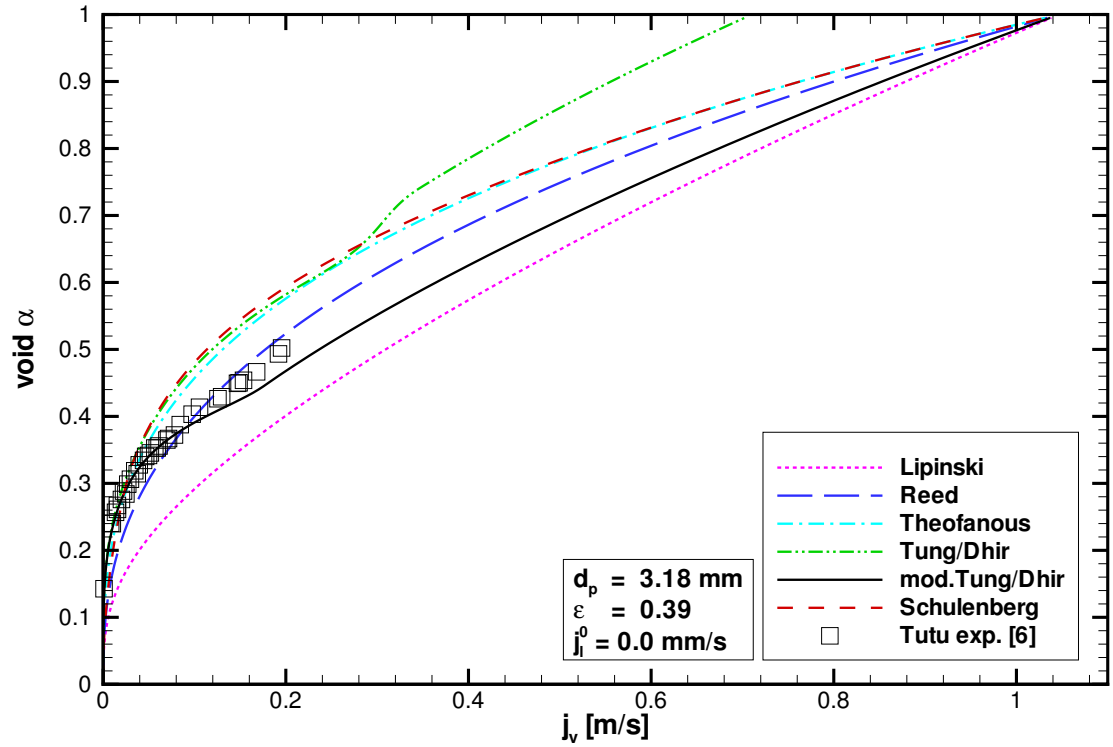

Figure 6.9: Void fraction for air injected into a water filled column of 3.18 mm diameter particles (exp. data taken from [6])

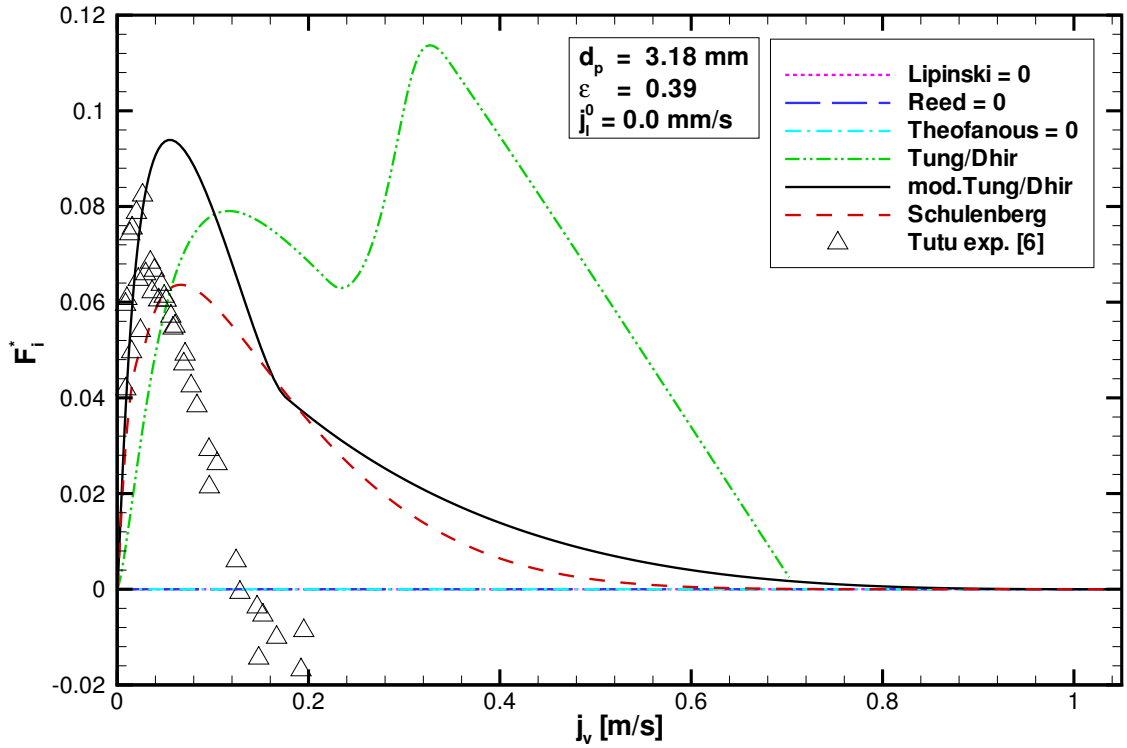

(a) F_i as function of the superficial gas velocity

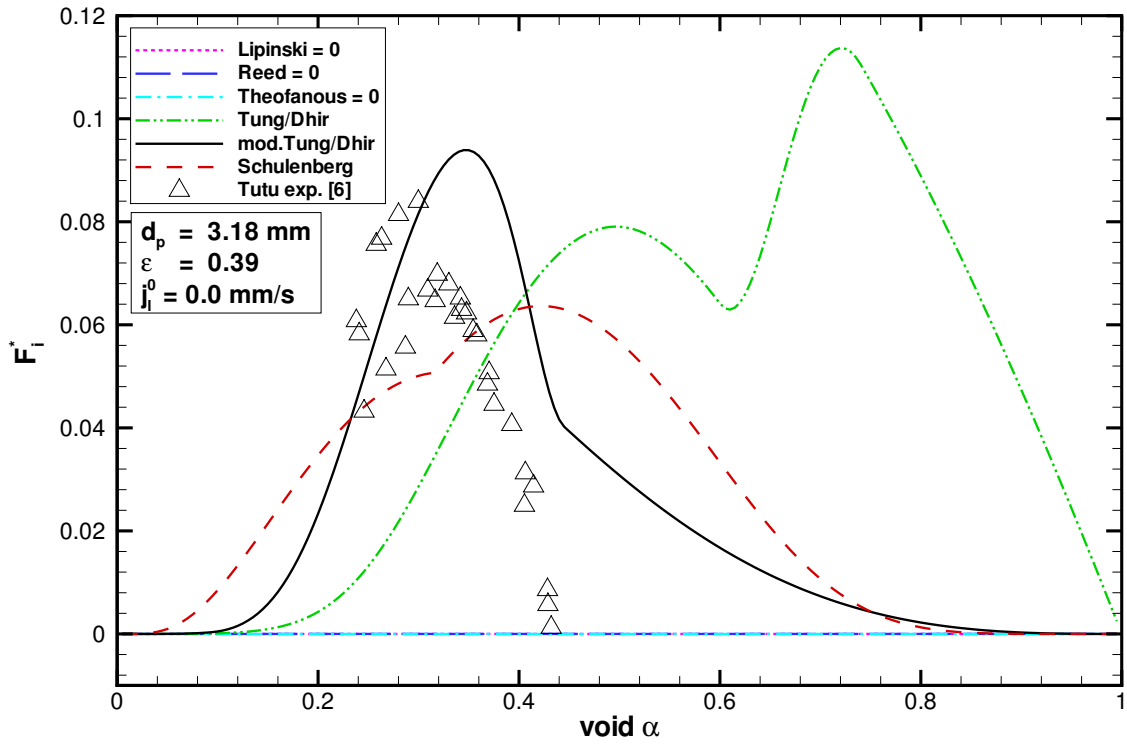

(b) F_i as function of the void

Figure 6.10: Comparison of experimentally and theoretically deduced dimensionless interfacial friction in the case of figure 6.8 and 6.9

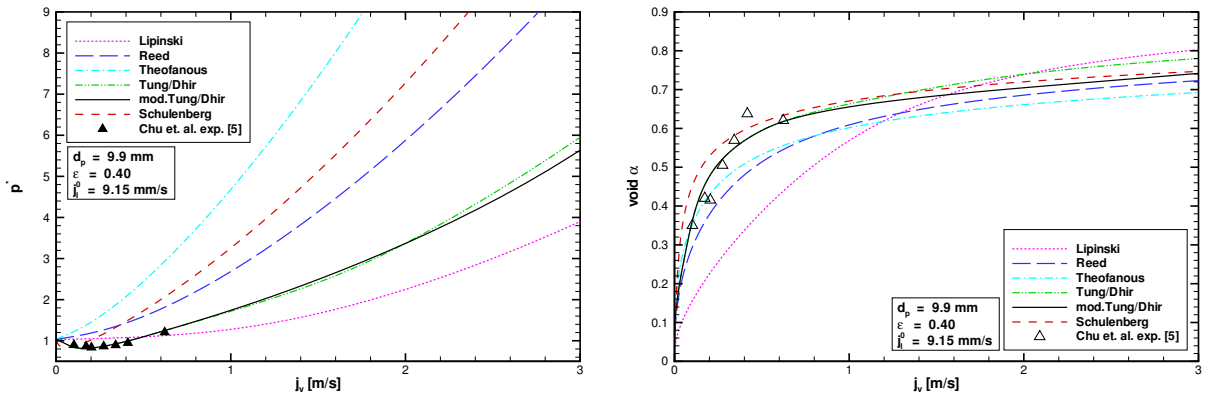

Figure 6.11: Dimensionless pressure gradient (left) and void fraction (right) in a column filled with 9.9 mm diameter particles for co-current flow with constant water flow rate (exp. data taken from [5])

Especially for voids greater then $\alpha = 0.5$ the measured interfacial drag is zero (the negative values in figure 6.10 (a) indicate a measure for the experimental error). This can only be explained in the flow pattern picture with the transition to a channel like configuration with only minor contact of gas and water, as described by Haga et al. [35]. The interfacial friction is strongly reduced because of the reduced interfacial area in this flow pattern. In the modifications to the Tung/Dhir model proposed in the previous chapter this reduction is included in the redefined lower limit for the annular flow regime and in the reduction of the interfacial friction with the particle diameter in this pattern. The modifications to the original Tung/Dhir model therefore gain importance for smaller particles, which are to be expected for the particulate debris during a severe accidents in a nuclear power plant.

Chu et al. also performed experiments with a net water flow in co-current as well as in counter-current configuration, but still with larger particles. The co-current results, with water and air injection into the bottom, confirm the above results in principle. As an example, results for a fixed water superficial velocity are given in figure 6.11. As, per definition, the net water flow is fixed, the void limit of $\alpha = 1$ can not be reached in this case. Increasing the gas mass flux yields an increasing pressure gradient, that presses the fluids through the porous structures, as can be seen in the figure.

More interesting with respect to debris coolability is the counter-current flow configuration, where water is added to the top and exhausted from the bottom of the test section, yielding a top to bottom flow. Then the bottom injected gas and exhausted water are in counter-current mode, similar to the case of a boiling bed with a coolant pool on the top. Again, for fixed water mass flux, the air inlet rate is varied. Results

of the measured pressure gradient and void fraction, as well as the corresponding theoretical results are given in figures 6.12 and 6.13. In contrast to the co-current case, an upper limit for the gas superficial velocity exists, corresponding to a maximum gas mass flux. This limit is the counter-current flooding limit. No larger gas fluxes than this limit are possible in such a configuration. Looking at the void fractions in figure 6.13 it can be seen, that this value corresponds to a maximum void fraction. This fraction can't be one, because a certain amount of the cross-section or volume is necessary for the water flow. A further increase of the gas flow rate thus would hinder the water flow.

The counter-current flooding limit is directly linked to the coolability of porous structures with an overlying coolant pool. In a boiling bed the dryout heat flux corresponds to the critical steam flux. This limit is reached near the top, where the steam flux as well as the downflowing water flux are highest. The friction at this bottleneck - the location of highest steam fraction - is decisive for the coolability of the whole bed. As already can be seen in the isothermal results, a combination of j_l, j_v, α and $P^\star$, establishes at that limit. In a boiling bed the water flux is not fixed, but is linked to the steam flux due to the mass conservation for steady state conditions. By this a similar limit is defined.

The development of the classical models to obtain the measured dryout heat flux can also clearly be seen in the figure. The first approach from Lipinski yields a dryout heat flux higher than measured for top cooled particulate beds. Then by increasing the friction in the relative passability, as done by Reed, this critical heat flux was better reproduced. In figure 6.12 and 6.13 this can be seen by the smaller maximum reachable gas velocity. As already mentioned, Theofanous [1] criticised the published dryout heat flux data due to the measuring procedure, and consequently introduced even stronger particle fluid friction. As shown in the figures this adaptation process can also be seen in the isothermal air/water experiments. But, looking at the pressure gradient versus the gas flow rate in figure 6.12 one sees, that this adjustment does not represent the measured pressure losses. These can only be explained by including the interfacial friction, just as in the case with no net water flow. As in the classical models, the counter-current flooding limit - corresponding to the dryout heat flux in boiling beds - depends on the detailed formulation. Again, the modified Tung/Dhir model is in good agreement with the experimental data.

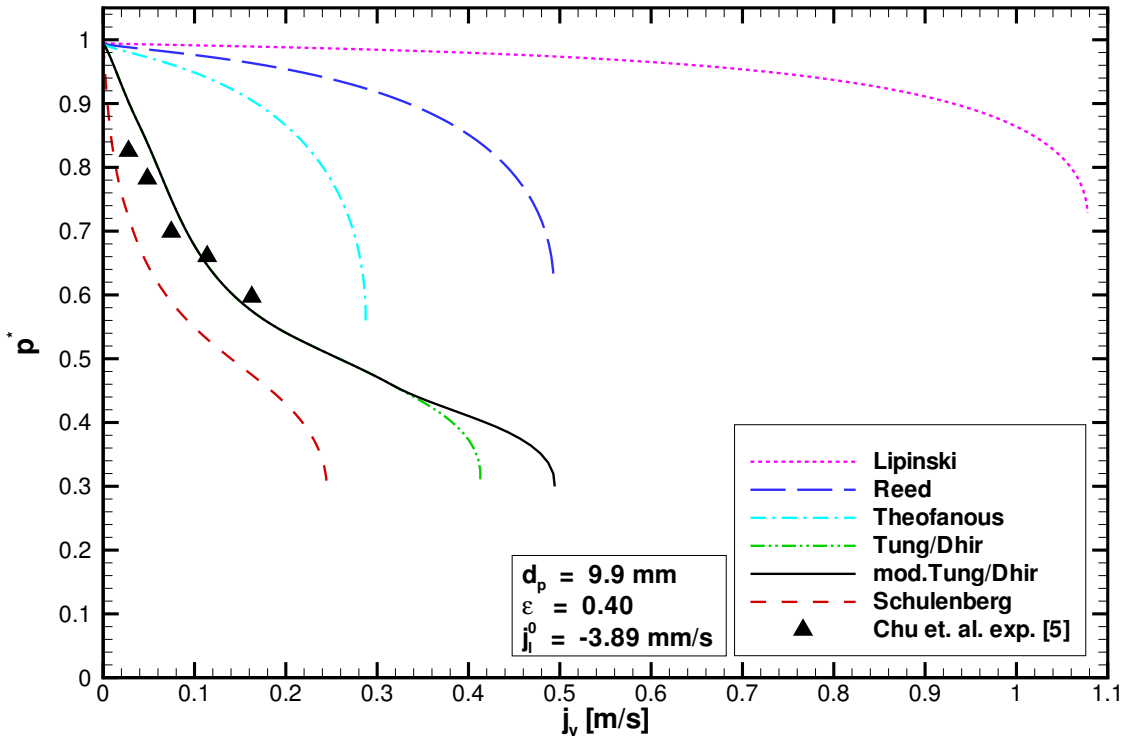

Figure 6.12: Dimensionless pressure gradient in a column of 9.9 mm diameter particles for counter-current flow with constant water flow rate (exp. data taken from [5])

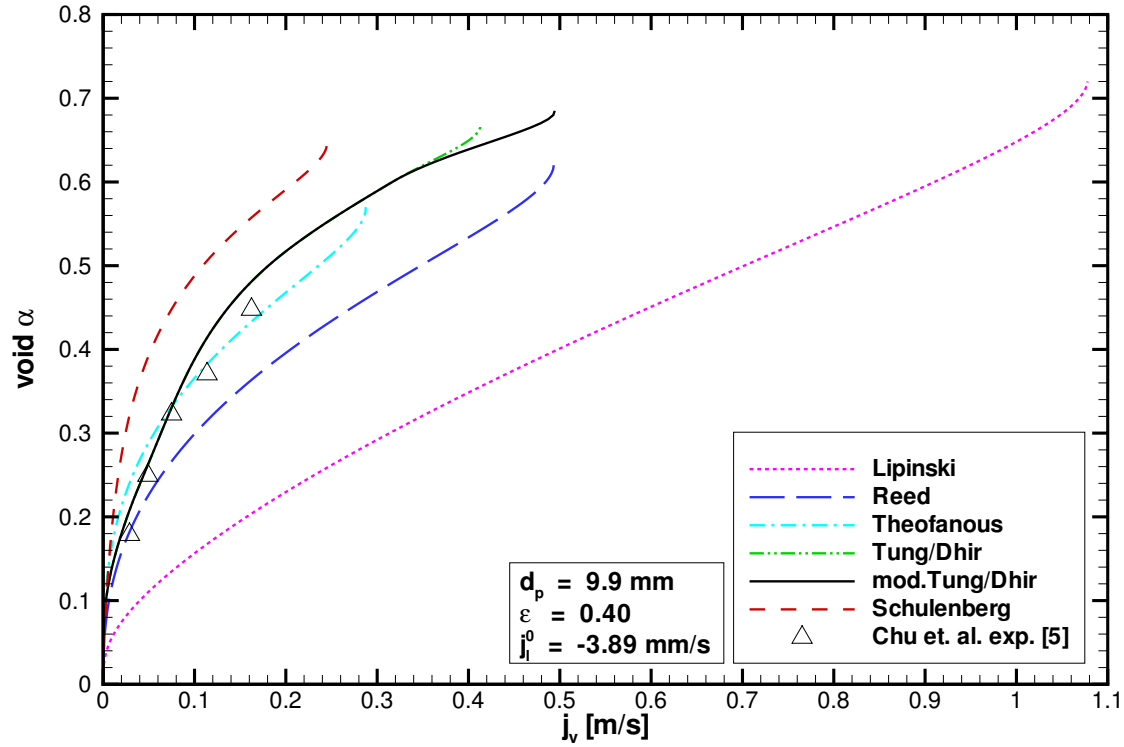

Figure 6.13: Void fraction in a column of 9.9 mm diameter particles for counter-current flow with constant water flow rate (exp. data taken from [5])

6.2 Comparison to experiments with boiling debris beds

In contrast to the isothermal air/water experiments, the local flow rates vary inside a boiling bed, even in a one dimensional configuration. The local gas flux, driven by buoyancy forces, is determined by the integrated steam flux, and thus by the bed power integrated from the bottom. For a homogeneous power distribution the steam mass flux is given by $\varrho_v j_v(z) = Q\, z/LH$, where Q is the volumetric power density and $LH = h_v - h_l$ is the specific latent heat of the evaporation. In a steady state the corresponding local water flux is directly given by the mass conservation equation. Assuming water inflow just from a pool above the bed, the liquid mass flux follows from $\varrho_l j_l(z) = -\varrho_v j_v(z)$.

6.2.1 Application to DHF experiments

Various experimental programs for direct investigation of the dryout heat flux for volumetrically heated porous structures have been performed, especially at the beginning of the 1980's. In most of these experiments the particulate debris consists of inductively heated metallic spheres in a one dimensional test column. Some authors used real granular particle beds (e.g. Theofanous [1]), and applied direct electrical resistance heating. In other experiments the particles are heated by irradiation (e.g. DCC experiments [3]). The coolant, mostly water, infiltrates from a pool at the top. The dryout heat flux in such configurations was determined by increasing the bed power in steps, until somewhere in the bed a local dryout is detected by an increase of the temperature. Slightly above the limiting bed power a first dryout has to be expected after a very slow transient near the bottom of the test column. As already pointed out by Hu and Theofanous in [1], the measurement procedure described above may yield too high values, because the power is further raised before detecting the dryout. So, they proposed to start from a steady state slightly below the critical power, then increase the power beyond the limit, and measure the time until the first dryout is detected in the bed. The critical heat flux is determined from several of such measurements with different power steps by interpolating the data points to infinite time before reaching local dryout.

Another problem of the measurements, also mentioned by Hu and Theofanous, is the fact, that the porous structure is disturbed at the walls of the test column. The increased porosity at the walls yields locally reduced friction, leading to a multidimensional flow configuration. This effect has to be suppressed in the experimental setup.

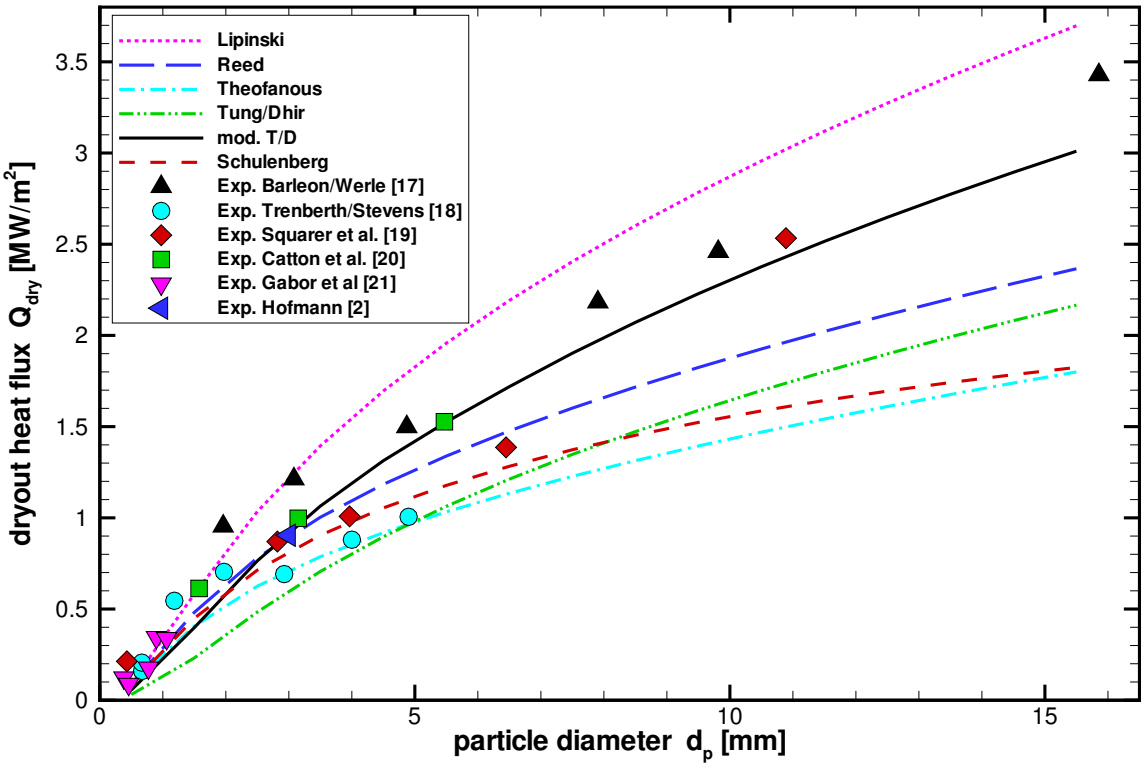

Figure 6.14: Experimental dryout heat flux in top fed beds for different particle diameters and results from the theoretical models

To get comparable results, additionally a homogenous distribution of the heating power has to be established.

Results of measurements for the commonly used conditions described above can directly be compared for different parameters. The dryout heat flux versus the particle diameter - measured by various authors for a system pressure of 1 bar - is shown in figure 6.14 together with results of the different friction models. In general, it can be seen that the different experiments yield some spread in the published data. This is due to different experimental setup and measurement procedures. In the models the dryout heat flux corresponds to the counter-current flooding limit, and therefore depends on the drag at this limit, as already discussed. A general statement on the validity of the models only based on these values is not possible. However, the tendency to yield smaller dryout heat fluxes can be seen with increasing friction in the classical models from Lipinski over Reed to Theofanous. While the commonly used Reed model looks good for small particles, the measured DHF values are higher than predicted for larger particles. A good representation of the data over the whole range is again given by the modified Tung/Dhir model. So, these results support again the modifications proposed in chapter 5.3.1.

For configurations with enhanced coolant inflow possibilities the dryout heat flux will increase. In a pure 1D setup, as regarded here, additionally to the coolant from the pool at the top, inflow via the bottom has to be considered. In the view of the coolability in a water environment this inflow is driven by the hydrostatic head of a coolant column as shown in figure 3.5. The inflow rate is then determined by the pressure gradient at the bottom, and therefore by the pressure field in the porous media. In the different models this pressure field strongly depends on the drag terms inside the particle bed. The inflow from below is favoured, because of the small void fractions there, yielding a reduced coolant-particle friction. Additionally, this coolant inflow is supported by the drag of the up flowing steam. So, the interfacial drag has to be modelled explicitly to consider both configurations, the pure top fed as well as the bottom fed case, because in the first one it hinders the coolability while supporting it from below. In contrast to the top fed case, now the dryout will not occur at the bottom. The evaporated water for a main part of the bed will inflow via the bottom, and only some water may infiltrate from the top. The void now is not limited by a maximum value, as in the top fed case. The up-flowing water will be reduced on its way by evaporation up to a level, where all is spent. Only the region above this level is cooled from above, and may be regarded as a top fed configuration with gas inflow from below.

Only two experiments with such inflow conditions are known. Stevens and Trenberth [36] used spheres with a diameter between 0.126 mm and and 5 mm while Hofmann [2] used only a particle diameter of 3 mm. These experiments show an increase of the dryout heat flux by a factor between 1.5 and 3. The measured values are given in figure 6.15 together with results of the different models. The first point to be noticed is valid for all models. Compared to the top fed case the dryout heat flux is increased because of the facilitated water inflow from below, as expected. But especially the data of Hofmann shows a much stronger increase, than calculated by

	L	R	T	TD	mTD	S
dryout heat flux (top fed)	1.22	0.90	0.71	0.60	0.93	0.82
dryout heat flux (top/bottom fed)	1.48	1.22	1.01	2.00	1.42	1.58
DHF_{bottom} / DHF_{top}	1.21	1.35	1.42	3.34	1.53	1.94
flow rate from below (j_l [mm/s])	0.564	0.454	0.374	0.925	0.642	0.725
level fed from below [%]	0.825	0.807	0.801	0.999	0.976	0.990

Table 6.2: Theoretical dryout heat flux for top and bottom fed configurations with a particle diameter of $d_p = 3$ mm (L: Lipinski; R: Reed; T: Theofanous; TD: original Tung/Dhir; mTD: modified Tung/Dhir; S: Schulenberg)

the classical models. The interfacial drag in the enhanced models additionally favours the water inflow from below, while hindering it from the top. Here the influence of the bottom inflow is much stronger. A summary of calculated results of the different models for a particle diameter of $d_p = 3\,\mathrm{mm}$, corresponding to the Hofmann experiment, is given in table 6.2. As can be seen, the ratio of bottom to top dryout heat flux (DHF_{bottom} / DHF_{top}) is more pronounced for the enhanced models. For these, almost all water evaporated in the particle bed is flowing via the bottom into particulate bed. This can be seen in the table at the level that is fed from below. The gain in coolability is most significant for the original Tung/Dhir formulation, but this is also effected by the very low top fed value. For the top fed configuration Hofmann reported a dryout heat flux of $q_{dry} = 92\,\mathrm{W/m^2}$. Comparing this with the table one notes that Reed for the classical models and Schulenberg as well as the modified Tung/Dhir formulation yield satisfying results. But, the value for additionally bottom inflow is better reached for the enhanced models. In general it is not possible to tune the particle-fluid drags in the models without interfacial friction to fit the top as well as the bottom fed configuration. So, the interfacial drag has to be modelled explicitly. A better experimental basis of such investigations is necessary for the validation of the enhanced models.

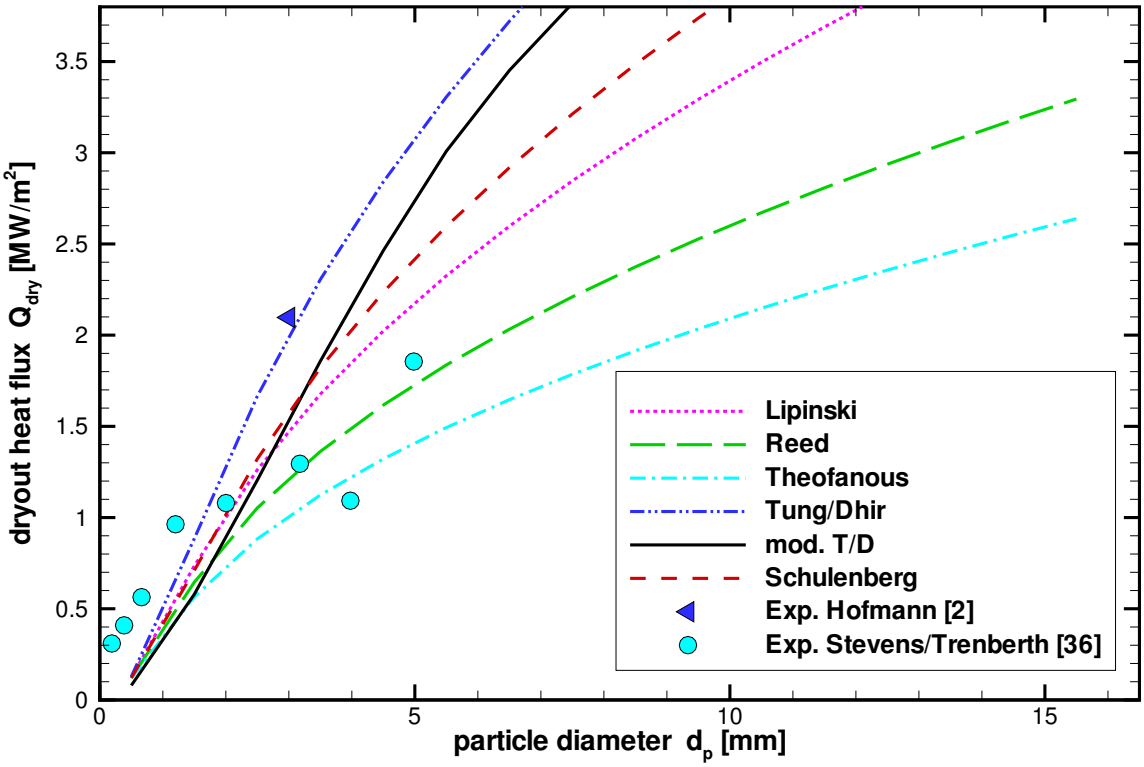

Figure 6.15: Experimental dryout heat flux in particle beds with bottom water inflow driven a hydrostatic head for different particle diameters and results from the theoretical models

6.2.2 The DEBRIS experiment

For specific investigations on the exchange terms, the friction laws, as well as the heat transfers, in boiling particulate beds, experiments were conducted in the DEBRIS facility at IKE [10]. A sketch of the experimental setup is shown in figure 6.16. A ceramic cylinder of 12.5 cm diameter and a height of 60 cm is filled with oxidised steel spheres. These steel spheres are heated inductively to represent the decay heat. The power distribution is almost homogeneous. 64 thermo-elements are distributed in the test column to detect local dryout. Along the bed height 8 pressure tubes are connected to differential pressure transducers, making it possible to measure the pressure gradient at 7 different levels. The coolant flowing into the porous region comes from a water pool above the bed. Optionally an adjusted water inflow rate from below can be injected. With this facility dryout experiment, as well as experiments on quenching of dry, hot particles are possible.

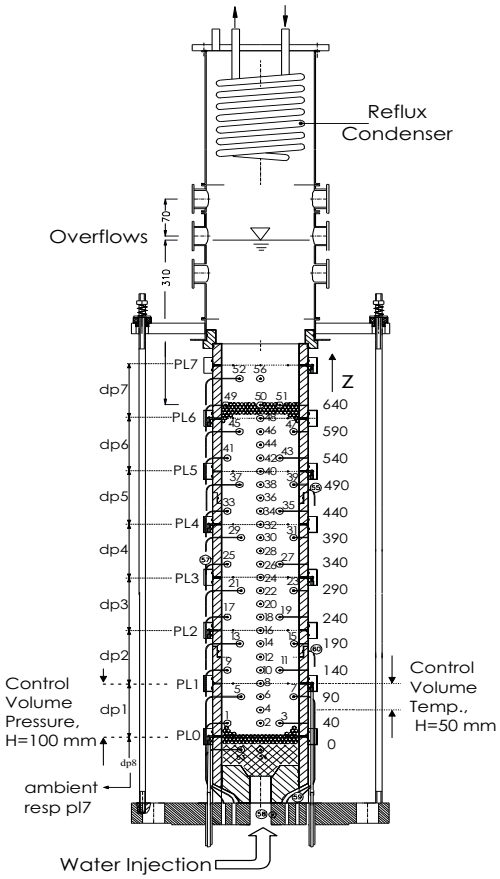

Figure 6.16: DEBRIS experimental setup

Besides the direct measurements of the dryout heat flux by increasing the bed power until the first temperature raise is detected, experiments with steady states in boiling beds can be used to deduce the friction laws. Assuming a homogeneous power distribution in the test section, the produced upflowing steam accumulates from bottom to top. So, at each level the steam flux is determined by the integrated power below. The evaporated water at each level must be replaced by water inflow. Thus, corresponding to the local steam flow, the local water flux is also given. The measured pressure gradients for these steady state conditions may be used again to compare the various friction models with the experimental data.

In the first experimental series many different measurements of pressure gradients in steady states with different bed power have been performed. The local mass fluxes between the pressure tubes are directly linked to the bed power by the condition of

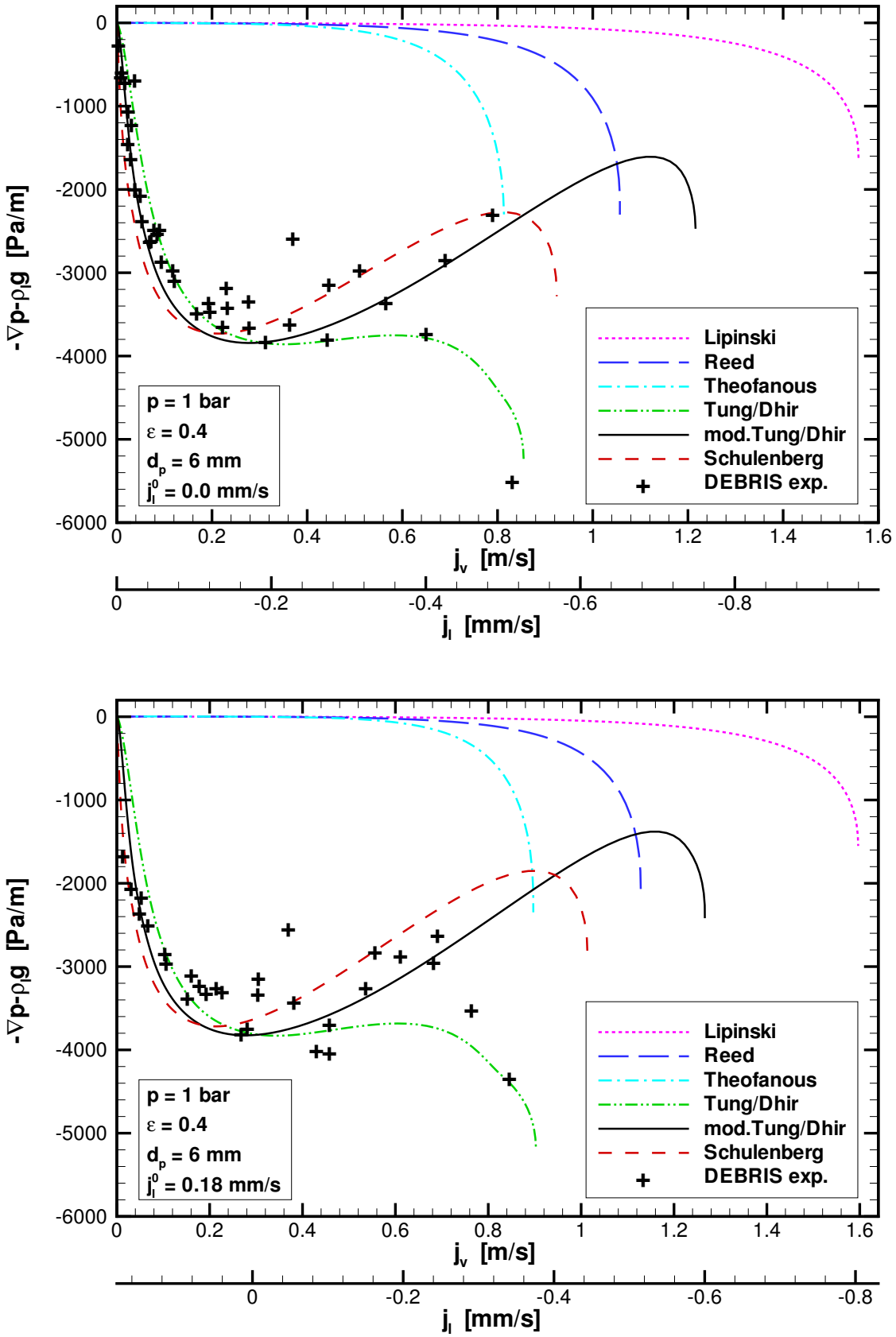

Figure 6.17: Measured and calculated pressure gradient for steady states in the DEBRIS experiments for a particle diameter of $d_p = 6\,\mathrm{mm}$ (top: without water injection from below; bottom: with water injection from below)

steady state. So, all the experimental results for the same diameter can be shown in one plot. Figure 6.17 shows the experimental data for 6 mm particles at a pressure of 1 bar. The pressure gradient, adjusted by the hydrostatic head of water, is shown versus of the superficial velocity of the steam j_v. Because of the statistical character of the measurements, an error in the order of 500 to 1000 Pa/m has to be assumed for the experimental data. Due to the steady state condition, the liquid velocity j_l is directly connected to j_v and is shown on the corresponding second x-axis in the plots. In the top figure of 6.17 the results for a pure top fed configuration are shown. Here the steam and the water fluxes are always in counter-current mode, as can be seen also at the different x-axes. With fixed water injection from the bottom, at least some parts are in co-current mode, as can be seen on the j_l-axis in the lower figure.

Additionally to the experimental data, results of calculations based on the different models for the given conditions are plotted in figure 6.17. In principle the development of the pressure gradient shows the same behaviour as in the counter-current air/water flow of figures 6.12 and 6.13. Again, it can be seen clearly that the classical models without interfacial friction can not reproduce the experimental data, and thus must be rejected. Only the enhanced models, including an explicit formulation of the interfacial drag, fit qualitatively the experimental results. Many data points have been measured for small vapour velocities. In this range the different enhanced models show no remarkable difference. For higher gas fluxes, where stronger difference between the models can be seen, it was difficult to establish steady states. So, only a few data points with a larger spread could have been measured in this range. Based on these data alone no final conclusion can jet be drawn to determine the best model.

In principle, the results with water feeding from below show the same behaviour, as can be seen in the lower plot. The pressure field obtained by the enhanced models is again showing the principle behaviour. These models fit well in both configurations, the counter-current ($j_l < 0$)) as well as the co-current flow ($j_l \geq 0$)). Another discussion from the previous chapter has to be repeated here. The limit of the steam mass flux from the models is directly connected to the dryout heat flux. Again, this can be seen in the plots. As in the isothermal case, the adaptation of the relative passability in the classical models to reproduce the measured dryout heat flux (corresponding to the limiting vapour velocity) can be seen here for a boiling bed. But as before, the pressure field in the porous structure is not reproduced.

Analogous measurements with smaller particles of $d_p = 3$ mm diameter have been performed too. The data, together with the results of the models are given in figure 6.18. The subfigure on the top again is for a pure top fed configuration, while the lower

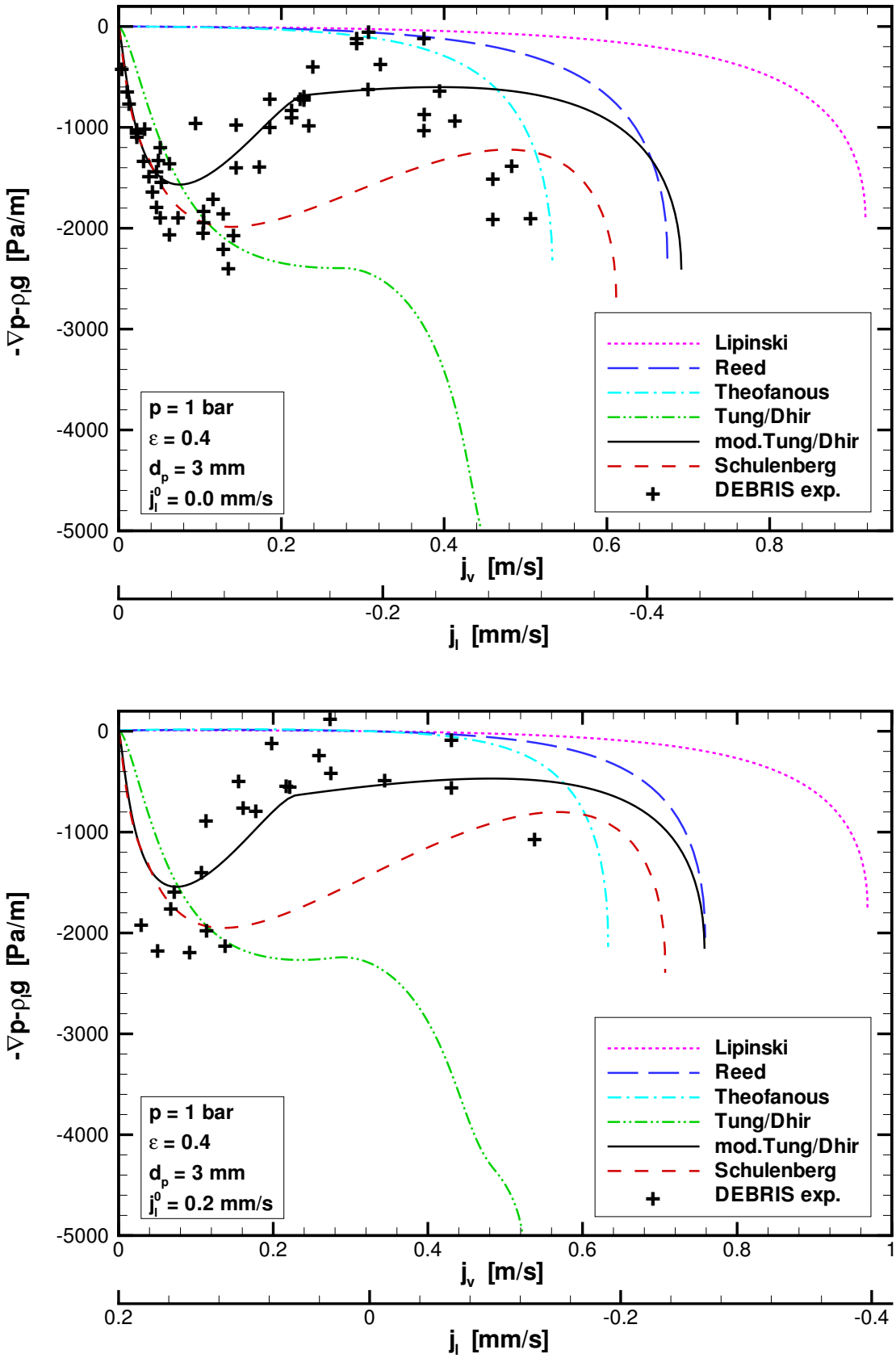

Figure 6.18: Measured and calculated pressure gradient for steady states in the DEBRIS experiments for a particle diameter of $d_p = 3\,\mathrm{mm}$ (top: without water injection from below; bottom: with water injection from below)

plot shows the results with a small water inflow of $j_l = 0.2\,\mathrm{mm/s}$ from below, yielding data points in co-current as well as in counter-current mode. For such small particles the influence of the modifications to the Tung/Dhir model proposed in chapter 5.3.1 become important, as already was seen for the isothermal experiments in the previous section. This can be seen comparing the result of the modified with the ones of the original formulation. While for the original Tung/Dhir model the pressure gradient shows a decrease with increasing vapour flux the modified formulation in principle fits the measured increase due to the reduced interfacial drag in the annular flow regime. This behaviour is also predicted by the Schulenberg model. But again, due to the spread in the experimental data, no final conclusion can be drawn which of the these two models is the better one. Therefore, in the next chapter both models will be used for calculations in reactor typical configurations.

7 Application to reactor typical configurations

7.1 Development of dryout in a pure 1D top fed configuration

All results shown so far are for steady state conditions. Such steady states only depend on the friction forces for the adjusted velocities. In the case of boiling beds the local gas flux is directly given by the accumulated steam flux, and thus by the integrated power from the bottom of the bed to the respective local height. The corresponding coolant flux is then determined by the criterion that all evaporated coolant has to be replaced. This is not valid for non-steady state conditions. Here a more sophisticated analysis, also including the mass conservation equations, is necessary. These investigations are done with the WABE-2D code, described in chapter 6.2.1. The system of mass, momentum and energy conservation equations is solved numerically in a quasi continuum approach. Additionally, a formulation for the capillary pressure is included in this code. Due to the interface of the porous bed to the coolant pool at the top, this supports the overall coolability. Based on the results of the previous chapter, only the Reed model, as the commonly used classical formulation, and the improved models of Schulenberg and Tung/Dhir, including the modifications proposed in chapter 5.3.1, will be applied in the following calculations.

The first results to be shown here will investigate the transient development to a local dryout in a simple top fed 1D configuration. A homogenous column of particulate debris with porosity $\varepsilon = 0.4$ and particle diameter $d_p = 3\,\mathrm{mm}$ at a system pressure of $p = 5\,\mathrm{bar}$ is assumed. To simplify the comparison with the in-vessel calculations shown in the next section, a bed height of $H = 1.6\,\mathrm{m}$ is chosen. By varying the specific power in the particle bed, the maximum bed power still leading to a steady state may be determined. Bed powers less than this value yield steady, cooled states, while higher ones result in a transient, leading to a local dryout. The location of the first dryout is dependent on the overpower and the bed conditions. Due to the assumed homogeneity of the power

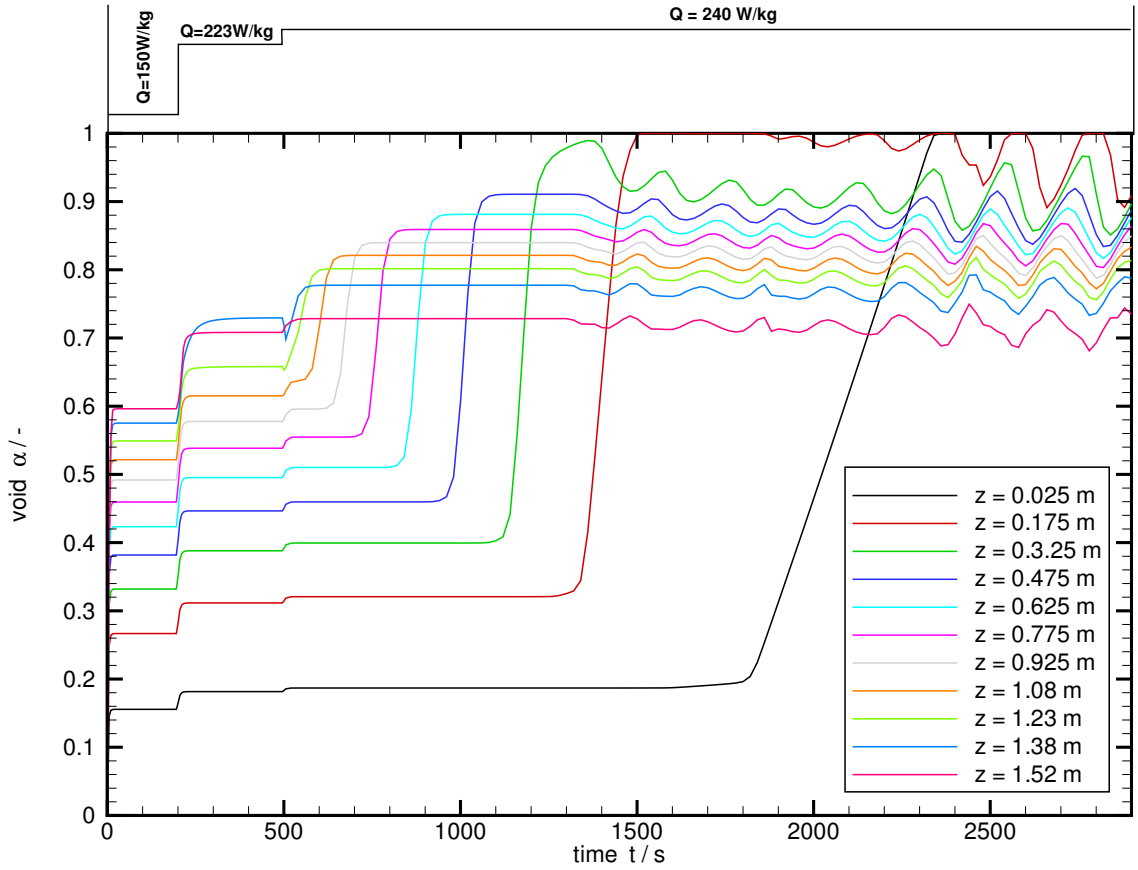

Figure 7.1: Development of the void fraction in a top fed column of 3 mm particles and height 1.6 m for a power history given on the top of the figure

distribution this maximum specific power Q in W/kg can easily be converted into the dryout heat flux by multiplying it with the density, the volume fraction of the solid material and the total bed height. For simplification, the WABE-2D calculations are performed using the Reed friction model. Initially saturated conditions are assumed.

The establishment of steady states, as well as the transient behaviour for bed powers beyond the dryout heat flux, will be shown in the first calculation. Initially, a specific power of $Q = 150\,\mathrm{W/kg}$ is chosen. As can be seen in figure 7.1, showing the time dependence of the local void at different levels in the bed, a steady distribution quickly establishes. The corresponding void profile is given in figure 7.2 by the black curve. The void increases from bottom to top. Due to capillary forces the liquid fraction slightly increases at the very top. The steam is pressed out and water sucked into this region. Therfore the profile has a maximum void, corresponding to a minimum liquid saturation, slightly below the top of the bed.

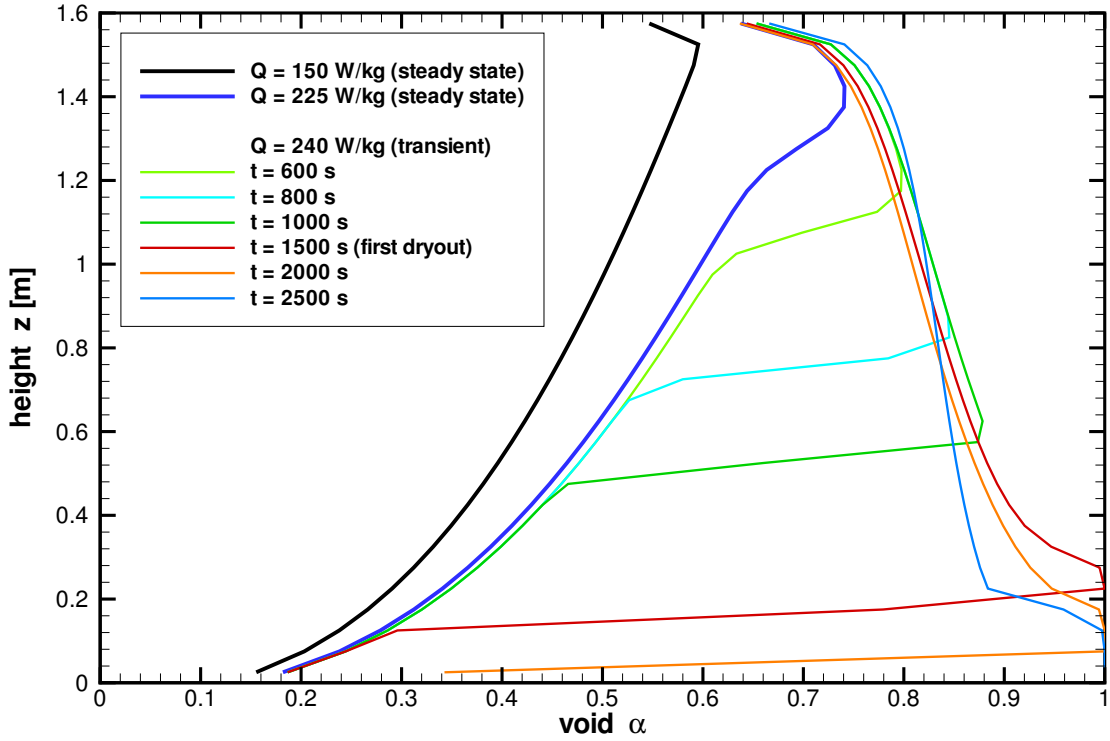

Figure 7.2: Development of the void profile for the case depicted in figure 7.1

Increasing the bed power yields an increased steam flux, and by this an increase of the void fraction. After a short transient again a steady states establishes, as long as the power is below the critical one. This is also shown in figures 7.1 and 7.2, where the specific power is raised to $Q = 225\,\mathrm{W/kg}$, a value slightly below the critical one. Here still a steady state can establish, but the maximum void of the counter-current flooding limit is nearly reached in the top region. Additionally the void profile in figure 7.2 shows a broader nose region near the top. For a further increase of power, no more steady states are possible and a transient behaviour starts.

The transient development to local dryout after an increase of the specific power beyond the critical value is also shown in figure 7.1 and in the corresponding void profiles in figure 7.2. Here the specific power was raised to a value about 8 % above the critical conditions. Due to the increased power the steam flux to the top is increased too. This also increases the void, which now hinders the coolant inflow, yielding an undersupply of coolant water. As can be seen in the figures, the local void first increases in upper regions, while it remains almost stable in the lower bed parts. This is due to an internal flow of coolant water in the bed itself. So, the lower bound of the coolant undersupply migrates downwards, superimposed by a decrease of the minimum liquid fraction until

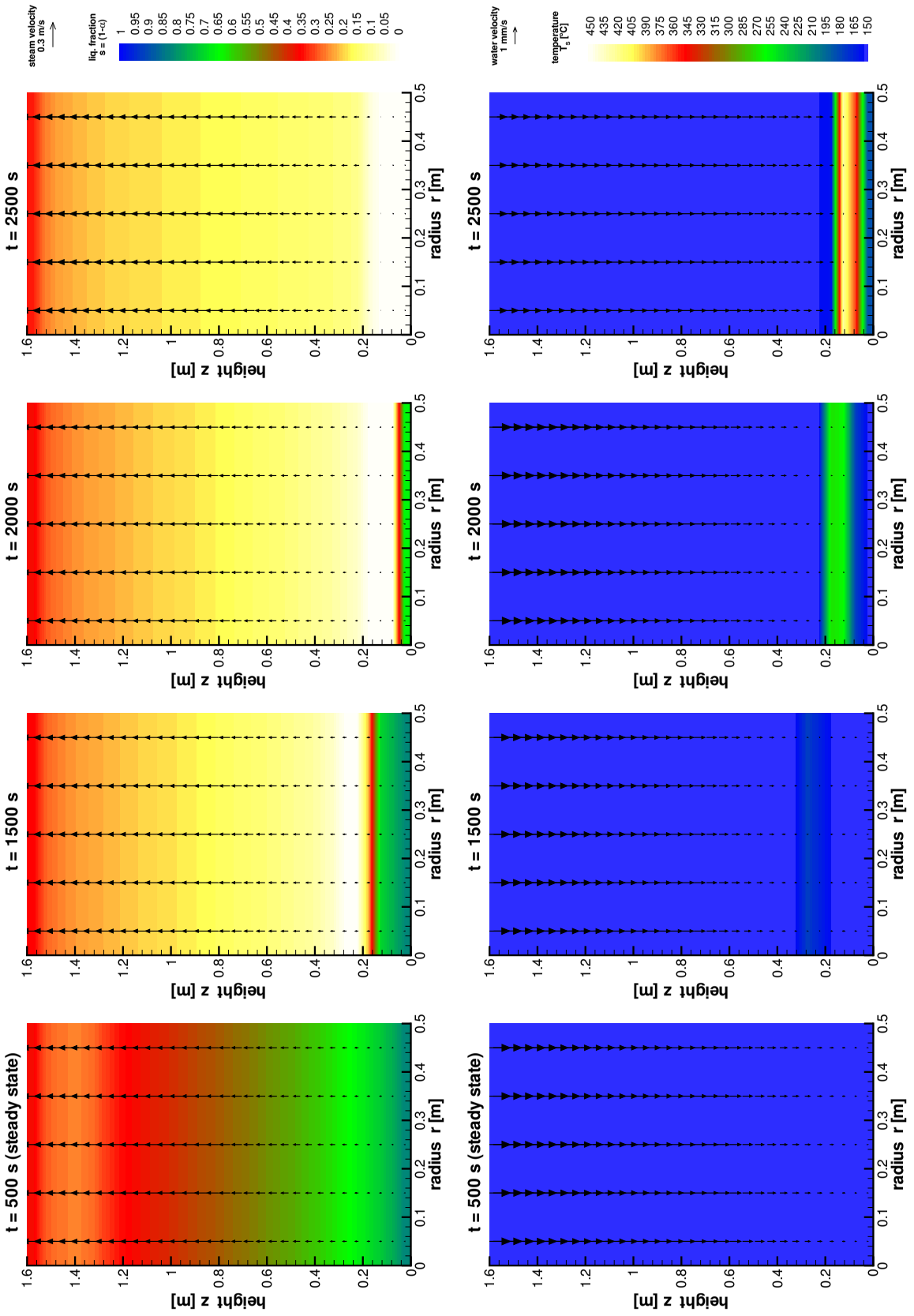

Figure 7.3: Development of the liquid volume fraction $s = (1-\alpha)$ and superficial velocity of the steam (upper row), as well as the particle temperature and water velocity (lower row) for the case depicted in figure 7.1

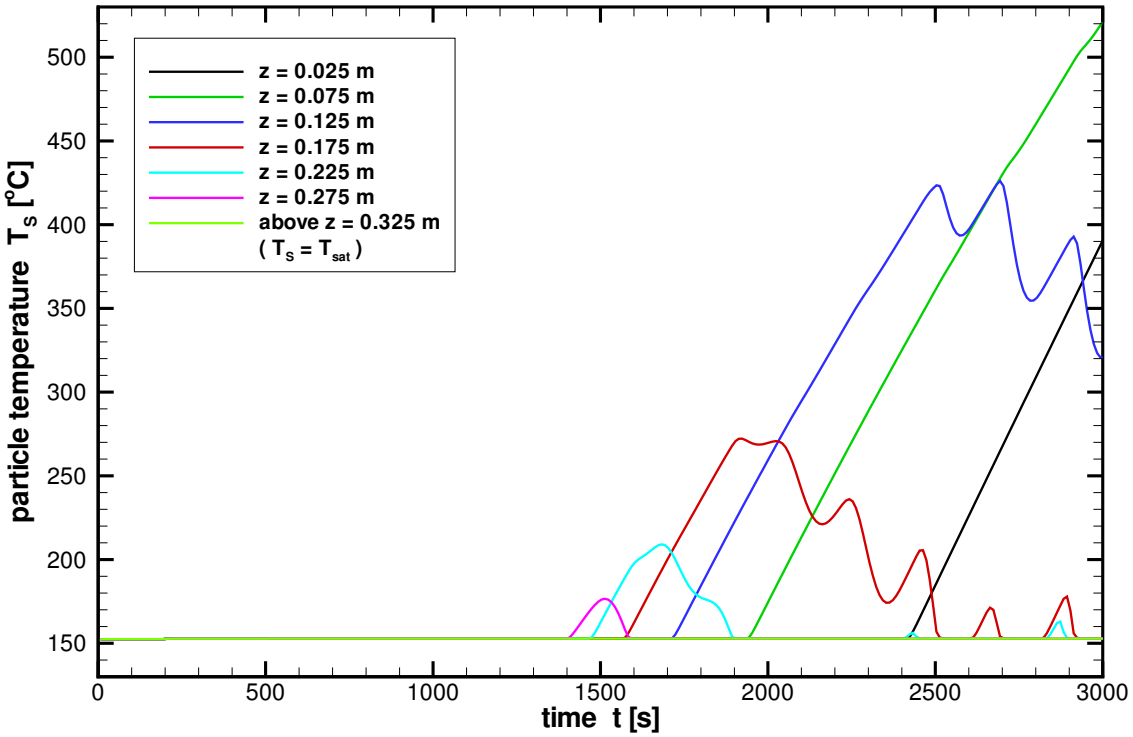

Figure 7.4: Development of the particle temperature in the lower calculation cells for the case depicted in figure 7.1

local dryout. This can clearly be seen in the void profile development in figure 7.2. The location of this first dryout depends on the overpower. The more this power is above the critical one, the higher the location of first dryout will be.

As can also be seen in the void profiles of figure 7.2, the dryout location moves towards the bottom. This is easy to understand, as no more water from the top reaches the region below the dryout. The locally existing water is just evaporated, superimposed by a small downwards water flux inside this region. So, the lower bound of the dryzone moves downwards. On the other hand, the upper bound moves downwards too. Since in the dry zone no more steam is produced, the steam flux to the top is reduced, yielding a slightly enhanced water inflow. The water downflow reaches down to the dryzone, where all of it is consumed during the path. This process continues, until the dry zone has reached the bottom of the bed. A steady liquid distribution with a dry region at the bottom establishes. The upper part of the particle bed is cooled by water inflow from above. On its way down the coolant is evaporated and reaches just until the upper bound of the dryzone. This development can clearly be seen in the contour plots given in figure 7.3. The liquid fraction $s = (1-\alpha)$ as well as the steam velocity j_v are given in the upper row for different times. The local dryout is displayed by the

white colour. Even easier this can be seen in the temperature distributions, given in the lower row of figure 7.3 together with the velocity of the liquid coolant.

Besides the downward motion the absolute overheating of the dryzone increases with time as can also be seen in figure 7.4. The development of the particle temperature is shown for lower bed regions. Before the first dryout occurs the particles are almost at saturation temperature. The increase in temperature at the level $z = 0.275\,\mathrm{m}$ indicates the first dryout. Subsequently, lower cells also get dry, while, due to the now missing steam production in the dryzone, the regions of the first dryout are quenched again. After reaching the bottom of the bed, the dryout location will be stable. As there is now no more heat sink, the temperature will raise unlimited here, as can be seen for the lowest cells at $z = 2.5\,\mathrm{cm}$ and $z = 7.5\,\mathrm{cm}$ in figure 7.4. The fluctuations of the void after the first dryout in figure 7.1, even in upper bed regions, are a direct consequence of this development. The dried out region heats up a bit and is quenched when water is reaching the position again. This yields a stronger evaporation, and by this a small pressure increase, hindering further water to reach this region. The produced steam arises through the bed, yielding temporally higher void fractions in upper parts. This procedure repeats during the movement of the dryzone. Varying the discretisation in the WABE-2D calculations with half and quarter cell sizes shows no significant differences in the results. Especially the calculated frequence of the fluctuations is the same.

The above used saturation conditions, in temperature, as well as in water fraction, as starting conditions may not be assumed for particulate debris during severe accidents in a nuclear power plant. During the fragmentation process melt droplets are created first. They are quenched while falling into the water, and solidified to particular debris. After they have settled the particles are still hot, with a steam film around them. So, for more realistic initial conditions superheated particles have to be assumed. The heat transfer to the cooling water, yielding the evaporation, is now given by film-boiling correlations. In the WABE-2D code a representation of the boiling curve including a pool- as well as a film boiling regime is included. So, such configurations can be calculated with the code too.

An exemplary result of such a calculation is given in figures 7.5 and 7.6. The conditions chosen are the same as for figure 7.1, but this time starting with a dry particle bed at a particle temperature of $1000\,^{o}\mathrm{C}$. As before, a constant specific power of $Q = 150\,\mathrm{W/kg}$ is used. A race between further temperature increase in the dry regions due to the decay heat and quenching due to coolant influx establishes. If the quench front has reached every location in the bed before remelting of the particles, the configuration

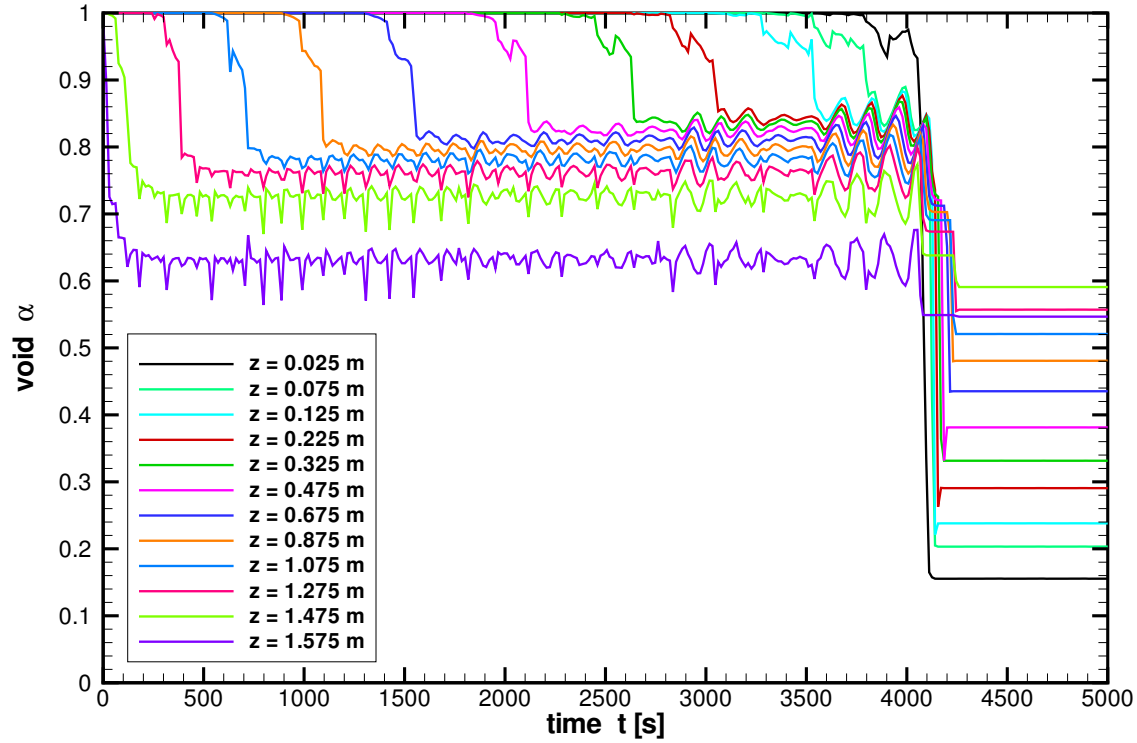

Figure 7.5: Development of the void at different levels during quenching of an overheated dry particle bed (T_s^0=1000 ^{o}C)

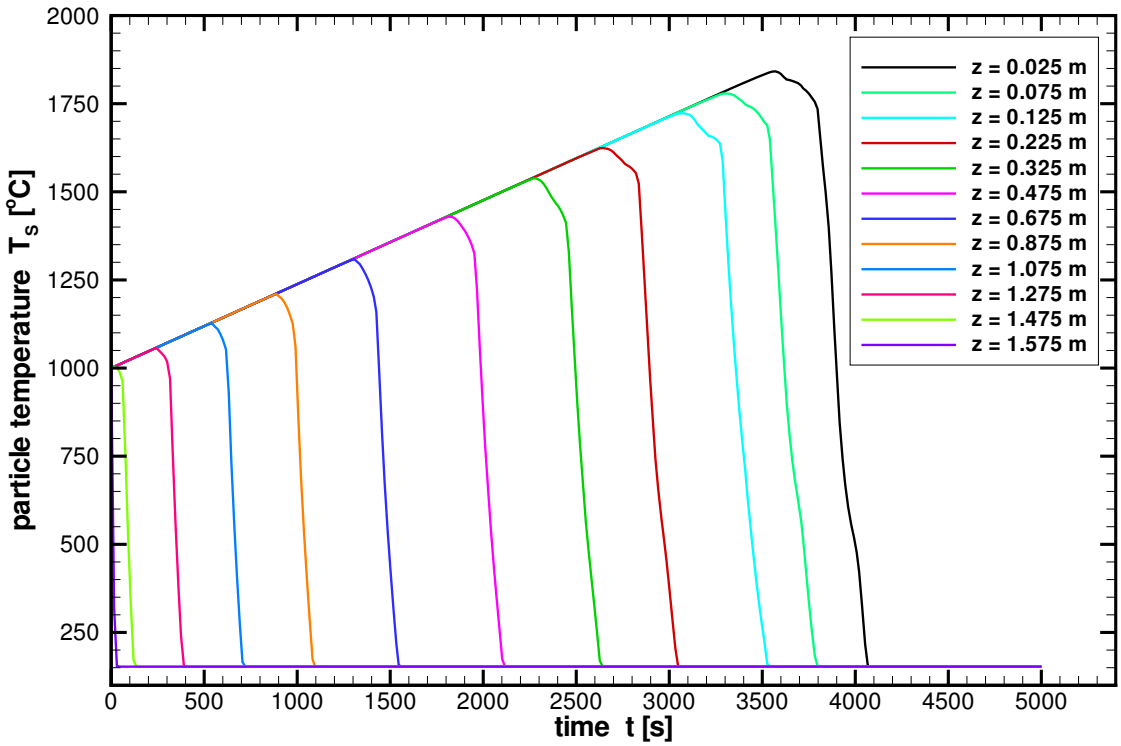

Figure 7.6: Development of the temperature at different levels during quenching of an overheated dry particle bed (T_s^0=1000 ^{o}C)

is coolable. In the calculation such a steady state is reached for the conditions given here after about 4200 s. It has to be noted, that the resulting state is the same as the one calculated when starting from saturation conditions in figure 7.1. So, for the long term coolability it is in general necessary to include such overheated starting conditions, to assure that quenching occurs before remelting. On the other hand, to compare the cooling potential of different configurations, the maximum power that can be discharged, corresponding to the dryout heat flux, can also be compared when starting from saturated conditions.

7.2 In-Vessel particulate debris

Realistic configurations of particulate debris, that are to be expected during severe accidents in a nuclear power plant, are not purely one dimensional, as stated above. Due to the multidimensionality the flow conditions are enhanced. Especially coolant flow paths with less resistance to lower bed regions increase the overall coolability of particulate corium in a water pool. This was already seen in chapter 6.2.1 for a one dimensional configuration with bottom inflow driven by hydrostatic pressure. For configurations where the coolability has to be established passively in a water environment, as in the reactor application, facilitated coolant flow paths define a similar effect.

Corresponding to the 1D configuration of the last chapter, now a particulate debris bed is assumed in the lower head of a reactor pressure vessel. As before, a maximum bed height of $H = 1.6\,\mathrm{m}$ is set at the centre. The configuration, as well as the discretisation of the calculations, is given in figure 7.7. As the calculation domain in WABE-2D is fixed to a simple structured grid, the parts outside the particle bed have to be modelled. First of all, the boundary of the vessel has to be mapped to the discretisation grid. To avoid any kind of fluid flow in the outer region a very small porosity of $\varepsilon = 10^{-10}$

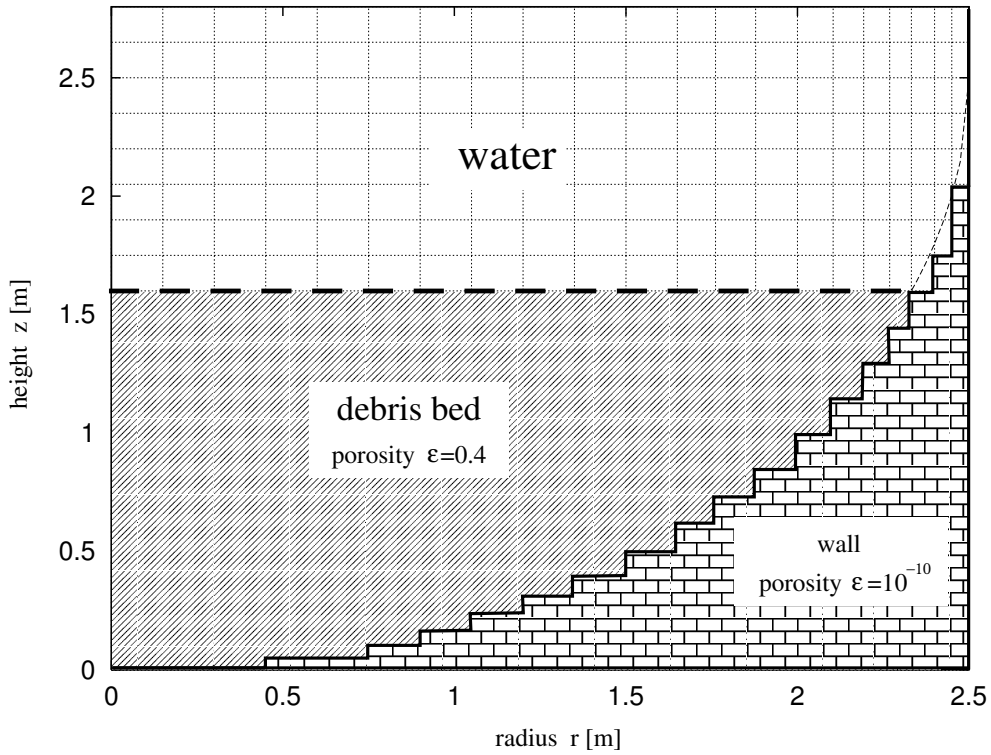

Figure 7.7: Configuration of the particulate debris in the lower head (case1)

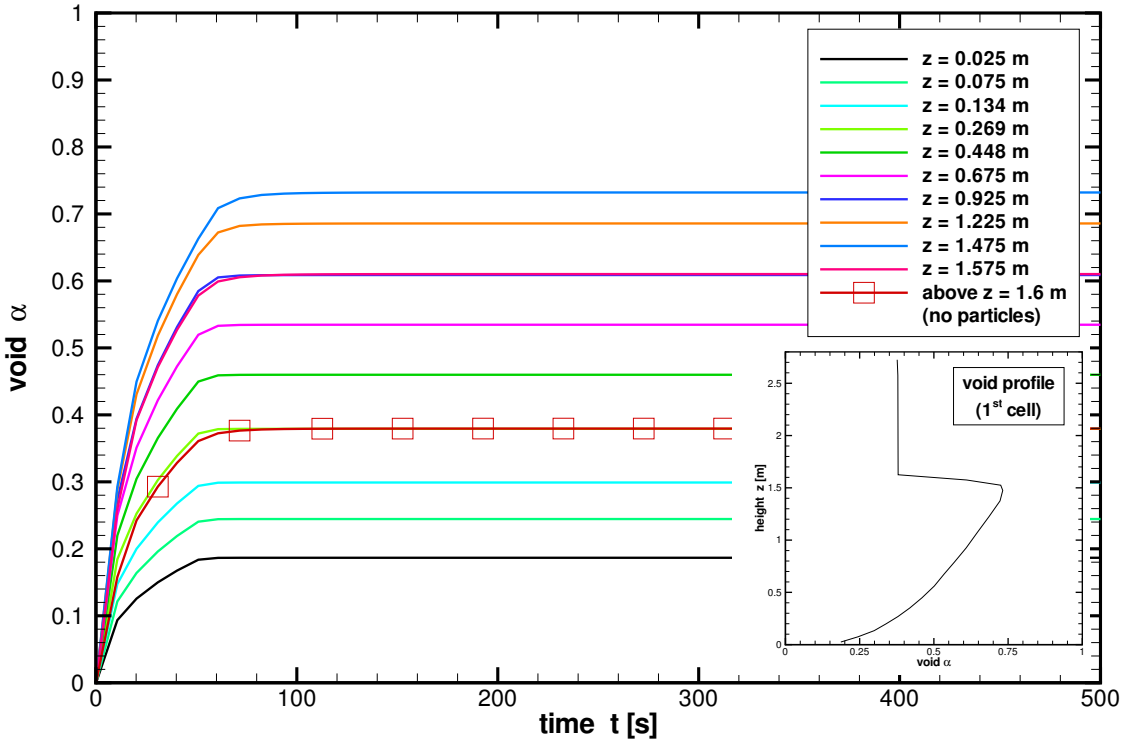

Figure 7.8: Development of the local void fraction in the inner cell

is assumed here. Additionally, the local power is set to zero. Above the particulate debris bed a water area with no local heat sources is assumed. As the friction terms implemented in WABE-2D do not include the inertial and the stress terms of the Navier-Stokes equations, some porosity and particle diameter has to be assumed here to represent a resistance against the motion. Variations have shown, that a porosity of about $\varepsilon \approx 0.8$ in this region is sufficient. Higher values showed no more influence on the calculation results.

Except for the geometry the same debris parameters as in the 1D case of figure 7.1 are used in the calculation. Again, a porosity of $\varepsilon = 0.4$, a particle diameter of $d_p = 3\,\mathrm{mm}$ and a system pressure of $p = 5\,\mathrm{bar}$ is assumed. The particulate debris fills the hemispherical lower plenum of radius 2.5 m up to a maximum height of $H = 1.6\,\mathrm{m}$. This corresponds to the 1D configuration of the previous chapter. The total corium mass in this geometry is $M = 80\,\mathrm{t}$. As before, a specific power of $Q = 240\,\mathrm{W/kg}$ (corresponding to a volumetric power of $1.15\,\mathrm{MW/m^3}$) is applied. This value yields a dryout in a 1D configuration. As can be seen in figure 7.8, in the two dimensional configuration this power can still be discharged, and a steady state establishes. A maximum void of $\alpha_{max} = 0.72$ is reached in the upper centre of the particle bed. The reason for this enhanced coolability can be seen in the contour plots in figure 7.9. Due to the lower bed height in the

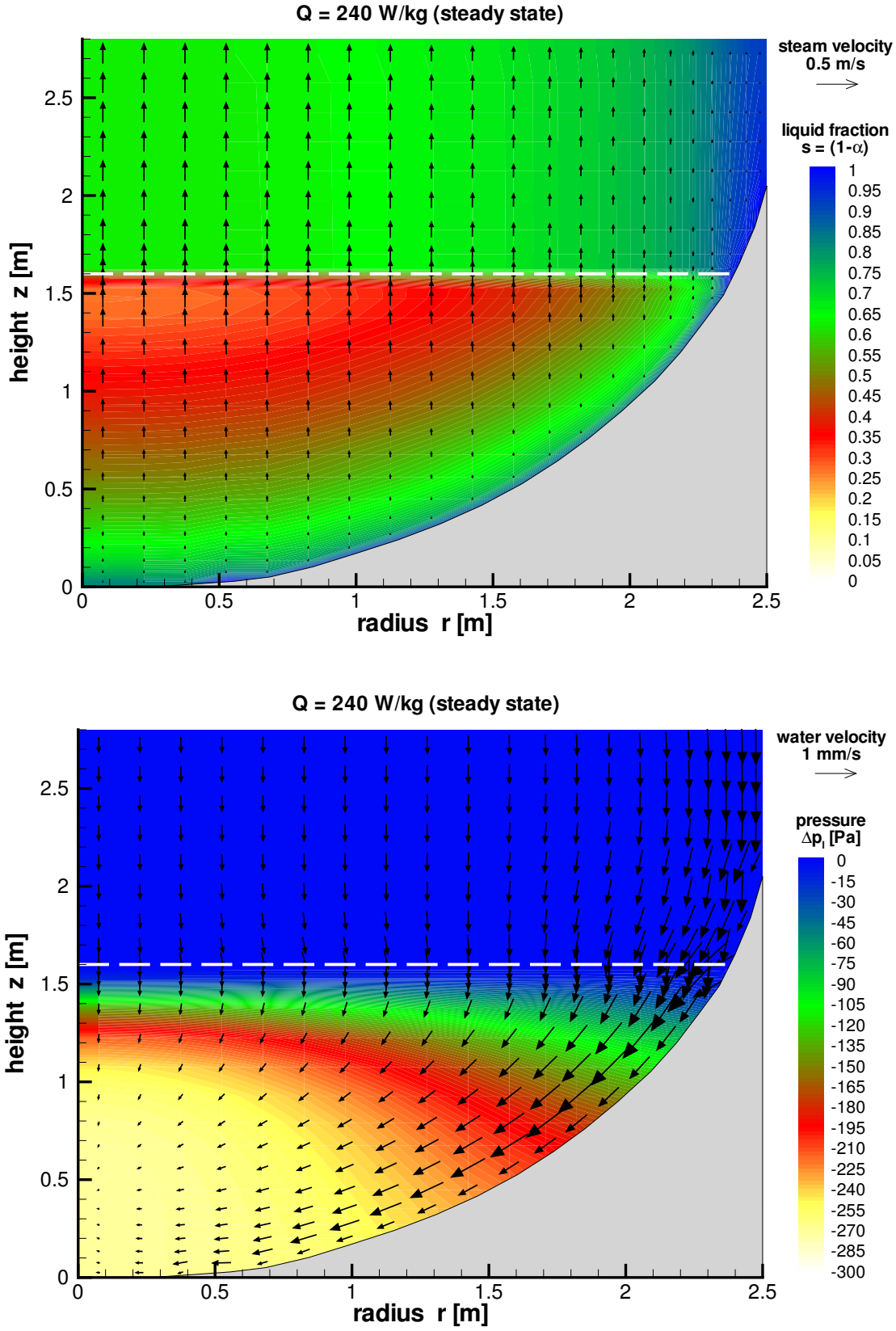

Figure 7.9: Distribution of liquid fraction and steam velocity (top) as well as local pressure, reduced by the hydrostatic head, and liquid velocity (bottom)

outer parts of the debris bed, here water infiltration is easier. Driven by gravity, or correspondingly by the established pressure distribution, the coolant flows along the vessel wall to lower bed regions, as can be seen in figure 7.9 (b). So, the evaporated liquid in main parts of the bed is replaced by lateral water ingression over regions of small void, and corresponding high water fraction. Due to the higher liquid saturation the particle-liquid drag is reduced along this path.

The pressure field shown in the figure is the calculated local pressure, reduced by the local hydrostatic head of a water column. It is obvious from equation 5.5, that the gradient of this field is the driving force for the water flow when no interfacial friction is considered. The lowest pressure is reached in the centre near the bottom of the bed. So, the water is pulled towards this region. As can be seen in the figure, the lower parts of the bed are supplied by lateral water influx driven by this pressure field. This coolant flow increases the overall coolability. A major fraction of the total inflowing water now is not in counter-current mode against the highest steam flow. But, in the upper parts, the evaporated liquid is still replaced by vertical inflow from above. This holds true especially for the region of smallest void in the top centre of the bed. From the outer parts the excessive water flows to lower central regions and by this supports the overall coolability.

Local dryout, and thus the limit for overall coolability, will be reached for increased bed power. For the in-vessel configuration given in figure 7.7 this limit is reached - based on the Reed friction model - at a specific power of $Q = 301\,\mathrm{W/kg}$. The resulting distributions of the liquid fraction, the reduced pressure and the velocities for this calculation are plotted in figure 7.10. As for the steady state before, the location of the minimum liquid fraction is almost in the centre at the top of the debris part. In contrast to the 1D configuration, discussed in the previous section, here a local liquid fraction of almost zero may be achieved for still steady states. As discussed before, in the pure top fed 1D case, a minimum local saturation of about $s_{min} \approx 0.26$, depending on the model formulation, is necessary to assure the water inflow to lower bed regions in counter-current mode. In the two dimensional case this is no more the limiting factor, because lower bed regions are laterally supplied by cooling liquid. This effect can also be seen clearly in the distribution of the reduced pressure and the liquid velocity in figure 7.10 (b). The lowest local pressure now is at the location of the smallest liquid saturation, almost at the top. Due to the pressure gradient in the centre the water coming from the side is even dragged up to this location, yielding a co-current flow here. This is in some kind similar to the bottom fed configurations discussed in chapter 6.2.1. Only the very top of the central region is directly supplied from above in counter-current mode.

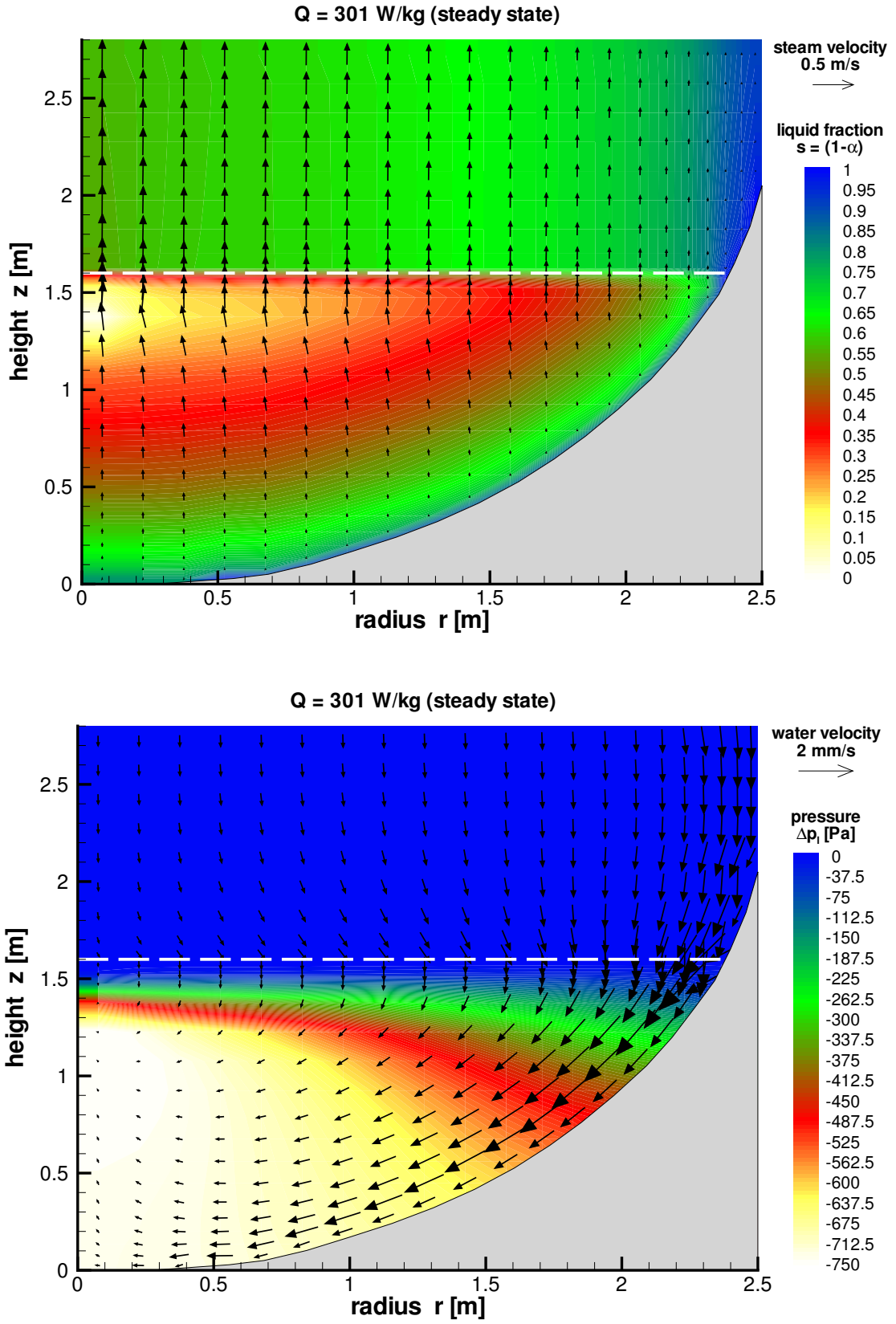

Figure 7.10: Distribution of liquid fraction and steam velocity (top) as well as local pressure, reduced by the hydrostatic head, and liquid velocity (bottom) for a power slightly below dryout (Reed model)

A further small increase of the bed power will yield a local dryout exactly at the point of the smallest liquid saturation in the central top region. Now, no more all the evaporated water can be replaced by the inflow into the bed. The flow paths of the liquid are the same as before in the steady state, but now the inflowing water is consumed before reaching the dry spot. The size of the dry zone depends on the overpower, but its location will be stable, besides some extension due to heat conduction from the hot spot to the surrounding regions.

In general it is not clear, how to define the dryout heat flux in such multidimensional configurations. As can be seen in figure 7.10 (a) the produced steam rises straight to the top, driven by the buoyancy force, just as in the one dimensional case. In contrast now the evaporated coolant is not just replaced by a counter flow downwards. So, the counter-current flooding limit, determining the dryout heat flux in 1D configurations, is no more limiting. But, based on the steam flux, the heat flux to the top may be defined for a column where the almost dry spot occurs. This is at the centre, where the bed is highest. The dryout heat flux can now be defined by the maximum heat flux from this column, before reaching a local dryout. It is calculated by multiplying the volumetric power by the bed local height. By this definition it is clear, that the dryout heat flux now has no more a comparable value for different configurations, because it strongly depends on the bed geometry. For example, supposing a particle bed surrounded by a cylindrical grid in a water environment, the dryout heat flux will decrease for increasing cylinder diameter. As a conclusion of the non-generality of the dryout heat flux, multidimensional calculations have to be performed for the specific geometry to investigate the overall coolability. For this purpose, verified codes based on realistic friction laws are necessary.

Nevertheless, using the definition of the dryout heat flux based on the maximum bed height, comparisons to a pure 1D case and to cases with the same geometrical configuration may be done. Using the bed parameters for a 1D configuration of height $H = 1.6\,\mathrm{m}$ yields a maximum specific power of $Q^{1D}_{max} = 228\,\mathrm{W/kg}$, corresponding to a dryout heat flux of $q^{1D}_{dry} = 1.72\,\mathrm{MW/m^2}$. This value has to be compared with the two dimensional result of $Q_{max} = 301\,\mathrm{W/kg}$ (volumetric power $1.44\,\mathrm{MW/m^3}$) maximum hating power, or equivalently $q_{dry} = 2.3\,\mathrm{MW/m^2}$ dryout heat flux. So, due to the multidimensionality an increase in coolability of about 32 % can be observed. As a consequence, the coolability potential of particulate corium during a severe accident in a nuclear power plants will be in general underestimated when based one dimensional considerations, as usually done.

Similar calculations have also been executed for the enhanced friction models of Schulenberg and Tung/Dhir, including the modifications proposed in chapter 5.3.1. The

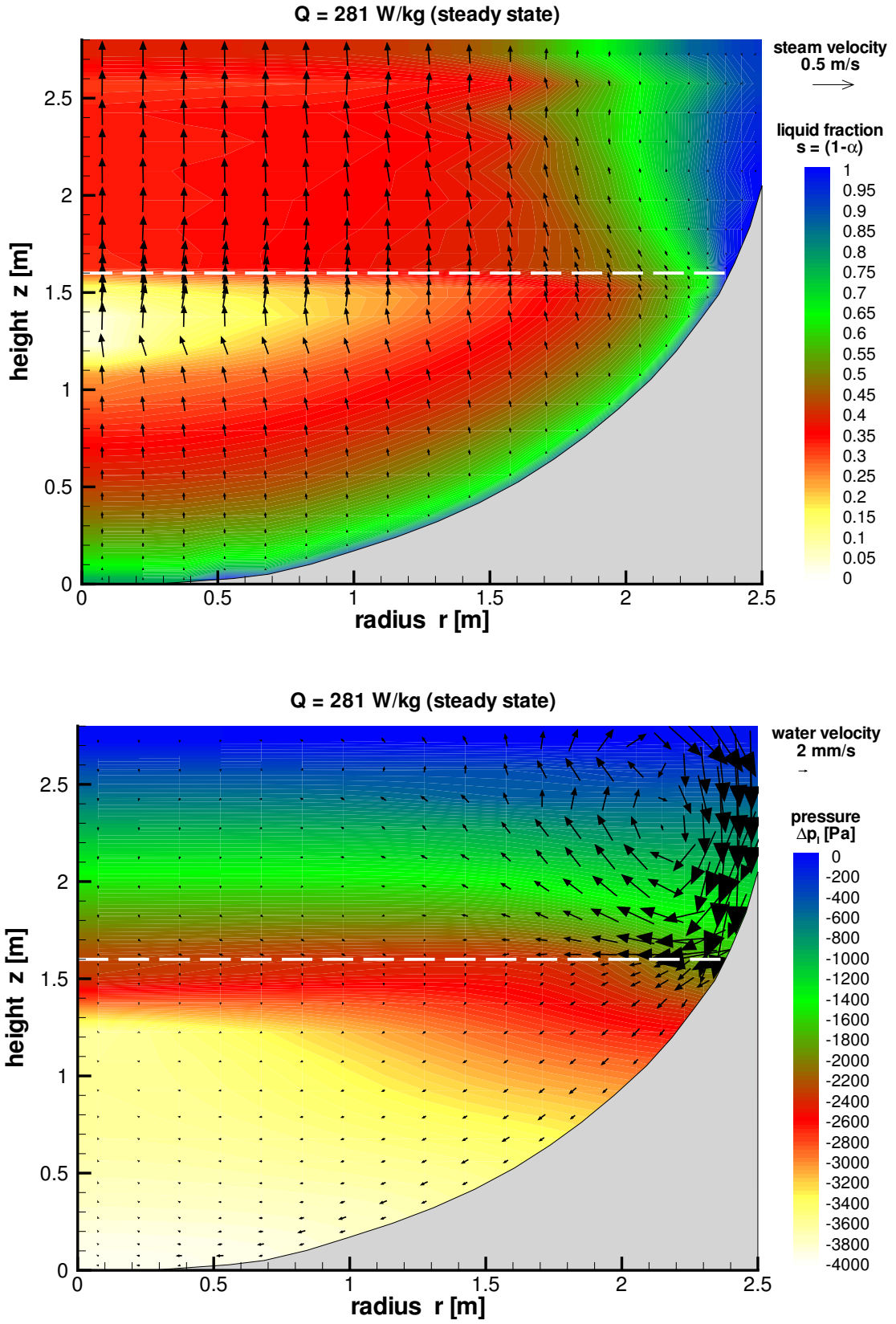

Figure 7.11: Distribution of liquid fraction and steam velocity (top) as well as local pressure, reduced by the hydrostatic head, and liquid velocity (bottom) for a power slightly dryout (Schulenberg model)

distributions for a steady state slightly below the dryout point can be seen in figure 7.11 for the Schulenberg model. The first point to be discussed, is the smaller maximum specific power of $Q_{max} = 281\,\mathrm{W/kg}$ ($q_{dry} = 2.15\,\mathrm{MW/m^2}$) compared to the result of the Reed calculation. This difference can already be seen in the 1D configuration, where the Schulenberg model yields a dryout heat flux of $q^{1D}_{dry} = 1.56\,\mathrm{MW/m^2}$ ($Q^{1D}_{max} = 204\,\mathrm{W/kg}$). Looking at the friction laws given in chapter 5, this difference becomes clear. Schulenberg uses the same exponents in the particle-liquid drag as Reed, and increased the particle-gas drag by increasing the exponent in the relative passability of the gas. Additionally, Schulenberg included the interfacial friction, acting against coolant inflow from above. This explains the worse coolability based on Schulenberg's model. Nevertheless, comparing the 1D and 2D results yields a slightly higher gain in cooling potential of 38 % for the Schulenberg model.

Looking at the water velocities in figure 7.11 (b) it can be seen, that the movement in the water area above the bed becomes dominating. As the interfacial drag of the upflowing steam on the water is largest above the centre, a kind of water loop establishes in the pool area. The flow velocities here are not interesting, but dominate the distribution. So they will be ignored in further plots, to resolve the velocities inside the debris bed. An updated plot is given in figure 7.12.

The interfacial friction hinders the water ingression from the pool, especially in centre regions of the geometry, where the steam flux is highest. Comparing the water velocities of the Reed results (figure 7.10) with the ones for the Schulenberg model (figure 7.12) shows that clearly. In the Schulenberg case a more pronounced lateral water flow can be observed. This can also be seen in the pressure field. Much smaller reduced pressures ($\approx$-4000 Pa) are reached inside the bed, leading to higher pressure gradients driving the water flow. So, the increased friction for the flow is partly compensated by the higher pressure gradients in the bed. This was already seen in chapter 6.2.2 for 1D configurations. Additionally, the lowest pressure now is at the bottom centre of the debris bed. But, above this location, the water flows against the pressure gradient. This is due to the drag force of the upflowing steam on the liquid. The direct inflow from above is reduced by the interfacial drag at the centre top of the bed. In general it can be concluded, that the flow paths of both models are comparable with a stronger tendency to lateral flow for the Schulenberg model. This leads to a comparable gain in coolability. A summary of the results for the different models is given in table 7.1. Besides the maximum specific power Q_{max} the corresponding dryout heat flux q_{dry} and the total discharged power for the whole bed configuration is given.

The corresponding results for the modified Tung/Dhir model are show in figure 7.13. In general, all the points discussed before for the Schulenberg model hold here too.

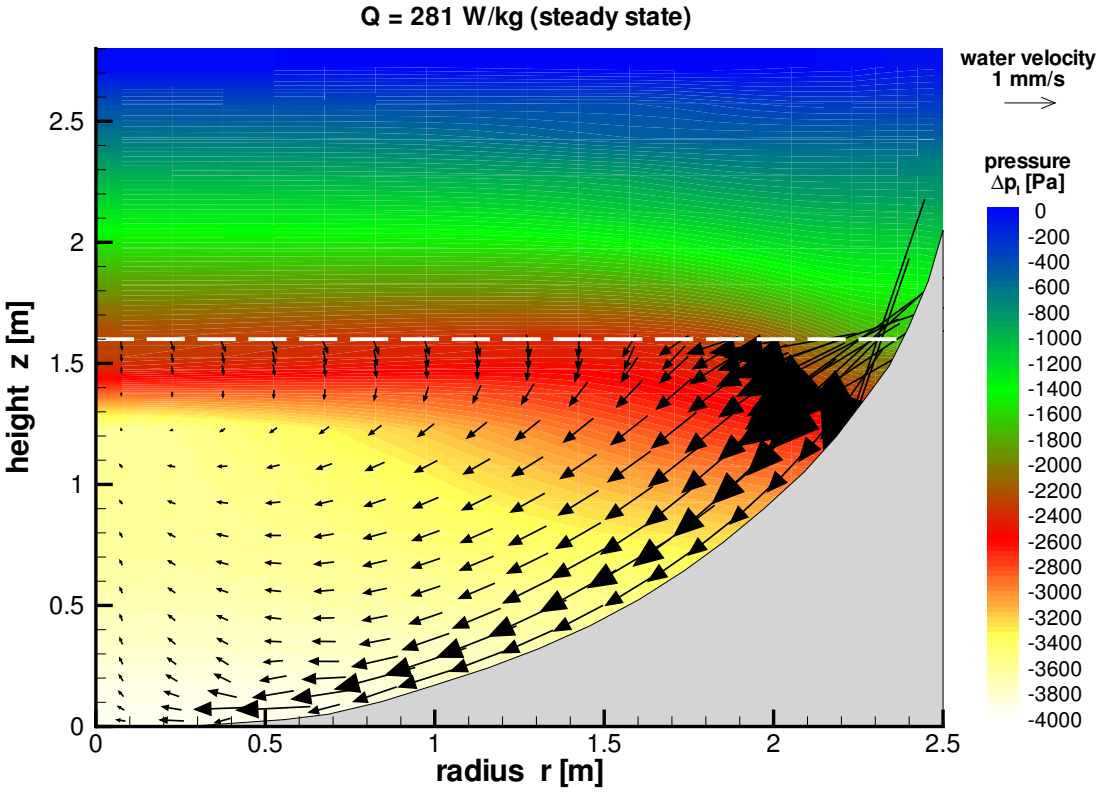

Figure 7.12: Distribution of local pressure, reduced by the hydrostatic head, and liquid velocity for a power slightly below dryout (Schulenberg model). The velocities outside the particulate debris are ignored

Due to the smaller particle fluid drags, better coolability is achieved for this model compared to the Reed formulation, in the 1D as well as in the 2D configuration. Comparing the 1D and the 2D results, the modified Tung/Dhir formulation only yields a coolability gain of about 26 %, but this is strongly affected by the large 1D value with a maximum specific power of $Q^{1D}_{max} = 252\,\mathrm{W/kg}$. Looking at the formulation of the friction terms, this can be explained. In general the particle fluid drag is smaller in the Tung/Dhir formulation than in the Reed model. The interfacial drag is reduced due to the modifications proposed in chapter 5.3.1 for the 3 mm particles of the bed. But outside in the pool, described by larger particles and porosity, this friction is dominant and hinders the water ingression from above into central regions. On the other hand, due to the smaller friction compared with the Schulenberg model, the pressure gradient in the bed is not so pronounced, yielding a weakened lateral water flow. Summarising these results, a strong increase in coolability was observed due to the lateral coolant flow in the two dimensional configuration, compared to a 1D consideration. This gain in the overall coolability is mainly independent of the friction model. In the enhanced

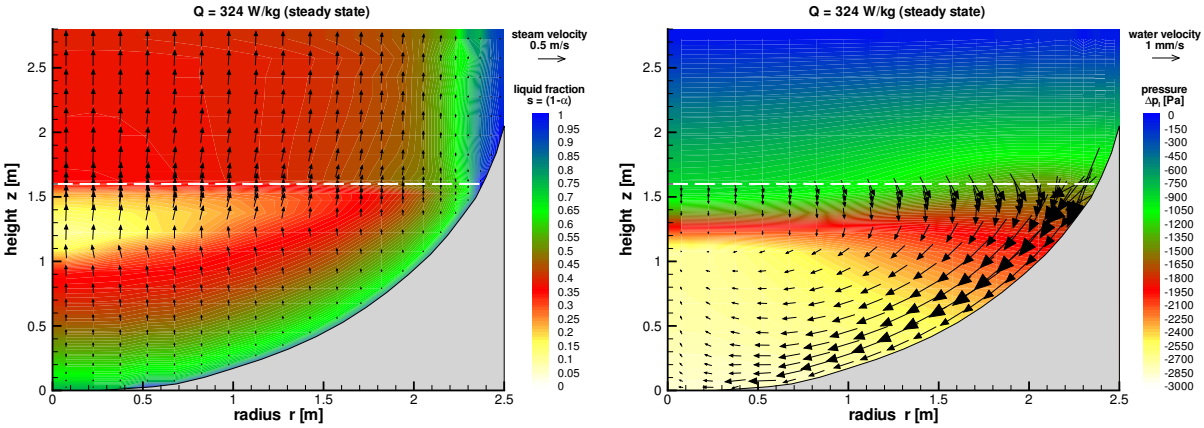

Figure 7.13: Distribution of liquid fraction and steam velocity (top) as well as local pressure, reduced by the hydrostatic head, and liquid velocity (bottom) for a power slightly below dryout (modified Tung/Dhir model)

models, including an explicit formulation for the interfacial drag, the increased friction is compensated by increased pressure gradients that establish inside the porous bed.

A second case with even stronger 2D characteristics will be regarded in the following. Now the particle bed has no flat upper surface, but is assumed to have a mound shape represented by a truncated cone. This may also be expected during an accident scenario due to the settlement of the fragmented melt jet as particles in the water environment. The configuration of case 2 is shown in figure 7.14. With a total corium mass of $M = 86\,\mathrm{t}$ this case is comparable to the case 1 shown before. Stronger 2D effects can now be expected, increasing the overall coolability. But, the main counteracting effect is due to the increased maximum bed height of $H = 2.8\,\mathrm{m}$ in the centre. The one dimensional dryout heat flux is per definition independent of the bed height, but corresponds to smaller bed powers for higher beds. Thus the maximum allowed power values in this configuration are significantly smaller than before in the flat configuration. The resulting maximum power discharged for the different models in comparison with the corresponding results for a pure 1D configuration are again given in table 7.1. Results of calculations based on the different models are given in figure 7.15.

As in the flat configuration, a direct upflow of the steam and an almost dry spot in the top of the particle bed can be seen. The evaporated water below this spot is replaced by a lateral water inflow over the debris boundary. For the classical Reed model this inflow is almost homogeneous over the whole surface. The models with interfacial frictions show a different behaviour. Here the main coolant inflow is over the lower edge of the debris part. In higher parts of the shell, the drag of the upflowing

steam hinders the water ingression. Comparing the results of the different models, again the stronger pressure gradients for the enhanced models have to be mentioned. This stronger pressure gradient is necessary to yield the enlarged water inflow along the vessel boundary. As can be seen in table 7.1, an even increased gain in overall coolability is obtained for the Reed and the Schulenberg model. Both yield a more than 40 % increased coolability, compared to a one dimensional configuration. Only the modified Tung/Dhir model yields a smaller gain of 25 %, but as in the flat case, this value is referenced to a higher 1D coolability value.

In general it can be concluded from the calculations in this subsection, that the main effect increasing the overall coolability of the in-vessel particle debris examined here is due to the multidimensional nature of the configurations. Only a minor influence of the global behaviour on the interfacial drag was observed. Increased drag forces in the enhanced models are partly compensated by increased pressure gradients. As a second result it has to be noticed, that the increased bed height in the mound shaped configuration yields less overall coolability. This is the same in one dimensional considerations, but due to the multidimensional configuration the limiting value is reached at a higher power level.

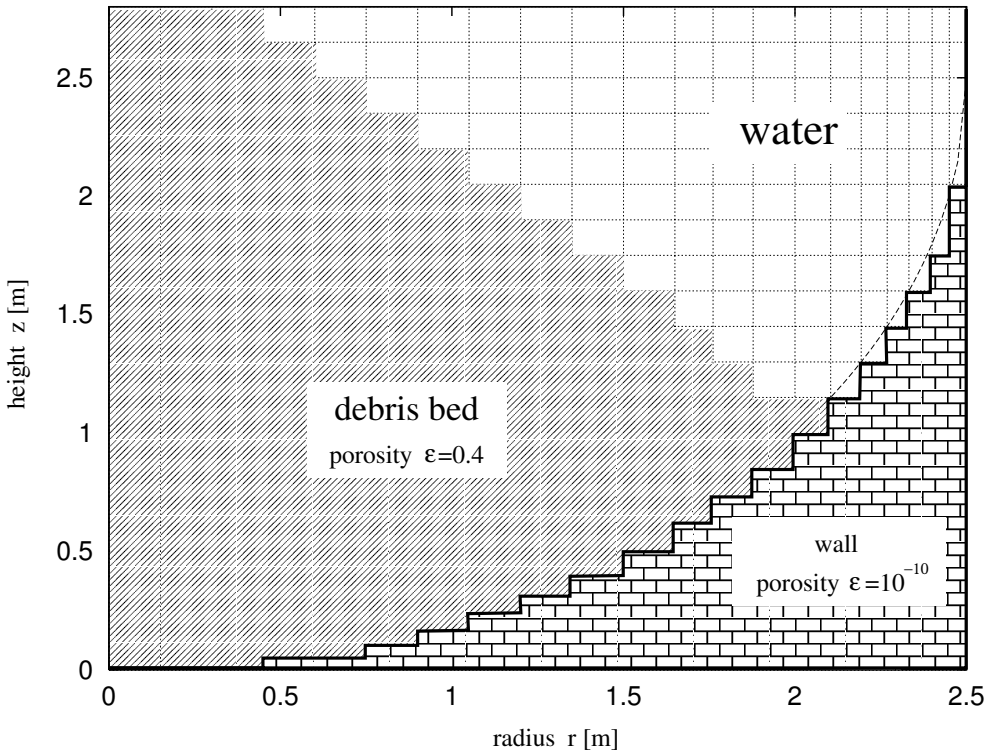

Figure 7.14: Configuration of the particulate debris in the lower head (case2)

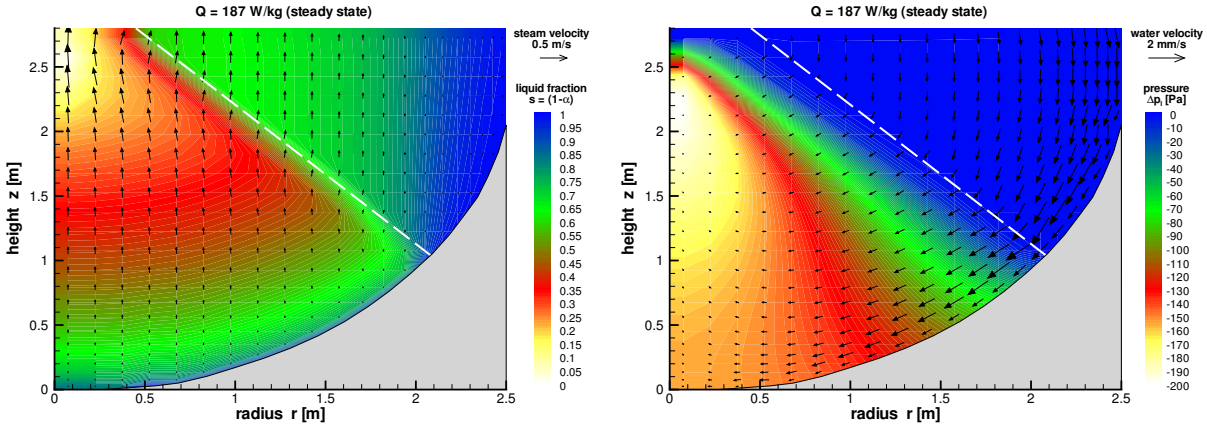

(a) Reed

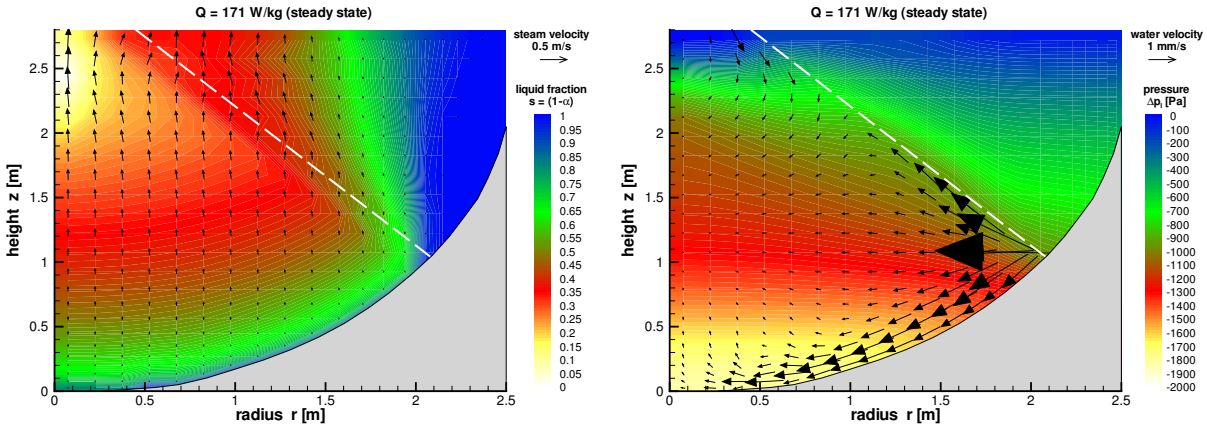

(b) Schulenberg

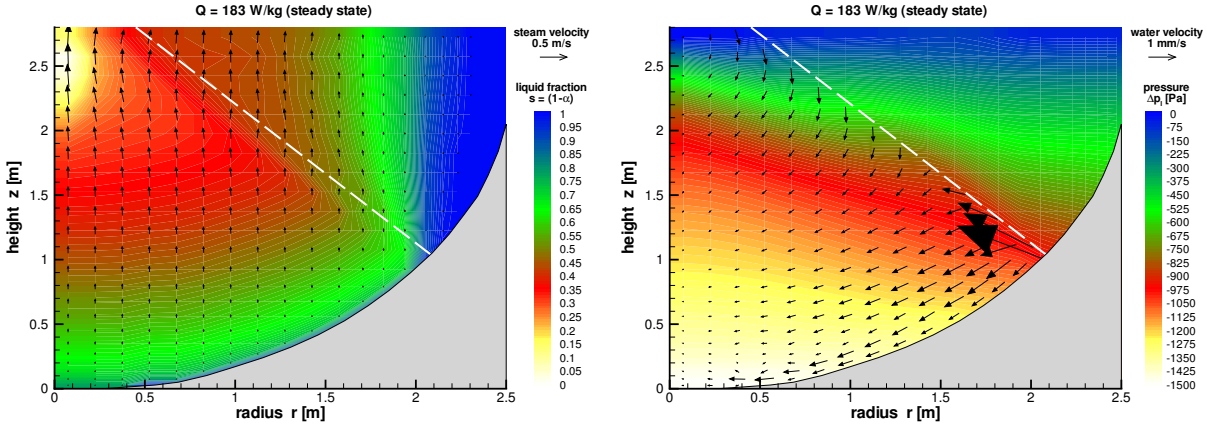

(c) modified Tung/Dhir

Figure 7.15: Distribution of liquid fraction and steam velocity (left) as well as local pressure, reduced by the hydrostatic head, and liquid velocity (right) for the different models for the configuration of case 2

		Case 1			Case 2		
		R	S	mTD	R	S	mTD
DHF [MW/m^2]	1D	1.74	1.56	1.97	1.74	1.56	1.97
	WABE-2D	2.20	2.15	2.48	2.50	2.29	2.45
max. spec. power [W/kg]	1D	228	204	257	132	119	147
	WABE-2D	301	281	324	187	171	183
total power [MW]	1D	18.34	16.41	20.60	11.37	10.25	12.64
	WABE-2D	24.21	22.60	26.06	16.10	14.72	15.76
gain		32%	38%	26%	42%	44%	25%

Table 7.1: Results for in-vessel calculations for different models (R: Reed, S: Schulenberg, mTD: modified Tung/Dhir)

7.3 Ex-Vessel particulate debris

If the corium can not be cooled inside the vessel, e.g. due to the non availability of cooling water, a melt pool will develop in the lower plenum and attack the reactor pressure vessel. After vessel failure the melt will flow out of the vessel into the reactor pit, as described in chapter 2. If the cavity is filled with water, either automatically, or due to accident management measures, the melt jet will pour into water. Especially for Boiling Water Reactors (BWR) with the great depth of the cavity a good fragmentation of the melt jet may be expected under such conditions. These fragments again settle as a particulate debris. To avoid further destruction and radioactive contamination of the environment, coolability should be reached at least at this stage, before losing the containment integrity as the last safety barrier. Configurations with fragmented corium in a water pool, as described above, have a high potential of coolability, especially when water access from below is possible, as will be shown in the next calculations.

In the following scenario a large Boiling Water Reactor is assumed, where the total core and major parts of core components have been destroyed. The fragmented corium has settled as particulate debris in the reactor pit. The chosen corium consists of about 150 t UO_2, 80 t Zircalloy and 210 t structure material yielding a total corium mass of $M = 440$ t. These values are typical for reactors of about 4000 MW thermal power. As the decay heat after one hour is about 1 % of this value, about 40 MW have to be discharged from the particles in the reactor pit. This corresponds to a specific power of $Q \approx 90$ W/kg.

In the calculations a radius of 4.4 m, typical for such reactors, is chosen for the reactor pit. The geometry is shown in figure 7.16 (a). At the outer boundary a supporting base of the mounting devices is considered as wall area. As to be expected in reality, the particulate debris is chosen to have a mound shape with a slope angle of 33.7°. For a porosity of $\varepsilon = 0.4$ a bed height of $H_{max} = 2.8$ m is obtained. As for the in-vessel calculations a particle diameter of $d_p = 3$ mm is chosen, but now at a smaller system pressure of only $p = 3.15$ bar, because in general the pressure will be less in the containment. As mentioned in subchapter 3.5 this lower pressure yields less coolability due to the reduced steam density.

In addition to this base configuration, two modifications shall be considered in the calculations to investigate some supporting features that may be considered in reality. Objective of the first modification is to take advantage of enhanced coolability if water inflow from below can be installed. In a reactor this may be achieved via the sump below the reactor pit. If there is a connection from the water filled containment to the

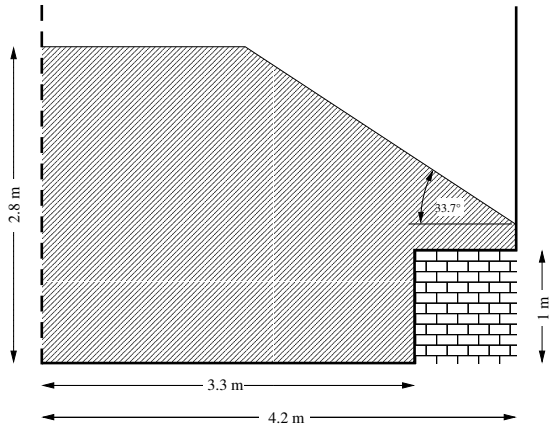

(a) Base configuration

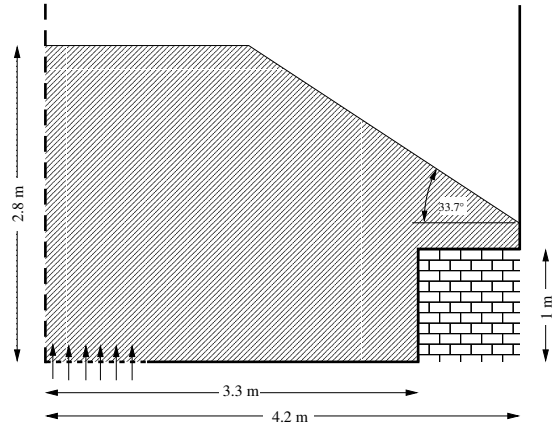

(b) Including water loop over sump

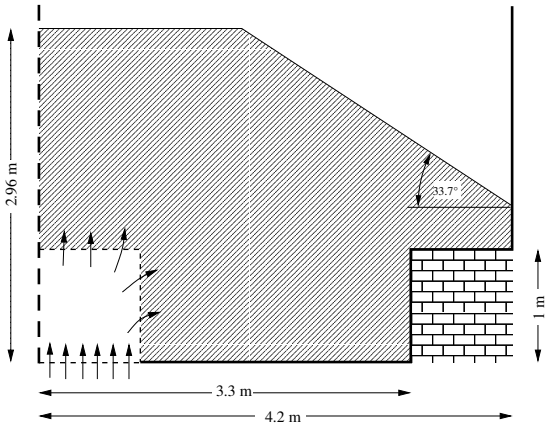

(c) Additionally cage over the sump

Figure 7.16: Configuration of the particulate debris in the reactor pit

grid covered sump, water at hydrostatic pressure is connected to the bottom of the particle bed. As the pressure inside the bed is less than hydrostatic, a water influx will establish and support the overall coolability. Even better, if the sump is connected to a water reservoir at higher level, this pressure difference, and thus the water inflow, will be further enhanced. In the calculations this is considered by defining the hydrostatic pressure as boundary condition at the bottom. As can be seen in the sketch in figure 7.16 (b) here a radius for the inflow region of $r = 0.6\,\mathrm{m}$ is chosen. Thus, inflow is only possible via a minor part of the lower bound.

A further enhanced configuration is proposed in figure 7.16 (c). Now a cage with a height of 1 m is assumed above the sump. By this, the total inflow area is increased,

and it can be expected, that more water can flow into the particle bed. On the other hand, keeping the total mass constant, this measure rises the bed height by 16 cm to $H_{max} = 2.96$ m in the centre. In general this yields a counter effect that will complicate the coolability of the whole configuration.

Calculations using the Reed model as well as the enhanced models of Schulenberg and Tung/Dhir, including the modifications proposed in subchapter 5.3.1, were carried out for the three configurations. The resulting steady state distributions of the liquid fraction ($s = 1 - \alpha$), pressure (reduced by the hydrostatic part) and velocities for a power just below the overturn are given in the next figures. First of all, figure 7.17 shows the results for the Reed friction model. As can be seen in subfigure (a), steady states can be reached up to a specific power of $Q_{max} = 146$ W/kg in the base configuration. Due to the multidimensional effects of the mound shape, this value again is noticeably higher than for a pure 1D configuration with the same height of $Q^{1D}_{max} = 112$ W/kg. This again yields a gain of 30 % in the overall coolability. The reason for this gain can be seen in the water velocities shown in figure 7.17(a). Central regions, where the bed is highest, are supported by a lateral water inflow from the lower outer parts of the bed. This is even enhanced by the base with the very shallow bed part above. An almost dry spot can be seen near the top of the bed, but this spot is laterally shifted from the centre. Here the water infiltration from the top is hindered by the huge steam flux from below. On the other hand, the lateral water flow mainly supplies central regions.

Opening the water loop over the reactor sump, as described before, an enhanced coolability is expected. The calculation result for the Reed model yielding a maximum specific power of $Q_{max} = 152$ W/kg is given in figure 7.17 (b). To resolve the velocity field in the debris part the vectors of the water velocities in the first axial calculation cell over the bottom inlet are ignored in the figure. A strong water influx from below can be observed. But, comparing the maximum power to the one without bottom inflow, only a slightly higher value can be reached. The bottom inflow yields no significant enlargement in the overall coolability. Integrating the liquid volume flux over the boundaries yields a water volume flux of 6.51 l/s from below, while the main fraction of 26.33 l/s still flows via the top surface into the particle bed. Thus, only about 20 % of the water is coming from below. The given boundary pressure at the inlet also affects the pressure field in the whole bed. As the pressure field shown in the figures is the local pressure reduced by the hydrostatic one of a water column, a value almost to zero establishes above the inlet. The pressure gradient here corresponds to the pressure loss of the inflowing water. As a consequence, the pressure rises everywhere in the particle bed, leading to smaller pressure gradients. Thus the driving force for the coolant flow is reduced in the bed, yielding only a minor gain in coolability.

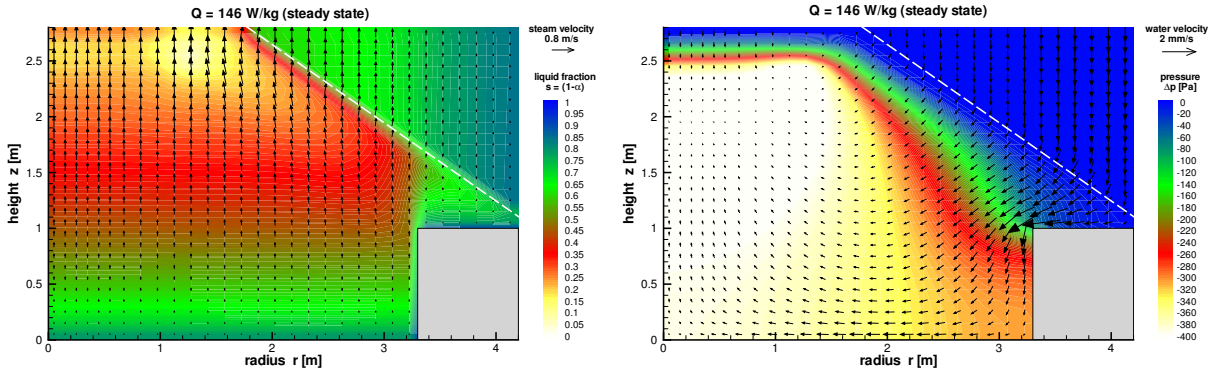

(a) case 1; maximum possible specific power 146 W/kg

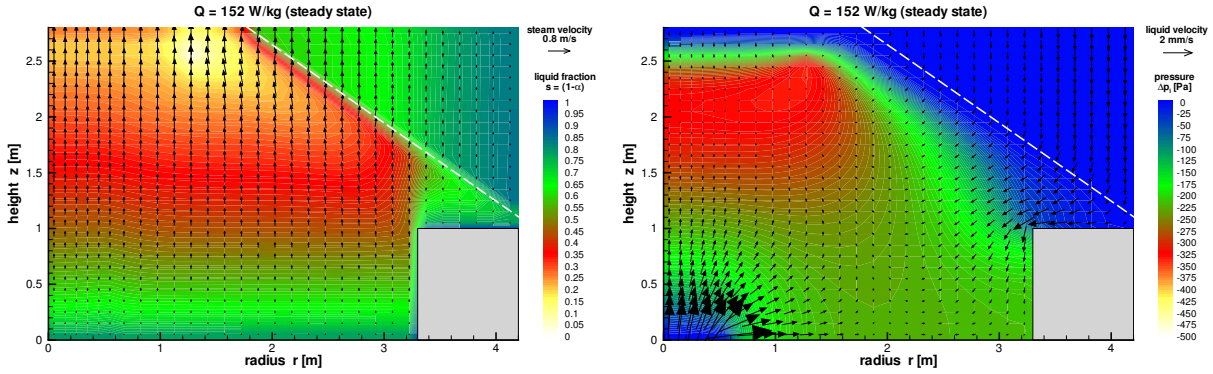

(b) case 2; maximum possible specific power 152 W/kg

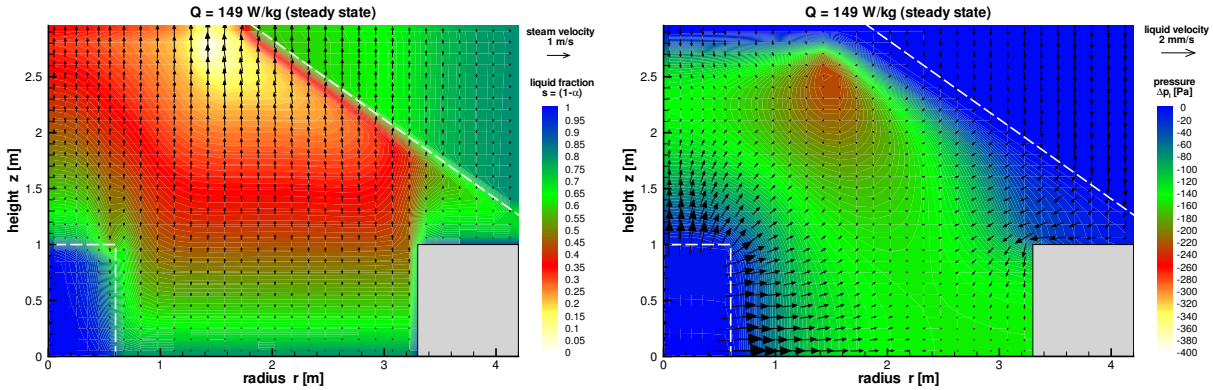

(c) case 3; maximum possible specific power 149 W/kg

Figure 7.17: Distribution of liquid fraction and steam velocity (left) as well as local pressure reduced, by the hydrostatic head, and liquid velocity (right) for ex-vessel particulate debris according figure 7.16 (Reed model)

A further enhancement of the overall coolability is expected for the configuration of figure 7.16 (c) with a cage over the inlet region. Surprisingly, for the Reed friction model with Q_{max}=149 W/kg the global coolability is less than without the cage. This is due to the counter effect of the enlarged bed height. As can be seen in figure 7.17 (c), again a significant water inflow over the sump can be observed. But, this can not compensate the counter effect. Looking at the integrated water fluxes now an inflow rate of 10.89 l/s, corresponding to 31 % from below is calculated. So, although the area connected directly to the water path is increased by a factor of 4.3 the overall influx is only raised by slightly. Thus, based on this classical model without the interfacial drag term, the increase of influx is only moderate. In this calculation the counter effect of the increased bed height dominates. As before, the smaller pressure gradient leading to less water movement in the debris, can be seen in the plot. Correspondingly, the inflow from above is reduced.

The interfacial drag, hindering the water inflow from the top, should support the overall coolability, if the coolant is supplied from below. Results of the calculations for the different configurations are given in figure 7.18 for the Schulenberg and in figure 7.19 for the modified Tung/Dhir model. In the base configurations of subfigures (a) the effect of the geometry alone can be observed. First of all, again an increased coolability compared to 1D considerations can be seen. This is due to the geometrical shape. The maximum specific power values are summarised in table 7.2. A gain of 20 % for the Schulenberg model and of only 9 % for the modified Tung/Dhir model was calculated compared to the 1D results. Again the small gain for the Tung/Dhir model is partly due to the high value for the 1D configuration. As in the in-vessel cases, the drag of the upflowing steam hinders the water inflow over the shell of the mound. A kind of water loop establishes in the water area. By this flow, some water is drawn out of the "gusset" above the outer support base. But this effect has only minor influence on the overall coolability. Besides this, as for the in-vessel cases, the main difference to the Reed result can be seen in the pressure distribution. Again the enhanced models yield a significant increased pressure gradient with the lowest pressure value at the bottom of the particle configuration.

Enabling the water inflow possibility from below over the reactor sump, this smaller pressure is connected to the outer hydrostatic one. Thus coolant is pressed into the debris until the pressure loss due to the inflow compensates the pressure gradient, leading to steady inflow conditions. The enlarged water inflow for the enhanced models compared to the Reed results can clearly be seen in the figures. Even better this enlarged inflow is shown by the integrated coolant influxes. While in the Reed model only 20 % of the total coolant flows via the bottom, here 80 % for the Schulenberg

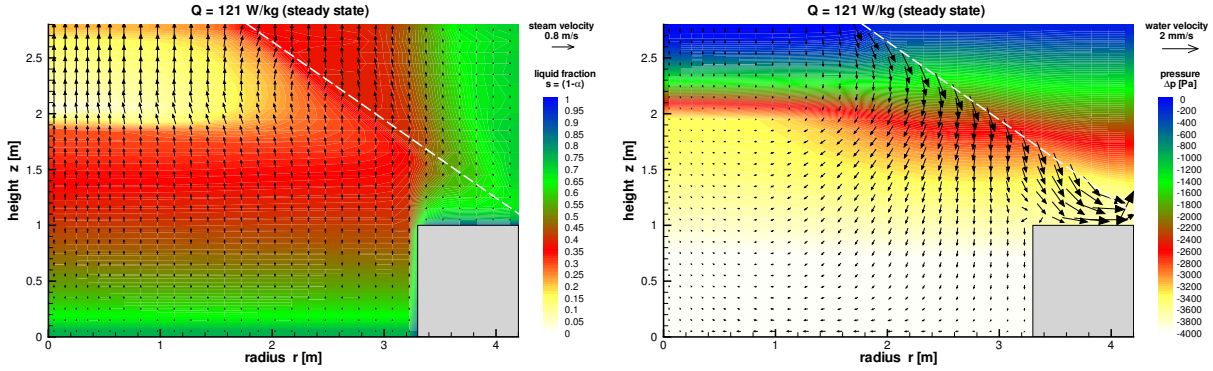

(a) case 1; maximum possible specific power 121 W/kg

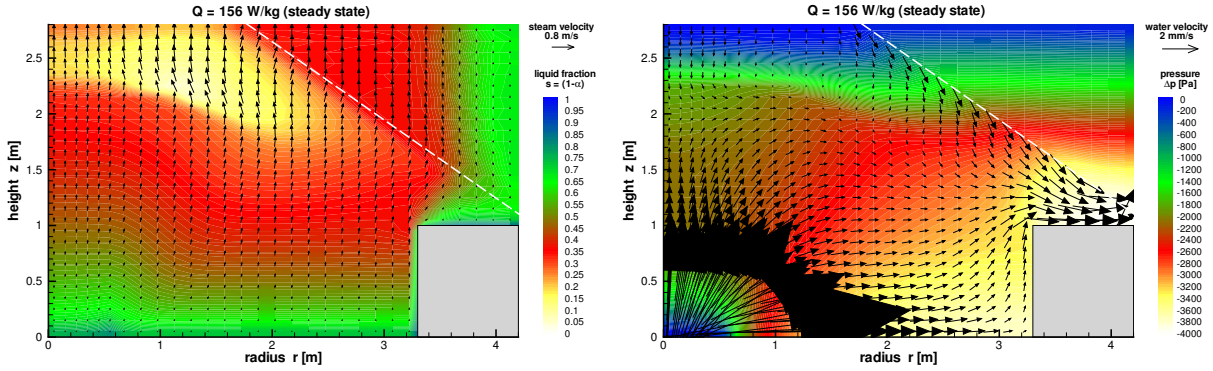

(b) case 2; maximum possible specific power 156 W/kg

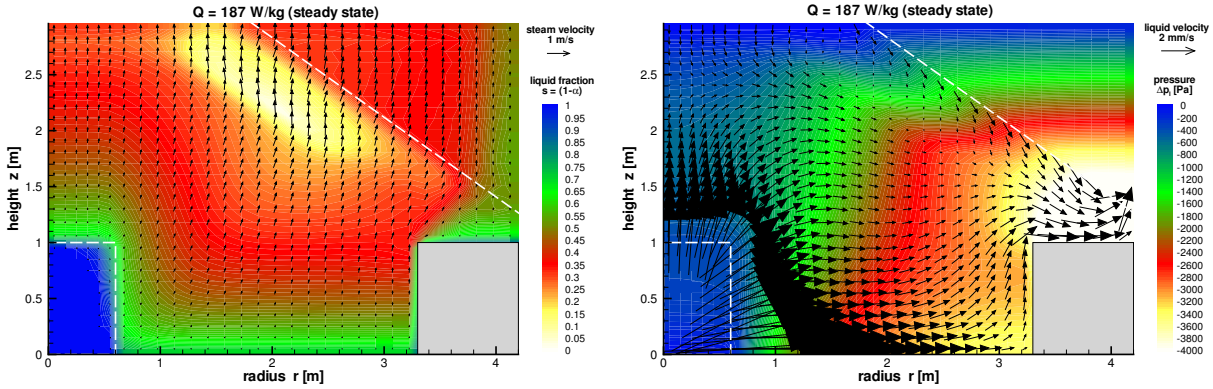

(c) case 3; maximum possible specific power 187 W/kg

Figure 7.18: Distribution of liquid fraction and steam velocity (left) as well as local pressure, reduced by the hydrostatic head, and liquid velocity (right) for ex-vessel particulate debris according figure 7.16 (Schulenberg model)

model and 72 % for the modified Tung/Dhir formulation comes from below. These fractions are even increased by increasing the inflow area by the cage over the sump in the configuration of figure 7.16 (c). Now a coolant fraction of 95 % for the Schulenberg and 94 % for the modified Tung/Dhir model are supplied through the lower bound. This further enhanced influx from below yields an increased overall coolability, even for the higher bed in the configuration with the cage. Compared to the case (a) without bottom influx an increase of 20 % for the modified Tung/Dhir formulation and of 55 % for the Schulenberg model is calculated.

Comparing the calculated power limits of table 7.2 with the expected decay heat of about $Q_{reactor} \approx 90\,\mathrm{W/kg}$ shows the high chances for overall coolability in the containment, even for the simpler Reed model. But, in the calculations presented here, only a homogeneous configuration with a large amount of structure material was assumed. Besides the precondition of the possible fragmentation and quenching of the hot particles, setups including hindering effects have not been observed here. Coolability has to be reached even for configurations with complicating conditions. In general, the emphasised lateral water flow and the interfacial drag will additionally support the coolability in such hindered cases. A detailed analysis is necessary to investigate the safety margins. But, these margins are remarkable higher for the enhanced models.

Based on these calculations it can be concluded, that the interfacial friction has a significant influence on the overall coolability if water access from below is enabled. Although only a minor fraction of 2 % of the lower bound is directly connected to the coolant pool, a remarkable increase in the maximum coolable bed power is calculated. This shows the importance to include the interfacial drag in the momentum equations, as done by Schulenberg and Müller or Tung and Dhir.

	R		S		mTD	
	Q_{max}	f	Q_{max}	f	Q_{max}	f
1D	112	-	101	-	124	-
base configuration	146	-	121	-	135	-
including inflow via sump	152	20 %	156	80 %	152	72 %
including cage over the sump	149	31 %	187	95 %	161	94 %

Table 7.2: Maximum specific powers Q_{max} (in [W/kg]) and the fraction f of water inflow from below in the ex-vessel calculations for the different models (R: Reed, S: Schulenberg, mTD: modified Tung/Dhir)

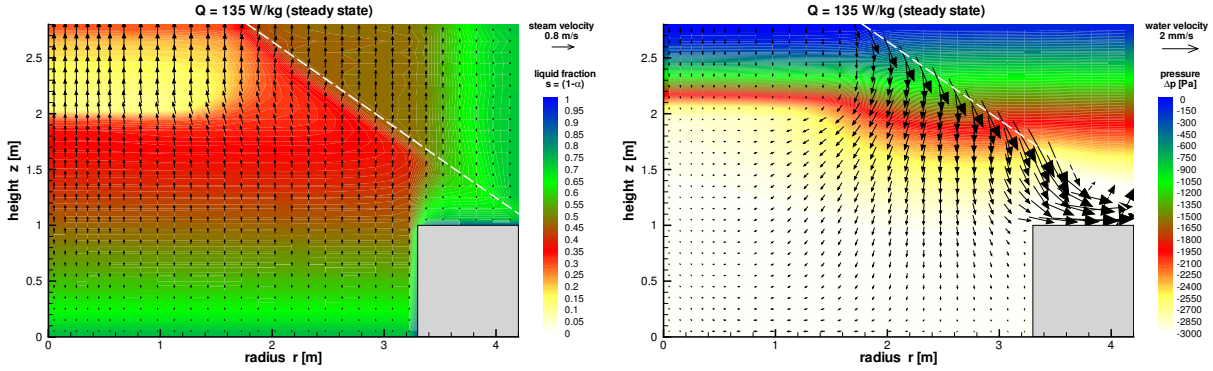

(a) case 1; maximum possible specific power 135 W/kg

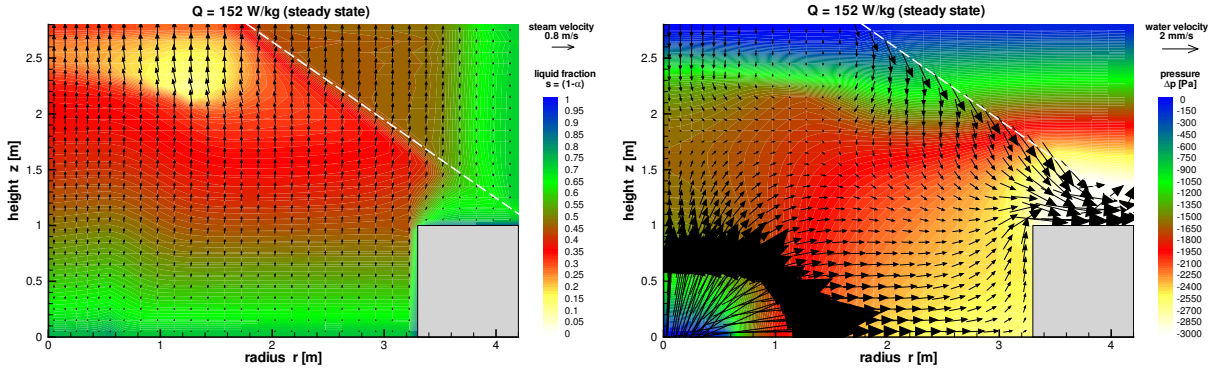

(b) case 2; maximum possible specific power 152 W/kg

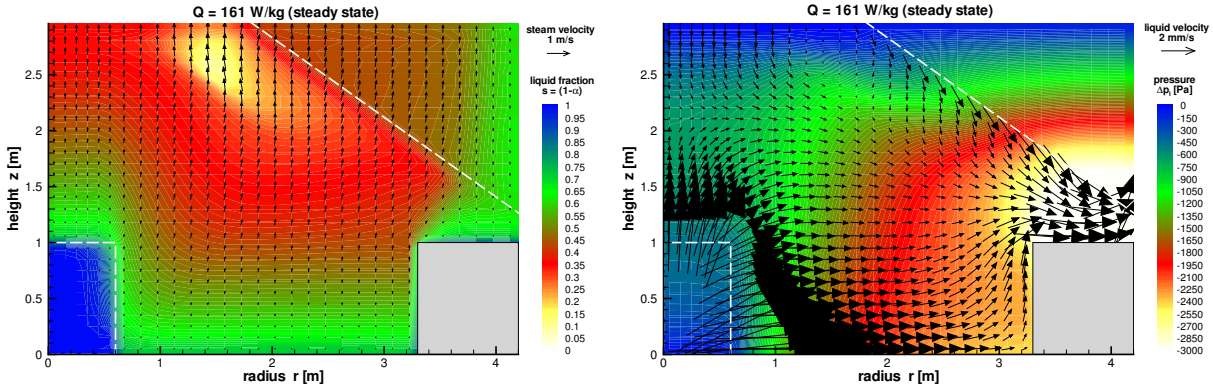

(c) case 3; maximum possible specific power 161 W/kg

Figure 7.19: Distribution of liquid fraction and steam velocity (left) as well as local pressure, reduced by the hydrostatic head, and liquid velocity (right) for ex-vessel particulate debris according figure 7.16 (modified Tung/Dhir model)

8 Summary and conclusion

The central aim of this thesis has been to work out the cooling potential of fragmented corium, which has to be expected during a very unlikely severe accident in a Light Water Reactor. Due do the high decay heat, coolability can only be achieved by evaporation of water. So the coolability is determined by the two phase flow of water and steam in the porous configuration of the corium. Classical considerations are based on one dimensional configurations with a coolant pool over the heated particle bed. By increasing the bed power, a limiting heat flux before reaching a local dryout was determined. Correspondingly, models have been developed to calculate this dryout heat flux for different conditions. These models are based on the pressure loss of flows through porous media according to Ergun, extended by relative permeabilities and passabilities, to encounter the influence of the second fluid phase. Various authors published formulations describing the dependence of these relative coefficients on the volume fractions. But, the development of these models is just by an adaptation of the particle-fluid friction in that way, to reproduce the experimentally determined dryout heat flux of a 1D top fed configuration. Based on his experiments Reed proposed such a formulation, which is now used by many researchers.

While this adaptation of the relative permeability and passability was very successful for the experimentally observed 1D top fed configurations, it is not applicable to situations with a pressure driven coolant inflow from below. Likewise is the situation for multidimensional configurations, which are to be expected in reactor applications. Lower parts of the bed may be supplied by a water inflow via preferred flow paths, enhancing the overall coolability. The steam and the water flow are now no more in a counter-current mode as before, but flow co-currently, at least in some regions of the bed. The interfacial friction, which is included in the classical models only in a global manner, supports the coolant inflow from below. So, some authors additionally included an explicit formulation of the interfacial friction in their models. But, it is still difficult to split the contributions of the different drag parts to the measured overall pressure loss.

To investigate the coolability in typical reactor configurations, verified computer codes based on verified friction laws have to be used. In chapter 6 comparisons of the models with single effect experiments, for isothermal as well as for boiling beds, have been

presented. The necessity of the explicit consideration of the interfacial drag was directly shown by the pressure loss in the isothermal experiments with no net liquid flow. Two models including this friction have been regarded in this thesis. The first one of Schulenberg and Müller is based on isothermal air-water experiments with a realistic particle diameter of $d_p = 3\,\mathrm{mm}$. Based on more theoretical considerations, including also different flow patterns, Tung and Dhir proposed another enhanced model. They also verified their model by comparison with experimental results of the pressure loss in isothermal air-water experiments, but with larger particles. In chapter 5 some modifications for this model have been proposed, in order to extend it to smaller diameters. Additionally, the interfacial friction in the annular flow regime was modified to reach a plausible limit for high voids.

Based on the different models, calculations on reactor relevant configurations have been presented in chapter 7. The results of the in-vessel calculations show an enhanced coolability in two dimensional geometries of about 30-40 %, compared to a 1D configuration. For a bed power slightly higher than the critical one a first dry spot establishes in the highest bed regions, in contradiction to the 1D case, where, after a transient, a dry zone develops near the bottom. Only a minor additional benefit was observed for the enhanced models, which include the interfacial drag. As in the classical models, here the commonly used one according Reed was applied, all water inflow is form the pool above. The direct water inflow from this pool is hindered by the interfacial drag in the models with interfacial drag. But, stronger pressure gradients are observed, that compensate the increased friction, and thus support the coolability.

Non coolable in-vessel configurations would yield a melt pool in the lower head of the reactor pressure vessel, that would attack the vessel walls. Assuming a flooded cavity of sufficient water height, melt fragmentation and settlement of particulate debris in the reactor pit may be assumed again after failure of the vessel. Due to the larger base area, the bed height for the ex-vessel particulate debris would be reduced. However, larger total corium masses have to be assumed here. In subchapter 7.3 a typical ex-vessel configuration for a large boiling water reactor with some variants was studied. As in the in-vessel cases again a gain in the coolability, compared to 1D, was calculated just due to the geometrical configuration of the debris mound. A strong enhancement of the overall coolability was expected for an assumed water inflow from below. In a typical reactor, this may be established via the reactor sump, covered by a grid, that may be connected to the water filled cavity or, even better, to a high-placed coolant reservoir. Although the cross section of the sump affects only a very small fraction of 2 % of the cavity, a better overall coolability was shown in the calculations, especially for the enhanced models, while the classical Reed model yields only a minor influence. The

interfacial drag and the stronger pressure gradient in the debris region yield a higher water inflow from below. Additionally, in the lower bed regions the void fraction is small leading to reduced particle-liquid friction.

As an additional constructive measure, the placing of a cage over the sump to increase the inflow area was proposed in subchapter 7.3. But, based on the calculations, for the Reed model the coolability was reduced due to the slightly increased bed height. In contrast to this model, the enhanced one of Schulenberg and the modified Tung/Dhir model yield a further increase in the overall coolability. The water inflow from below is significantly enlarged by the cage construction. Almost all water inflow is via the bottom, increasing the overall cooling potential. These calculations show the importance of the interfacial drag on the coolability of configurations with water inflow from below. Thus, this drag has to be included in investigations of the overall coolability.

By the calculations good chances to reach coolability, either in- or ex-vessel, have been shown. Comparing the maximum specific power reached in the calculations with the expected decay heat, almost all configurations may be regarded as coolable. Only the in-vessel configuration of case 2, with the great bed height, may be critical, depending on the corium composition, and thus the specific power. However, in all calculations homogeneous conditions, although for small particles, have been assumed. Supporting effects, as well as hindering effects, may occur in non homogeneous configurations. Flow paths with higher porosity lead to enhanced coolability, while for well mixed multigrain configurations, or due to badly fragmented cakes, locally lower porosities and thus less coolability may be obtained. The same holds for local power concentrations due to inhomogeneities in the corium composition. A special effect that may also be expected in reality due to the settlement of the fragments is the layering of the fragments, with smaller particles covering larger ones. This layer of smaller particles acts like a sponge holding the water. In 1D top fed configurations this yields a dramatic reduction of coolability (see [23]). In realistic configurations, multidimensional effects have to be considered. First of all, a really sharp transition between the layers over the whole cross section, as set in the experiments, is very unlikely. Secondly, in multidimensional configurations water may easier find a preferred flow path to lower bed regions. This is even enhanced if there is an unhindered flow path to the bottom. Results of various calculations, also including hindering effects, as described above, can be found in [11, 13].

In this thesis coolability is defined by steady states, where no dry spot occurs inside the particle configurations. The evaporated water can be replaced by inflow at each location. The definition of the overall coolability may be extended even for configura-

tions with a local dryout. Such a dry spot may be cooled by heat transfer to the steam flux through it. This requires first of all a steady steam flux from below, and thus a lateral water supply to these regions. Secondly, the extension of the dry spot may only be very small. Exemplary calculations can be found in [11, 13]. As also discussed in the same reports, the cooling criterion may even be carried up to local remelting, where a small melt pool establishes on a crust, cooled from below by water. In this sense the potential of overall coolability is further enhanced.

In general it can be concluded, that multidimensional treatment is required to investigate the potential of coolability for realistic debris configurations. The models have to be based on verified friction laws in the range of relevant parameters. These may be taken from single effect experiments, as described in chapter 6. In general, it is not easy and clear in every case, how to distribute the friction to the different drag terms. Thus, further experimental investigations are necessary, especially for smaller particle diameters in the range of 1–6 mm. The ongoing DEBRIS experiments at IKE are designed for such studies in boiling beds. Unfortunately, the SILFIDE experimental program at EdF had been stopped before real 2D test were performed. Based on such experiments general code validations would have been possible.

References

[1] K. Hu and T.G. Theofanous. On the measurement and mechanism of dryout in volumetrically heated coarse particle beds. *Int.J. Multiphase Flow*, Vol.17(No.4), 1991.

[2] G. Hofmann. On the location and mechanisms of dryout in top-fed and bottom-fed particulate beds. *Nuclear Technology*, Vol. 65, April 1984.

[3] A.W. Reed, K.R. Boldt, E.D. Gorham-Bergeron, R.J. Lipinski, and T.R. Schmidt. DCC-1 / DCC-2 Degrated Core Coolability Analysis. Technical Report NUREG/CR-4390, SAND85-1967, Sandia National Laboratory, Oct. 1985.

[4] R.J. Lipinski. A one dimensional particle bed dryout model. *ANS Transactions*, Vol.38:386–387, June 1981.

[5] W. Chu, V.K. Dhir, and J. Marshall. Study of pressure drop, void fraction and relative permeabilities of two phase flow through porous media. In *Heat transfer-Seattle*, volume Vol.79 of *AIChE Symposium series*, pages 224–235, 1983.

[6] N.K. Tutu, T. Ginsberg, and J.C. Chen. Interfacial drag for two-phase flow through high permeability porous beds. *Journal of Heat Transfer*, Vol.106:pp. 865–870, Nov. 1984.

[7] D. Magallon, I. Huhtiniemi, and H. Hohmann. Lessons Learnt from FARO/THERMOS Corium Melt Quenching Experiments. In *Proceedings of the OECD/CSNI Specialists Meeting on Fuel Coolant Interactions, May 1997*. JAERI, 1998.

[8] H. Hohmann, D. Magallon, I. Huhtiniemi, A. Annunziato, and A. Yerkess. Advance in the FARO/KROTOS melt quenching test series. In *22nd Water Reactor Safety Information Meeting*, Bethesda, Maryland, USA, Oct. 23-26 1994.

[9] É. Décossin. Experimental investigations on particulate debris bed coolability in a multi-dimensional configuration. In *OCDE/CSNI-Workshop on EX-VESSEL DEBRIS COOLABILITY*, 16.-18. Nov. 1999.

[10] P. Schäfer and D. Steiner. Untersuchungen zum Dryout und Druckabfall in einer 6 mm Kugelschüttung. Technical report, IKE, Universität Stuttgart, Mai 2002. IKE 5-TB-1718-02.

[11] M. Bürger, W. Schmidt, G. Pohlner, and W. Widmann. Stand der Arbeiten zum Schüttungsmodell WABE und Mischungsmodel IKEMIX. Technical report, IKE, Universität Stuttgart, Dez. 1999. IKE 2-143.

[12] M. Buck. *Modelling of the Late Phase of Core Degradation in Light Water Reactors*. Doktorarbeit, IKE, Universität Stuttgart, (in Vorbereitung) 2003.

[13] M. Bürger, M. Buck, W. Schmidt, G. Pohlner, and W. Widmann. Ausbau und Verifikation der Spätphasenmodelle und des Gesamtmodels zum Kernschmelzen in KESS und ATHLET-CD. Technical report, IKE, Universität Stuttgart, Mai 2001. IKE 2-145.

[14] W. Widmann. *Theoretical Modelling of Ex-Vessel Core Melt Coolabiltiy by Injection of Water from the Bottom*. Doktorarbeit, IKE, Universität Stuttgart, (in Vorbereitung) 2003.

[15] H. Alsmeyer and W. Tromm. Concept of a core cooling system and experiments performed. *Nuclear Engineering and Design*, vol. 154:pp. 69–72, 1995.

[16] H. Brauer. *Grundlagen der Einphasen- und Mehrphasenströmung*. Verlag Sauerländer, Aarau und Frankfurt, 1971.

[17] L.Barleon and H.Werle. Dependence of dryout heat flux on particle diameter for volume- and bottom-heated debris beds. Technical Report KfK 3138, Kernforschungszentrum Karlsruhe, 1981.

[18] R. Trenberth and G. F. Stevens. An experimental study of boiling heat transfer and dryout in heated particulated beds. Technical report, UKAEA Winfrith (UK), 1980.

[19] D. Squarer, A. T. Pieczynski, and L. E. Hochreiter. Effect of debris bed pressure, particle size and distribution on degraded nuclear reactor core coolant. In *Nuclear Sience and Engenering*, volume 80, pages 2–13. 1982.

[20] I. Catton, V.K. Dhir, and C.W. Somerton. An experimental study of debris-bed coolability under pool boiling conditions. Technical report, University of California at Los Angeles, 1983.

[21] J. D. Gabor et al. Status report on limiting heat fluxes in debris beds. Technical Report ANL/RAS 80–21, Aronne National Laboratory, 1980.

[22] J.S. Marshall and V.K. Dhir. Effect of overlying liquid layer on dryout heat flux measurements. *Nuclear Science and Engineering*, Vol.91:pp.109–113, 1985.

[23] G. Hofmann and L. Barleon. Reduced coolability of particle beds as a result of capillary effects at horizontal phase boundaries. In *ANS/ENS Topical Meeting on Thermal Reactor Safety, San Diego, Cal.*, Feb. 1986.

[24] M.C. Leverett. Capillary behavior in porous solids. In *Transactions of the American Institute of Mining and Metallurgical Engineers*, volume Vol.142, 1941.

[25] B.D. Turland and J. Morgan. Compendium of post accident heat removal models for liquid metal cooled fast breeder reactors. In *European Application Research Report*, volume EUR 10250 EN, 1985.

[26] S. V. Patankar. *Numerical Heat Transfer and Fluid Flow.* Hemisphere Publishing Corporation, 1980.

[27] H. Darcy. *Les Fontaines Publiques de la Ville de Dijon.* Dalamont, Paris, 1856.

[28] S. Ergun. Fluid flow through packed columns. *Chemical Engineering Progress*, Vol. 48(No.2):pp. 89–94, Feb. 1952.

[29] P. Mayr. *Analytische Untersuchung zur Kühlbarkeit schwer zerstörter Kernbereiche in Leichtwasser-Reaktoren.* Doktorarbeit, IKE, Universität Stuttgart, September 1995. IKE 2-104.

[30] R.H. Brooks and A.T. Corey. Hydraulic properties of porous media. Hydrology Papers, Colorado State University, March 1964. No. 3.

[31] A.W. Reed. *The effect of channeling on the dryout of heated particulate beds immersed in a liquid pool.* PhD thesis, Massachusetts Institute of Technology, Cambridge, Feb. 1982.

[32] R.J. Lipinski. A coolability model for postaccident nuclear reactor debris. *Nulcear Technology*, Vol.65:pp. 53–66, April 1984.

[33] T. Schulenberg and U. Müller. A refined model for the coolability of core debris with flow entry from the bottom. In *Proceedings of the Sixth Information Excange Meeting on Debris Coolability*, number EPRI NP-4455. University of California, Los Angeles, March 1986.

[34] V.X.Tung and V.K.Dhir. A hydrodynamic model for two-phase flow through porous media. *International Journal of Multiphase Flow*, Vol. 14(No. 1):pp. 47–65, 1988.

[35] D. Haga and Y. Niibori nad T. Chida. Tracer responses in gas-liquid two-phase flow through porous media. In *Procieedings World Geothermal Congress*, Kyushu - Tohoku, Japan, 2000.

[36] G.F. Stevens and R. Trenberth. Experimental studies of boiling heat transfer and dryout in heat generating particulate beds in water at 1 bar. In *Proceedings of the Fifth Post Accident Heat Removal Information Exchange Meeting*, pages 108–113. Nuclear Research Center Karlsruhe, 1982.

Institut für Kernenergetik und Energiesysteme

Universität Stuttgart

Pfaffenwaldring 31

D-70550 Stuttgart